

MITIGATION OF ELECTRIC VEHICLE CHARGING EFFECTS ON DISTRIBUTION GRIDS THROUGH SMART-CHARGING AND ON-BOARD SOLAR CHARGING

Muhammad Hosnee Mobarak

McMaster University, mobarm2@mcmaster.ca

**MITIGATION OF ELECTRIC VEHICLE CHARGING
EFFECTS ON DISTRIBUTION GRIDS**

**MITIGATION OF ELECTRIC VEHICLE CHARGING
EFFECTS ON DISTRIBUTION GRIDS THROUGH SMART-
CHARGING AND ON-BOARD SOLAR CHARGING**

By

MUHAMMAD HOSNEE MOBARAK, M.Sc. (TUM)

A Thesis

Submitted to the School of Graduate Studies
in Partial Fulfilment of the Requirements
for the Degree of Doctor of Philosophy
in Electrical and Computer Engineering

McMaster University

© Copyright Muhammad Hosnee Mobarak, August 2021. All rights reserved.

Doctor of Philosophy (2021)

McMaster University

(Electrical and Computer Engineering)

Hamilton, Ontario

TITLE: Mitigation of Electric Vehicle Charging Effects on Distribution Grids
Through Smart-Charging and On-board Solar Charging

AUTHOR: Muhammad Hosnee Mobarak, M.Sc. (TUM)

SUPERVISOR: Dr. Jennifer Bauman

NUMBER OF PAGES: xiv, 202

Lay Abstract

Overheating, accelerated aging, and eventual early failure of the distribution transformers caused by EV charging stress is a pressing concern that needs to be addressed. This thesis proposes two new vehicle-directed smart charging strategies and a concept of solar-charged electric vehicle (SEV) to help reduce the accelerated aging of distribution transformers. System level analysis of the mitigation of transformer aging using these two approaches with added driver and environmental benefits warrants the manufacturing and design challenges of the SEVs. Thus, this thesis proposes a fast and novel global maximum power point tracking algorithm well suited to fast moving vehicles for maximum solar power extraction at all times, especially during partial shading conditions, and an optimization process of the on-board PV cell dimension and number of such cells in series and parallel in the array based on power electronic converter for higher efficiency, lower cost, and lower mass.

Abstract

Electric vehicles (EV) have become very popular in recent years because they are a more sustainable, efficient, and environmentally friendly transportation option than traditional fossil-fuel vehicles. Increased EV charging can cause overheating, accelerated aging, and eventual early failure of the distribution transformers, as the distribution networks have not been established foreseeing a large number of EVs as loads. This thesis makes contributions in two main areas to help reduce the accelerated aging of distribution transformers as the number of EVs on the road continues to rise.

Firstly, vehicle smart charging is investigated to spread out the EV charging loads and hence decrease transformer heating and aging. Most EV smart charging algorithms require the use of extensive and costly infrastructure, including sensors, communication networks, controllable chargers, and central smart agents. This thesis proposes a new vehicle-directed smart charging strategy, called Random-In-Window (RIW) which allows individual vehicles to spread out their charging without any costly additional infrastructure. Detailed simulation results prove the advantages of this proposed algorithm.

Secondly, to further reduce EV charging loads on the grid, a large-scale solar-charged electric vehicle (SEV) is proposed. While RIW smart charging has only grid benefits, SEVs can contribute to grid benefit, driver benefit, and environmental benefit, as shown through detailed simulation results, making it a

viable solution to transformer aging mitigation. To turn the SEV concept into reality, this research also proposes a fast maximum power point tracking algorithm for partially shaded conditions, and an algorithm which optimizes photovoltaic (PV) cell size and arrangement along with the power electronic converter design for on-board solar charging. Thus, the proposed solutions in this research can help reduce distribution transformer aging as EV penetrations continue to rise and increase the environmental benefits of EVs through optimized solar charging.

Acknowledgments

I am overwhelmingly grateful to Almighty Allah for His mercy and provision in my life.

I would like to express my gratitude to my academic supervisor, Dr. Jennifer Bauman, for her supervision, advice, and guidance from the very early stage of this research until the writing phase of this thesis.

I genuinely thank my supervisory committee members, Dr. Ali Emadi and Dr. Mehdi Narimani, for their advice and guidance to ensure the appropriateness of my research progress.

Special thanks go to Dr. Rafael Kleiman, Chair, Department of Engineering Physics, McMaster University, for his kind research contributions in some of the publications.

I would also like to express my gratitude to my wife, my parents, and my siblings for their endless encouragement and support throughout my entire academic career. My son's birth a couple of months prior to the submission of this thesis inspired me more to give my best into the research and make the best out of the Ph.D.

Table of Contents

Chapter 1: Introduction.....	1
1.1. Background and Motivation	1
1.2. Research Contributions.....	3
1.2.1 Contribution 1	3
1.2.2 Contribution 2	4
1.2.3 Contribution 3	5
1.2.4 Contribution 4.....	6
1.3. Publications.....	7
1.3.1 Journal Publications	7
1.3.2 Conference Publications	8
1.4. Thesis Organization	8
Chapter 2: Vehicle-Directed Smart Charging Strategies to Mitigate the Effect of Long-Range EV Charging on Distribution Transformer Aging.....	13
2.1. Introduction.....	13
2.2. Research Methodology	18
2.2.1 Vehicle Data and Model	18
2.2.2 Grid Data.....	26
2.2.3 EV Charging Strategies.....	28
2.2.4 Transformer Aging Model	35
2.2.5 Simulation Process.....	38
2.3. Results And Discussion	39
2.3.1 Charging Profiles	39
2.3.2 Average Aging of 25 kVA Transformers	45
2.3.3 Average Aging of 37.5 kVA Transformers.....	50
2.3.4 Average Aging of 75 kVA Transformers	52
2.4. Conclusions.....	53
Chapter 2 References	55
Chapter 3: Solar-Charged Electric Vehicles: A Comprehensive Analysis of Grid, Driver, and Environmental Benefits.....	58
3.1. Introduction.....	58
3.2. Data Sources	65
3.2.1 Vehicle Data.....	65

3.2.2	Grid Data.....	67
3.2.3	Solar and Temperature Data	69
3.3.	SEV Modeling	72
3.3.1	Vehicle Modeling.....	72
3.3.2	On-Board Solar Cell Modeling	76
3.3.3	Modeling of Partial Shading	88
3.3.4	SEV Electrical Architecture and Challenges	91
3.3.5	Transformer Aging Model	94
3.3.6	Simulation Process.....	96
3.4.	Simulation Results and Discussion.....	99
3.4.1	Energy Use.....	99
3.4.2	Grid Benefits.....	100
3.4.3	Driver Benefits.....	109
3.4.4	Environmental Benefits.....	116
3.4.5	Economic Analysis	117
3.5.	SEV Future Trends	119
3.6.	Conclusions.....	124
	Chapter 3 References	126
Chapter 4: A Fast Parabolic-Assumption Algorithm for Global MPPT of Photovoltaic Systems Under Partial Shading Conditions		
4.1.	Introduction.....	134
4.2.	PV System Modeling	140
4.2.1	Single Diode Model	140
4.2.2	I-V & P-V Characteristics of PV Array Under PSCs	142
4.3.	Proposed Parabolic Assumption Algorithm.....	143
4.3.1	Mathematical Description of Parabolas	143
4.3.2	Parabolic Assumption for Partial Shading	144
4.3.3	Effect of Temperature Variation	152
4.4.	Simulation Results	152
4.4.1	Proposed PA Algorithm.....	152
4.4.2	Comparison to other MPPT Algorithms	160
4.4.3	Effect of Sensor Noise/Offset	163
4.4.4	Effect of PV Module Aging	165

4.5.	Experimental Results	168
4.6.	Conclusion	173
	Chapter 4 References	175
	Chapter 5: Optimization of PV Array and Power Electronics Design for On-Vehicle Solar Charging.....	179
5.1.	Introduction.....	179
5.2.	Optimum Power Electronic Architecture Selection.....	182
5.3.	Cell Size and Interconnection Optimization	186
5.3.1	Partial Shading Condition (PSC) Modeling on SEV	186
5.3.2	DC-DC Converter Efficiency Modeling	188
5.4.	Simulation and Results	191
5.5.	Conclusion	196
	Chapter 5 references	196
	Chapter 6: Conclusions and Future Work.....	198
6.1.	Conclusions.....	198
6.2.	Recommendation for Future Work	200

List of Figures

Fig. 2.1. Distribution of departure and arrival times, daily distance travelled, and simulated daily energy requirement for 150 logged drivers over 5 weekdays.....	19
Fig. 2.2. Distribution of departure and arrival times, daily distance travelled, and simulated daily energy requirement for 150 logged drivers over 2 weekend days.....	19
Fig. 2.3. Block diagram of vehicle model.....	22
Fig. 2.4. Logged vehicle speed and simulated battery SOC for one example logged day.	25
Fig. 2.5. Per house load profile without EV charging [31].	26
Fig. 2.6. Proposed RIW charging algorithm with RIW-FR and RIW-VR variants.	32
Fig. 2.7. Example of an RIW-FR charging algorithm for one driver on one day.	33
Fig. 2.8. Daily ambient temperature profile used for transformer aging model (from Toronto, Canada in July [37]).	35
Fig. 2.9. Simulation process summary	38
Fig. 2.10. Long-range EV and short-range EV simulated Monday load for 150 logged drivers (CRA charging strategy).....	40
Fig. 2.11. Long-range EV and short-range EV simulated Monday load for 150 logged drivers (TOU 7pm & 12am charging strategy).....	40
Fig. 2.12. Long-range EV and short-range EV simulated Monday load for 150 logged drivers (CBD charging strategy).....	41
Fig. 2.13. Long-range EV and short-range EV simulated Monday load for 150 logged drivers (Random charging strategy from [26]).	41
Fig. 2.14. Long-range EV and short-range EV simulated Monday load for 150 logged drivers (RIW-FR and RIW-VR charging strategies).	42
Fig. 2.15. Long-range EV and short-range EV simulated Monday load for 150 logged drivers (Idealized centralized smart-charging strategy [4],[6]).....	42
Fig. 2.16. Comparison of all charging strategies for 150 EV drivers on logged Monday evening for short-range EVs.	44
Fig. 2.17. Comparison of all charging strategies for 150 EV drivers on logged Monday evening for long-range EVs.	44
Fig. 2.18. Detailed charging load on Transformer 1 for logged Monday evening (long-range EV).....	44
Fig. 2.19. Average weekly equivalent aging factors for random charging and RIW-FR with different window start times (A) for short-range EVs.	46
Fig. 2.20. Average weekly equivalent aging factors for random charging and RIW-FR with different window start times (A) for long-range EVs.	46
Fig. 2.21. Average weekly equivalent aging factors for random charging and RIW-VR with different window start times (A) for short-range EVs.	46
Fig. 2.22. Average weekly equivalent aging factors for random charging and RIW-VR with different window start times (A) for long-range EVs.	47
Fig. 2.23. Weekly average transformer aging factors for different charging strategies across all EV penetration rates.....	48
Fig. 2.24. Weekly average transformer aging factors for different charging strategies across all EV penetration rates (zoomed in).	48

Fig. 2.25. Weekly average transformer aging factors for different charging strategies with 37.5 kVA transformer.	51
Fig. 2.26. Weekly average transformer aging factors for different charging strategies with 75 kVA transformer.	53
Fig. 2.27. Weekly average transformer aging factors for different charging strategies with 75 kVA transformer (zoomed-in).	53
Fig. 3.1. Distribution of departure and arrival times, daily distance travelled, and simulated daily energy requirement for 150 logged drivers over 5 weekdays.....	66
Fig. 3.2. Distribution of departure and arrival times, daily distance travelled, and simulated daily energy requirement for 150 logged drivers over 2 weekend days.....	67
Fig. 3.3. Monthly per house load profile without EV charging.	68
Fig. 3.4. Monthly solar radiation in Los Angeles for sunny and average cloud condition days.	70
Fig. 3.5. Monthly solar radiation in Detroit for sunny and average cloud condition days.	71
Fig. 3.6. Average daily ambient temperature profile for each month of the year in Los Angeles and Detroit.	71
Fig. 3.7. Block diagram of SEV vehicle model.	72
Fig. 3.8. Modeled relation between HVAC power use and trip average ambient temperature.	76
Fig. 3.9. Diagram of the spherical coordinate system used for calculating the projection cosine, $\cos\Psi$. The vector $V1$ points from the observer, O , towards the sun and is tilted by an angle θ_z from the zenith direction. The vector $V2$ is normal to the solar panel, which is tilted by an angle θ_t from the horizontal and rotated by an angle Φ around the zenith. The angle Ψ is the angle between $V1$ and $V2$	78
Fig. 3.10. Energy capture on an annual basis vs. tilt of a SEV panel (relative to horizontal) and vs. latitude, with latitude legend in degrees. The energy capture is referenced to the values for horizontal panels (i.e., 0° tilt) [43].	80
Fig. 3.11. Reference Chevy Bolt as solar-charged electric vehicle (SEV).	81
Fig. 3.12. Estimated CIGS cell efficiency as a function of cell temperature.	84
Fig. 3.13. Example case for partial shading modeling (structure on left side of vehicle).	89
Fig. 3.14. Monthly average zenith angle profile for Los Angeles and Detroit.	90
Fig. 3.15. Monthly partial shading solar radiation models for Los Angeles and Detroit.	91
Fig. 3.16. Two potential electrical architecture options for the proposed SEV.	94
Fig. 3.17. Summary of simulation process. This process is looped: for 150 drivers, for each day of the week, for each month of the day, for full sun, average cloud, and average cloud with partial shading conditions, and in two cities. This is also then rerun with solar radiation = 0 to represent the non-solar EV case.	97
Fig. 3.18. Vehicle speed and battery SOC for driver #1 over one example day, both for an EV without on-board solar, and the proposed SEV.	98
Fig. 3.19. Average daily radiation and ambient temperature profile for each month of the year in Saudi Arabia.....	100

Fig. 3.20. Household and EV charging load for 150 EVs and 150 houses for non-solar EV, SEV on a day with full sun, average cloud conditions, and average cloud conditions with partial shading (CRA charging).....	101
Fig. 3.21. Household and EV charging load for one transformer for non-solar EV, SEV on a sunny day, SEV on a day with average clouds, and SEV on a day with average clouds and partial shading (CRA charging).....	102
Fig. 3.22. Generated grid energy required to charge 150 EVs in each month of the year in Los Angeles and Detroit (CRA charging).....	104
Fig. 3.23. Annual average monthly generated grid energy required to charge 150 EVs (CRA charging).....	105
Fig. 3.24. Average monthly equivalent aging factors for non-solar EVs and SEVs in Detroit and Los Angeles (LA) (CRA charging).....	105
Fig. 3.25. Average annual equivalent aging factors for non-solar EVs and SEVs in Detroit and Los Angeles (LA) (CRA charging).....	106
Fig. 3.26. Household and EV charging load for 150 EVs and 150 houses using CBD charging strategy.....	108
Fig. 3.27. Average annual equivalent aging factors for non-solar EVs and SEVs for CRA and CBD EV charging strategies.....	109
Fig. 3.28. Simulated average grid energy consumption in grid kWh/100km in Los Angeles and Detroit.....	110
Fig. 3.29. Simulated annual average grid energy consumption in grid kWh/100km.....	111
Fig. 3.30. Daily solar energy range extension in Los Angeles and Detroit.....	112
Fig. 3.31. SEV effect on monthly EV charging costs per driver in Los Angeles and Detroit.....	115
Fig. 3.32. SEV effect on annual EV charging costs per driver.....	115
Fig. 3.33. CO ₂ production to charge 150 EVs monthly in Los Angeles and Detroit.....	117
Fig. 3.34. Annual CO ₂ production to charge 150 EVs.....	117
Fig. 4.1. Single-diode model of a solar cell.....	140
Fig. 4.2. Example of partial shading condition on a 4S1P PV array.....	143
Fig. 4.3. Multiple local peaks during partial shading condition.....	143
Fig. 4.4. Parabolas at different positions and their respective equations.....	144
Fig. 4.5. Justification of Parabolic Assumption (PA).....	145
Fig. 4.6. Schematic of the PV system.....	146
Fig. 4.7. Flowchart of the proposed PA GMPPT algorithm.....	147
Fig. 4.8. Application of Parabolic Assumption (PA) method on I-V characteristic curve during PSC.....	149
Fig. 4.9. I-V characteristic curves for four different PSC patterns.....	154
Fig. 4.10. P-V characteristic curves for four different PSC patterns.....	154
Fig. 4.11. Simulation of the performance of the proposed PA algorithm under PSC patterns 1 and 2.....	156
Fig. 4.12. Simulation of the performance of the proposed PA algorithm under PSC patterns 3 and 4.....	157
Fig. 4.13. Actual and approximated I-V and P-V characteristic curves for a 4S2P array configuration with PSC patterns 2 and 3.....	158

Fig. 4.14. Simulation of the performance of the proposed PA algorithm for a 4S2P configuration under PSC patterns 2 and 3.	160
Fig. 4.15. Dynamic performance comparison of the proposed PA, PSO, CFPSO, and Modified HC algorithms under all 4 PSC patterns.	162
Fig. 4.16. Sensitivity analysis of the proposed PA algorithm compared to PSO and CFPSO for various noise levels and offsets.	165
Fig. 4.17. Impact of aging on PV modules over 10 and 20 years of life.	166
Fig. 4.18. Simulation of the performance of the proposed PA algorithm for a 4S1P configuration consisting of 20 years old modules under PSC patterns 1 and 2.	168
Fig. 4.19. Experimental setup with alternate configuration for steady output voltage operation.	169
Fig. 4.20. (a) Experimental Setup, (b) TMS320F28379D Microcontroller, and (c) Boost Converter Evaluation Board KIT-CRD-3DD12P.	169
Fig. 4.21. Experimental performance of the proposed PA algorithm under PSC patterns 1 and 2.	170
Fig. 4.22. Experimental performance of the proposed PA algorithm under PSC patterns 3 and 4.	172
Fig. 4.23. Example of voltage, current, and efficiency profile from SAS interface.	173
Fig. 5.1. Two potential electrical architecture options for the proposed SEV [1].	180
Fig. 5.2. Efficiency map for bidirectional converter in Option 1.	184
Fig. 5.3. Efficiency map for dedicated boost converter in Option 2 (Rooftop PV).	184
Fig. 5.4. Efficiency map for dedicated boost converter in Option 2 (Hood top PV).	185
Fig. 5.5. Monthly solar radiation and temperature in Los Angeles.	185
Fig. 5.6. Performance comparison of the two considered PV architectures.	186
Fig. 5.7. Monthly partial shading solar radiation models for Los Angeles.	187
Fig. 5.8. Simplified roof and hood of a SEV.	187
Fig. 5.9. Outcome of GA for Roof.	191
Fig. 5.10. Optimized array for Roof.	192
Fig. 5.11. Outcome of GA for Hood.	193
Fig. 5.12. Optimized array for Hood.	194

List of Tables

Table 2.1. Summary of Curve Fitting Parameters for Driving Data	21
Table 2.2. Summary of Investigated EV Charging Methods	29
Table 2.3. Comparison of Charging Energy Demand For Long- And Short-Range EVs For 150 Drivers	42
Table 3.1. Electricity Price Rate In LA & Detroit [73] [74]	114
Table 4.1. Specifications of Sunpower SPR-200-WHT-U	142
Table 4.2. System Modeling Parameters	153
Table 4.3. Details of PSC Patterns	153
Table 4.4. Comparison of Proposed PA Algorithm With Other Methods	163
Table 4.5. Tracking Efficiency (%) Comparison of The Proposed PA Algorithm For Non- Aged And Aged PV Modules	167
Table 4.6. Experimental Results of The Proposed PA GMPPT Algorithm	173
Table 5.1. Specifications of the considered CIGS PV cell.	182
Table 5.2. Specifications of the upward facing PV panels.	183
Table 5.3. Specifications of synchronous buck converter.....	190
Table 5.4. Energy comparison for optimized and unoptimized array for roof.....	195
Table 5.5. Energy comparison for optimized and unoptimized array for hood.	195
Table 5.6. Total energy comparison for optimized and unoptimized array.	195

Chapter 1: Introduction

1.1. Background and Motivation

The demand of electric vehicles (EVs) is rapidly increasing due to diminishing fossil fuel reserves, greenhouse gas emissions from transportation, and local urban air pollution [1]. Even though range issues and high costs have restricted the adoption of EVs to date, the recent introduction of long-range EVs at reasonable prices [2], [3] has the potential to accelerate the transition to EVs in the near future. Despite the many advantages of transitioning to EVs, there is a concern that EV charging could severely affect the electric grid if many EVs charge at the same time as the grid is already overloaded at times. Although increased EV charging will have an impact on many aspects of the grid, studies have shown that local distribution systems, particularly distribution transformers, are the most vulnerable [4]-[9] as the distribution networks have not been developed foreseeing high numbers of EV loads. Depending on the charging rate, adding an EV charging load to a local distribution circuit is equal to adding one or more households to the system. Overloading induced by EV charging can cause overheating, leading to faster aging and eventual early failure of the distribution transformers, because most of them are only sized for the peak loads of the connected residences [4]-[9]. Considering the distribution transformers are not ready to accept these large loads, some suitable charging strategy is needed to reduce the need to replace distribution transformers as EV penetration rates rise.

Any plug-in vehicle charging strategy that varies the charging time and/or rate from the default approach of charging, i.e., charging at full rate as soon as the plug is connected is referred to as "smart-charging." There are two types of smart-charging strategies: centralized and distributed. Centralized strategies transmit car and grid data to a central server, which can determine which vehicles to charge at any given time using a variety of methods. Recently proposed methods include controlling EV charging to: match the aggregate load to a pre-determined power profile to improve grid stability [10], optimize the cost or speed of charging [11], minimize and flatten network peak loads, [4],[6],[12]-[14] or simultaneously minimize network loads and the number of on-off switchings of EV charging power [15].

Centralized smart-charging methods are computationally expensive and may not scale effectively to large numbers of EVs. As a result, several distributed strategies have been developed [16]-[18], in which local smart agents make charging decisions based on transmitted car and grid data. Both centralized and distributed smart-charging require grid sensors, communication networks, local or centralized smart agents, connected and controllable electric vehicle supply equipment (EVSE), and a method to obtain often proprietary vehicle battery state-of-charge (SOC) data from a variety of EV models [7] to function, which make both of these smart charging strategies very complicated and sometimes unfeasible for implementation. Hence, with the increase of long-range EVs either worldwide or in neighborhood clusters, it is crucial to develop alternative but effective

charging strategies which can play a vital role in mitigating the distribution transformer aging without requiring any extra intelligent sensors, smart agents, or communication networks. This thesis focuses on two ways to reduce the distribution transformer heating and aging: Random-in-window (RIW) smart charging and large-scale on-board solar charging. Combining the advantages of RIW and on-board solar charging, mitigation of transformer aging can be helped to a great extent with added driver and environment benefits.

1.2. Research Contributions

1.2.1 Contribution 1

To address the necessity of a charging schemes to reduce distribution transformer aging under increasing EV loads, this research proposes Random-in-window (RIW) smart charging strategy. RIW is a vehicle-directed smart charging concept, which automatically smooths out charging peaks by taking advantage of the inherent randomness already present within a group of EVs, i.e., a variety of next-day departure times and a variety of energy needs to be fully charged by the departure time. RIW performs approximately as good as a fully controlled centralized smart-charging algorithm at EV penetration rates up to 60% for long-range EVs and 70% for short-range EVs in the event of distribution transformer aging reduction. Yet it can easily be implemented as the EV just needs a software update.

1.2.2 Contribution 2

While RIW can benefit the grid to a great extent, this research further contributes to improve the scenario by introducing means to benefit the driver and environment in addition to reducing transformer aging. The full environmental benefits of EVs can only be realized when charging energy is generated with zero or low CO₂ emissions, e.g., wind, solar, hydro, etc. Thus, renewable energy generation and increased EV adoption must go together. Solar energy has become a dependable source of renewable energy because of seldom maintenance and no waste production, making it an entirely environment-friendly process. Thin-film solar panels can be installed on the vehicle body, which can charge the EV battery throughout the day, resulting in less charging energy required from the grid. Thus, this research proposes the concept of a large-scale solar-charged electric vehicle (SEV) with low-cost flexible thin film PV cells integrated directly onto the steel of all upwards-facing body panels of the vehicle i.e., roof, hood, and trunk.

The surface of the vehicle upward-facing body might not be that large, so the charging power could be low. But the low charging power is multiplied by the long length of daytime the vehicle is outside. As a result, the resulting charging energy is not low anymore and can be a significant portion of the daily energy use of the vehicle. With the analyses of solar energy capture of 150 drivers to realize grid, driver, and environmental benefits in Los Angeles and Detroit over the course of a full year, the simulations predict net annual vehicle energy use reductions of 21.5% in Los Angeles and of 17.5% in Detroit and 50% transformer aging reduction in

either city at 80% EV penetration for average cloud conditions, compared to a non-solar EV. The peak solar range extension is 47 km/day in Detroit on a sunny day in May and charging costs are reduced by about 20% for average cloud conditions.

1.2.3 Contribution 3

The system level analysis of real benefits to grid, driver, and environment motivates the further research to focus on the design and manufacturing challenges of SEVs. One of the main challenges of making a SEV concept into reality is extracting maximum solar energy under partial shading conditions (PSCs) on a fast-moving vehicle.

PSCs can often occur from shadows of clouds, buildings, trees, etc. PSCs produce multiple peaks on respective the I-V and P-V curves. Finding the global maximum power point (GMPP) is difficult in this case for conventional maximum power point tracking (MPPT) algorithms like hill-climbing [19] due to the possibility of getting trapped at a local peak, or like particle swarm optimization (PSO) [20] due to slow convergence. High GMPP convergence speeds to minimize energy loss during PSCs are critical for emerging mobile PV applications such as solar-charged electric vehicle [21] or aircraft [22]. This research proposes a completely new approach of a software-based GMPPT algorithm that analytically calculates the GMPP near-exactly during PSCs using exactly S current measurements, where S is the number of series modules in the array, and hence only S steps are required. The proposed algorithm's performance has first been evaluated using MATLAB/Simulink simulations, followed by experimental

verification. The results reveal very fast GMPP tracking with minimal tracking energy loss, with an experimental tracking efficiency over 99.6% for all PSC patterns tested.

1.2.4 Contribution 4

Optimization of PV cell interconnections, i.e., series and parallel connections in the array and power electronics design for on-vehicle solar charging is also an equally important design requirement. The upper body mounted PV panel should have the optimum cell size with optimum number of such cells in series and parallel to ensure maximum power extraction, especially in the event of PSCs. As PV cells come in different sizes, the optimum number of such cells and their possible interconnection depend on a couple of factors, e.g., current density of the cell (mA/cm^2), area of the upward facing PV panel, DC-DC converter efficiency, and partial shading modeling, etc. As there could be numerous combinations of these factors, an optimization algorithm needs to be used to find the optimum cell size and their possible interconnection configurations. This research proposes a novel approach to optimize the PV array interconnection considering power electronic converter efficiency using Genetic Algorithm (GA) for higher system efficiency, lower cost, and lower mass. This study has shown the proposed design solution could save up to 3% PV energy compared to the assumed random unoptimized array.

It is evident that RIW is an excellent and easily implementable decentralized vehicle directed smart charging strategy comparable to a fully controlled

centralized smart-charging algorithm at moderate EV penetration rates in the event of distribution transformer aging reduction. While this certainly benefits the grid, a solar-charged electric vehicle can add advantages such as charging cost savings, range extension, and CO₂ emission reduction. Combining RIW and the SEV concept and providing solutions to the design and engineering problems related to SEV, this research can help the grid, drivers, and the environment.

1.3. Publications

The thesis has been written in the “Sandwich Thesis” format, where the chapters correspond to individual journal articles. The articles have been slightly modified to comply with the thesis format keeping the main contents of the articles unchanged. The next section shows the manuscripts published or submitted in reputed journals and conferences from this thesis research. Chapter 2, 3, and 4 have been prepared from journal publications 1, 2, and 3 respectively and Chapter 5 has been prepared from the “In-progress” article 4 from Section 1.3.1.

1.3.1 Journal Publications

1. M. H. Mobarak and J. Bauman, "Vehicle-Directed Smart Charging Strategies to Mitigate the Effect of Long-Range EV Charging on Distribution Transformer Aging," in *IEEE Transactions on Transportation Electrification*, vol. 5, no. 4, pp. 1097-1111, Dec. 2019, doi: 10.1109/TTE.2019.2946063.

2. M. H. Mobarak, R. N. Kleiman* and J. Bauman, "Solar-Charged Electric Vehicles: A Comprehensive Analysis of Grid, Driver, and Environmental

Benefits," in *IEEE Transactions on Transportation Electrification*, vol. 7, no. 2, pp. 579-603, June 2021, doi: 10.1109/TTE.2020.2996363.

*Fig. 10 and the corresponding description in Section IIIB is contributed by Dr. R. Kleiman.

3. M. H. Mobarak and J. Bauman, " A Fast Parabolic-Assumption Algorithm for Global MPPT of Photovoltaic Systems Under Partial Shading Conditions," in *IEEE Transactions on Industrial Electronics*, Early Access.

4. M. H. Mobarak and J. Bauman, "Optimization of PV Array and Power Electronics Design for On-Vehicle Solar Charging," In progress to be submitted in *IEEE Transactions on Transportation Electrification*.

1.3.2 Conference Publications

1. M. H. Mobarak, R. Kleiman and J. Bauman, "Investigation of Grid Benefits from a Solar-Powered Electric Vehicle Using Real-World Driving Data," *2019 IEEE Transportation Electrification Conference and Expo (ITEC)*, 2019, pp. 1-6, doi: 10.1109/ITEC.2019.8790519.

1.4. Thesis Organization

This thesis presents a combination of system-level and device-level research used to propose vehicle directed smart-charging and on-board solar charging to mitigate distribution transformer aging. The thesis is organized as follows:

Chapter 2 describes the issues surrounding smart charging, the impact of various charging schemes on transformer aging, and proposes a vehicle-directed

smart charging strategy, namely Random-In-Window (RIW), which has two variants: fixed rate charging (RIW-FR) and variable rate charging (RIW-VR) that require no additional infrastructure or communication networks compared to the usual centralized or distributed smart-charging schemes. A detailed modeling of an EV in MATLAB & Simulink, modeling of transformer aging, and use of driving patterns of 150 unique drivers over a summer week have been used to carry out the outlined research.

Chapter 3 proposes a large-scale SEV concept that can provide significant benefits to the grid, drivers, and the environment. Detailed modeling is described, including modeling different solar radiations at different latitudes over a year, dealing with various vehicle directions, and partial shading. Furthermore, detailed driving data of 150 drivers is used to get realistic results. This detailed analysis of the advantage of using SEVs shows significant benefits, indicating that further research is justified to address the design and manufacturing challenges of SEVs.

One challenge with SEVs is extracting the maximum solar energy at all times, even when a vehicle is moving with partial shading conditions. Since many global maximum power point tracking (GMPPT) algorithms take numerous steps, and related time, to reach the GMPP, Chapter 4 proposes a totally novel approach to very quickly find the GMPP under partial shading conditions with a low fixed number of steps. This chapter includes both simulation and experimental results supporting the effectiveness of this novel GMPPT algorithm, which can be used on commercial SEVs, and also has general advantages for grid applications.

To further optimize the design of a large-scale SEV, Chapter 5 proposes a novel method using genetic algorithm (GA) to optimize the PV array while also considering the current density of the cell (mA/cm^2), area of the upward facing PV panel, DC-DC converter efficiency as functions of input and output voltages and currents, and partial shading modeling, etc. to ensure optimum cell size and cell interconnections for high system efficiency, lower cost, and lower mass.

Chapter 6 concludes the thesis with a summary of the entire research and provides recommendations for future research work.

Chapter 1 References

- [1] W.-J. Guan, X.-Y. Zheng, K. F. Chung, and N.-S. Zhong, “Impact of air pollution on the burden of chronic respiratory diseases in China: time for urgent action,” *The Lancet*, vol. 388, no. 10054, pp. 1939–1951, 2016.
- [2] Online: <https://www.chevrolet.com/electric/bolt-ev-electric-car> [Accessed May 2019]
- [3] Online: <https://www.tesla.com/model3> [Accessed May 2019]
- [4] Q. Gong, S. Midlam-Mohler, V. Marano, and G. Rizzoni, “Distribution of PEV charging resources to balance transformer life and customer satisfaction,” *Proceedings of the 2012 IEEE International Electric Vehicle Conference*, Greenville, SC, USA, 2012.
- [5] Q. Gong, S. Midlam-Mohler, V. Marano, and G. Rizzoni, “Study of PEV charging on residential distribution transformer life,” *IEEE Trans. on Smart Grid*, vol. 3, no. 1, pp. 404-412, March 2012.
- [6] Q. Gong, S. Midlam-Mohler, E. Serra, V. Marano, and G. Rizzoni, “PEV charging control considering transformer life and experimental validation of a 25 kVA distribution transformer,” *IEEE Trans. on Smart Grid*, vol. 6, no. 2, pp. 648-656, March 2015.
- [7] J. Quirós-Tortós, L. Ochoa, S. Alnaser, and T. Butler, “Control of EV charging points for thermal and voltage management of LV networks,” *IEEE Trans. on Power Systems*, vol. 31, no. 4, pp. 3028-3039, July 2016.
- [8] M. Gray and W. Morsi, “Power quality assessment in distribution systems embedded with plug-in hybrid and battery electric vehicles,” *IEEE Trans. on Power Systems*, vol. 30, no. 2, pp. 663-671, March 2015.
- [9] M. ElNozahy and M. Salama, “A comprehensive study of the impacts of PHEVs on residential distribution networks,” *IEEE Trans. on Sustainable Energy*, vol. 5, no. 1, pp. 332-342, Jan. 2014.
- [10] V. del Razo, C. Goebel, and H. Jacobsen, “Vehicle-originating-signals for real-time charging control of electric vehicle fleets,” *IEEE Trans. on Transportation Electrification*, vol. 1, no. 2, pp.150-167, Aug. 2015.
- [11] R. Abousleiman and R. Scholer, “Smart charging: system design and implementation for interaction between plug-in electric vehicles and the power grid,” *IEEE Trans. on Transportation Electrification*, vol. 1, no. 1, pp.18-25, June 2015.

- [12] J. Hu, S. You, M. Lind, and J. Østergaard, “Coordinated charging of electric vehicles for congestion prevention in the distribution grid,” *IEEE Trans. on Smart Grid*, vol. 5, no. 2, pp. 703-711, March 2014.
- [13] E. Veldman and R. Verzijlbergh, “Distribution grid impacts of smart electric vehicle charging from different perspectives,” *IEEE Trans. on Smart Grid*, vol. 6, no. 1, pp. 333-342, Jan. 2015.
- [14] N. Mehboob, M. Restrepo, C. Canizares, C. Rosenberg, and M. Kazerani, “Smart operation of electric vehicles with four-quadrant chargers considering uncertainties,” *IEEE Trans. on Smart Grids*, Early Access Article, 2018.
- [15] B. Sun, Z. Huang, X. Tan, and D. Tsang, “Optimal scheduling for electric vehicle charging with discrete charging levels in distribution grid,” *IEEE Trans. on Smart Grid*, vol. 9, no. 2, pp. 624-634, March 2018.
- [16] A. Hilshey, P. Hines, P. Rezaei, and J. Dowds, “Estimating the impact of electric vehicle smart charging on distribution transformer aging,” *IEEE Trans. on Smart Grid*, vol. 4, no. 2, pp. 905-913, June 2013.
- [17] O. Ardakanian, S. Keshav, and C. Rosenberg, “Real-time distributed control for smart electric vehicle chargers: from a static to a dynamic study,” *IEEE Trans. on Smart Grid*, vol. 5, no. 5, pp. 2295-2305, Sept. 2014.
- [18] S. Weckx, R. D’Hulst, B. Claessens, and J. Driesen, “Multiagent charging of electric vehicles respecting distribution transformer loading and voltage limits,” *IEEE Trans. on Smart Grid*, vol. 5, no. 6, pp. 2857-2867, Nov. 2.
- [19] P. Van den Heever, S. Oberholzer, and J. Enslin, “High-efficient solar panel/wind turbine converter with maximal power control,” in *Proc. Eur. Conf. Power Electron. Appl.*, 1989, pp. 663-668.
- [20] Yu et al., “An overall distribution particle swarm optimization MPPT algorithm for photovoltaic system under partial shading,” *IEEE Trans. Ind. Electron.*, vol. 66, no. 1, Jan. 2019.
- [21] M. H. Mobarak, R. Kleiman, and J. Bauman, “Solar-charged electric vehicles: a comprehensive analysis of grid, driver, and environmental benefits,” *IEEE Trans. Transp. Elec.*, Early Access, May 2020.
- [22] A. Diab-Marzouk and O. Trescases, “SiC-based bidirectional cuk converter with differential power processing and MPPT for a solar powered aircraft,” *IEEE Trans. Transp. Elec.*, vol. 1, pp. 369-381, 2015.

Chapter 2: Vehicle-Directed Smart Charging Strategies to Mitigate the Effect of Long-Range EV Charging on Distribution Transformer Aging

2.1. Introduction

Electric vehicles have the potential to significantly reduce greenhouse gas emissions, regulated emissions which cause local air pollution and negative health effects [1], and society's reliance on fossil fuels. Though range concerns and high costs have somewhat limited the adoption of electric vehicles (EVs) to date, the recent introduction of long-range EVs with moderate costs [2], [3] has the potential to trigger a more widespread transition to EVs in the near future. Although increased EV charging will affect multiple aspects of the grid, research has shown that local distribution systems, especially distribution transformers, are of primary concern [4]-[9]. Adding an EV charging load to a local distribution circuit is equivalent to adding one or more homes to the system, depending on the charging rate. Since most distribution transformers are sized for only the peak loads of the connected homes, overloading caused by EV charging can cause overheating, leading to accelerated aging and eventual early failure [4]-[9]. This chapter investigates the effect of long-range EV charging on distribution transformer aging using real world driving data, and proposes an effective smart-charging strategy that does not require any additional distribution system infrastructure or communication networks.

The term “smart-charging” refers to any plug-in vehicle charging strategy that changes the charging time and/or rate from the default strategy: charging at the full rate as soon as the plug is connected. Smart-charging strategies can be categorized as centralized or distributed. Centralized strategies transmit vehicle and grid data to a central server that can use a variety of methods to determine which vehicles to charge at any given time. Some recently proposed algorithms include controlling EV charging to: match the aggregate load to a pre-determined power profile to improve grid stability [10], optimize the cost or speed of charging [11], minimize and flatten network peak loads [4],[6],[12]-[14] or simultaneously minimize network loads and the number of on-off switchings of EV charging power [15]. Furthermore, [16] uses genetic algorithms to minimize both charging cost and transformer peak-to-average load ratio and [17] uses game theory to determine optimal charging schedules to maximize transformer lifetime. However, centralized smart-charging schemes are computationally expensive, and may not scale well to large numbers of EVs. Thus, numerous distributed strategies have also been proposed, where local smart agents use transmitted vehicle and grid data to make charging decisions. For example, [18] uses local transformer temperature data in addition to vehicle data to control EV charging to limit transformer aging, [19] measures the capacity of the local network in real time to ensure EV charging does not cause an overload, and [20] uses a multi-agent scheme to limit transformer loading and stabilize local voltages. Furthermore, [21] uses a decentralized strategy

based on the Frank-Wolf algorithm to minimize cost while respecting voltage and substation capacity limits.

However, these centralized and distributed smart-charging strategies require significant infrastructure to operate [7], including: grid sensors, communication networks, local or centralized smart agents, connected and controllable electric vehicle supply equipment (EVSE), and a method to obtain often proprietary vehicle battery state-of-charge (SOC) data from a variety of EV models. As the smart grid evolves, this infrastructure may become available if viable business models are developed; however, if long-range EV adoption increases either globally or in neighborhood clusters before these fully-controllable charging systems are in place, what is the best alternative? This chapter defines *Vehicle-Directed Smart Charging* as charging strategies that can be implemented by individual EVs without the need for grid sensors, communication networks, smart agents, connected and controllable EVSEs, and vehicle battery SOC measurements. This chapter uses a real-world dataset of 150 unique drivers to investigate the effects of long-range EV charging on distribution transformer aging, using both known *Vehicle-Directed Smart Charging* strategies, and two newly proposed *Vehicle-Directed Smart Charging* strategies based on randomness.

Obtaining detailed driving data for smart-charging studies has been notoriously difficult [9]. Many previous studies have used the 2009 National Household Travel Survey (NHTS), creating probability distribution functions to represent daily mileage and home arrival times [9],[18],[21], with many works

using Monte Carlo simulations to generate individual trips [6],[8],[9],[22],[23]. The limitation to using large driving surveys like the NHTS for smart-charging studies is that individual driving habits get absorbed into probability distribution functions, erasing the link between when a person actually drove, how fast they drove, how far they drove, and when they returned home. Other studies have used a German driving survey of 500 households [10], a Copenhagen driving survey of 18 vehicles [12], a Netherlands driving survey with 25 drivers extracted [13], and a Denmark driving survey [24]. These smaller surveys still do not provide any information on how each driver drove (i.e., city or highway) meaning estimates of energy use must be based on assumptions of constant kWh/km rates. However, calculating accurate energy use while driving is critical since this will directly affect the battery SOC upon arrival home, and thus the amount of charging energy required. Other work has used even more general assumptions: [19] assumes departure after 6am and arrival after 4pm with Poisson distributions with all EVs having fully discharged batteries, [15] assumes a charging window from 6pm to 8am with all EVs needing 6 hours of charging at 3.3kW, and [16] assumes daily mileage with normal distribution around a mean of 55km. Furthermore, [25] assumes a normal distribution around 8am work start time and 5pm work end time with NHTS average daily driving distance, [26] uses an EPRI report based on stochastic modeling of NHTS data, and [27] builds stochastic models based on logging two EV charging stations.

The highest-quality vehicle data for smart-charging studies is logged vehicle data, as individual driving times are precise, and linked to the individual's driving habits. Vehicle models can be used to simulate the logged driving speed profile, so that accurate ending SOCs can be calculated for each day. Reference [5] uses logged data from 9 drivers, [7] uses logged data from 8 drivers, [14] uses stochastic modeling based on 11 logged drivers and a UK Travel Survey, and [28] uses logged data for 10 drivers. Reference [29] uses the largest set of logged data in the prior work with 76 drivers, but considers only short-range plug-in vehicles (Toyota Prius with 4kWh battery, Chevrolet Volt with 16kWh battery, and Nissan Leaf with 24kWh battery) and only studies the effect of uncontrolled charging on the grid. In this chapter, 150 drivers were logged for one week in Toronto, Canada to obtain a large detailed dataset for a very accurate smart-charging analysis. The logged vehicles were conventional internal combustion engine (ICE) vehicles, meaning the drivers could drive exactly as they normally would with no EV range limitations. It is common in other works, such as all studies using NHTS data, to assume driving habits remain the same from ICE vehicles to EVs. This assumption is especially relevant in this chapter since the focus is on long-range EVs, which people can drive more like ICE vehicles due to reduced range concerns compared to shorter-range EVs. Thus, this chapter takes a forward-looking approach by analyzing the charging needs of the long-range Chevrolet Bolt [2] with a 60kWh battery, in contrast to most studies that use EV battery sizes from 4kWh to 24kWh [5], [7], [9], [12]-[15], [19], [21], [22], [25].

The main contributions of this chapter are:

- 1) Investigation of long-range EV (60kWh battery) charging impacts on distribution transformer aging, with a comparison to the often-considered short-range EV (20kWh battery),
- 2) Two proposed *Vehicle-Directed Smart Charging* strategies (see Section 2.2) that require no additional infrastructure or communication networks compared to centralized or distributed smart charging schemes, and
- 3) Analysis of the above scenarios using a real world logged dataset of 150 unique drivers over one week.

Section 2.2 describes the research methodology, including the vehicle data and model, the grid data, the smart-charging strategies considered, the transformer aging model, and the simulation process. Section 2.3 presents the simulation results and discussion, and Section 2.4 summarizes and concludes the chapter.

2.2. Research Methodology

2.2.1 Vehicle Data and Model

This study uses one week of logged vehicle data from 150 drivers of ICE vehicles in Toronto, Canada. The logged data consists of time and date-stamped trips along with the second-by-second vehicle speeds of each trip. The data is obtained from a logger plugged into the on-board diagnostic port of each participant's vehicle to log CANbus (controller-area-network) signals. Since GPS and altitude data is not available, it is assumed that road grade is zero and that the last trip of the day returned the vehicle home, where all charging occurs. MATLAB

scripts were used to organize the data into driving days, which were assumed to start at 12am. Figs. 2.1 and 2.2 show the driving habits of the group for the 5 weekdays and 2 weekend days logged along with curves modeled to fit each dataset. The simulated energy use is based on a Chevrolet Bolt vehicle model driving the logged cycles; this vehicle model is described in detail below.

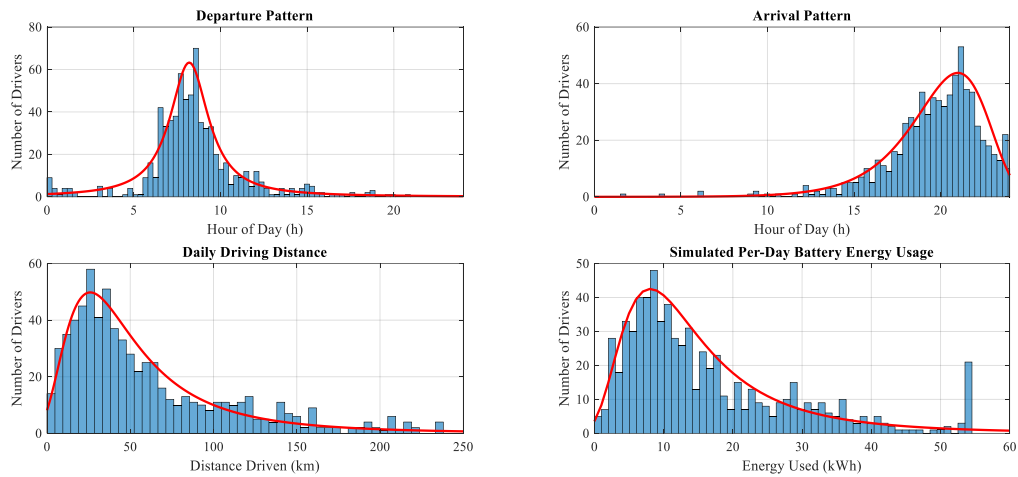


Fig. 2.1. Distribution of departure and arrival times, daily distance travelled, and simulated daily energy requirement for 150 logged drivers over 5 weekdays.

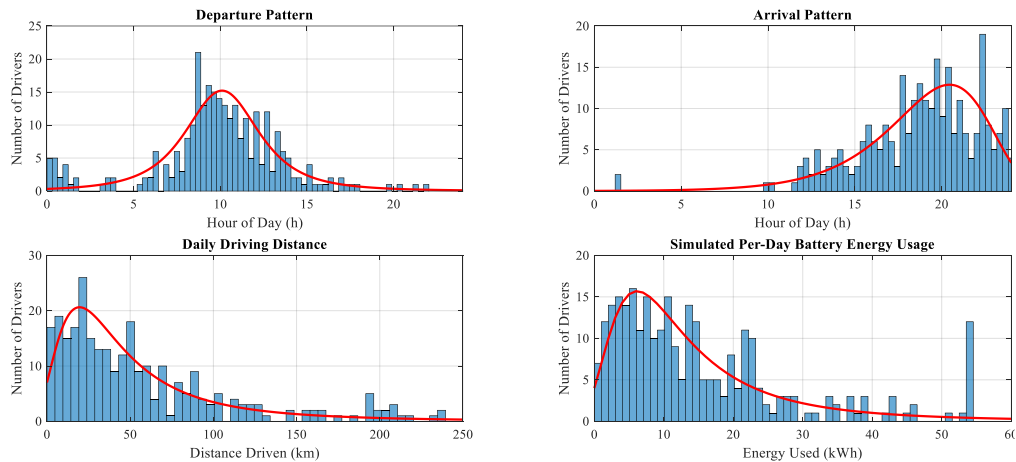


Fig. 2.2. Distribution of departure and arrival times, daily distance travelled, and simulated daily energy requirement for 150 logged drivers over 2 weekend days

The departure times are best represented by a t location-scale distribution, which is useful for modeling data distributions with heavier tails (more prone to outliers) than the normal distribution. The probability density function of the t location-scale distribution is shown in (1):

$$f(x) = \frac{\Gamma\left(\frac{v+1}{2}\right)}{\sigma\sqrt{v\pi}\Gamma\left(\frac{v}{2}\right)} \left[\frac{v + \left(\frac{x-\mu}{\sigma}\right)^2}{v} \right]^{-\left(\frac{v+1}{2}\right)} \quad (1)$$

where Γ is the gamma function, and all other parameters are listed in Table 2.1.

The arrival times are best represented by MATLAB's extreme value distribution, with the probability density function defined as

$$f(x) = \sigma^{-1} \exp\left(\frac{x-\mu}{\sigma}\right) \exp\left(-\exp\left(\frac{x-\mu}{\sigma}\right)\right) \quad (2)$$

Both the daily driving distance and simulated per-day battery energy use data are best represented by MATLAB's generalized extreme value distribution, given as

$$f(x) = \sigma^{-1} \exp\left(-\left(1+k\frac{(x-\mu)}{\sigma}\right)^{\frac{1}{k}}\right) \left(1+k\frac{(x-\mu)}{\sigma}\right)^{-1-\frac{1}{k}} \quad (3)$$

Table 2.1 provides all parameters to model the eight distributions, plus a scaling factor, m . Since each probability distribution function sums to one, a scaling factor is used on each plot to scale the curve to the units shown in Figs. 2.1 and 2.2. The probability distribution equations in (1)-(3) are widely known equations and

Table 2.1. Summary of Curve Fitting Parameters for Driving Data

Dataset	Distribution Type	Weekday Parameters	Weekend Parameters
Departure Time (h)	T location-scale	$\mu = 8.2$ $\sigma = 1.3$ $v = 1.2$ $m = 250$	$\mu = 10.1$ $\sigma = 2.26$ $v = 2.5$ $m = 95$
Arrival Time (h)	Extreme value	$\mu = 21$ $\sigma = 2.1$ $m = 250$	$\mu = 20.45$ $\sigma = 2.77$ $m = 97$
Daily Driven Distance (km)	Generalized extreme value	$\mu = 33.45$ $\sigma = 27.19$ $k = 0.3339$ $m = 3500$	$\mu = 28.2$ $\sigma = 26.9$ $k = 0.41$ $m = 1400$
Daily Simulated Energy Use (kWh)	Generalized extreme value	$\mu = 9.83$ $\sigma = 7.19$ $k = 0.289$ $m = 800$	$\mu = 8.18$ $\sigma = 7.18$ $k = 0.348$ $m = 290$

have been used in this research in MATLAB & Simulink for distribution pattern generation as directed by MathWorks webpage. Note that the simulated battery energy use for this base case assumes a 2 kW accessory power load, and a useable battery capacity of 54 kWh, thus there is a spike in the histograms at 54 kWh energy use to account for the ICE vehicles that drove further than the Chevrolet Bolt model could drive.

A forward-looking vehicle model of the Chevrolet Bolt EV was created in MATLAB/Simulink, as described below. The model was validated to be within 1.6% of EPA energy consumption test data on city and highway drive cycles, as described in [30]. Fig. 2.3 shows a block diagram of the three top-level blocks in the model: driver, controller, and vehicle plant.

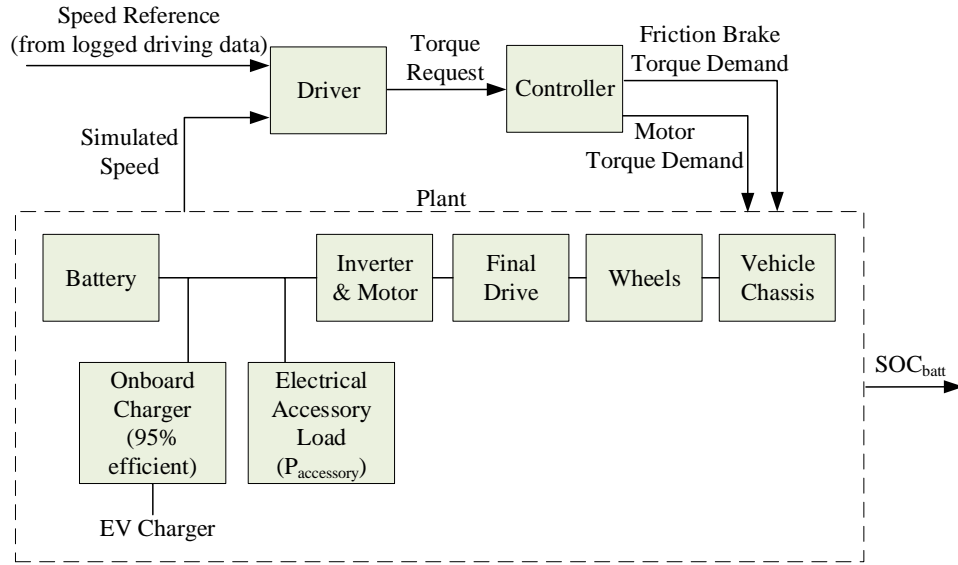


Fig. 2.3. Block diagram of vehicle model.

The driver is modeled as a PI feedback loop so that the driver torque request ensures that the simulated vehicle speed closely follows the speed reference from the logged drive cycles. The controller block generates the motor torque demand and friction brake demand subject to the driver torque request and the motor speed-torque limits. In the plant model, the vehicle speed in m/s at the next simulation step, $v_{chas}(t+1)$, is calculated from the force out of the wheel block and the chassis aerodynamic losses, as shown in (4):

$$v_{chas}(t+1) = v_{chas}(t) + \left(\frac{1}{m} \int_t^{t+1} \left(F_{out_wheel} - \frac{1}{2} \rho_{air} A C_d v_{chas}^2(t) dt \right) \right) \quad (4)$$

where m is vehicle mass in kg, ρ_{air} is air density (1.23 kg/m^3), A is vehicle frontal area in m^2 , and C_d is the coefficient of drag.

The force out of the wheel block is calculated from the torque into the wheel block (τ_{in_wheel} , positive for propulsion), the friction braking torque ($\tau_{friction_brake}$, negative for braking), and the rolling resistance losses, as shown in (5):

$$F_{out_wheel} = \frac{\tau_{in_wheel} + \tau_{friction_brake}}{r_{wheel}} - (\mu_1 + \mu_2 v_{chas})mg \quad (5)$$

where r_{wheel} is the wheel radius in meters, μ_1 and μ_2 are rolling resistance coefficients, and g is gravitational acceleration (9.81 m/s^2). The torque into the wheel block is equal to the motor output torque (τ_{motor}) multiplied by the final drive ratio (r_{fd}) and the final drive efficiency (η_{fd}), as shown in (6):

$$\tau_{in_wheel} = \tau_{motor} r_{fd} \eta_{fd} \quad (6)$$

The motor speed in rad/s is calculated using (7):

$$\omega_{motor} = \frac{v_{chas} r_{fd}}{r_{wheel}} \quad (7)$$

The motor and inverter are modeled as a lumped 2-dimensional efficiency table, with inputs of motor speed and motor torque. The motor/inverter block calculates the DC input current required from the battery using (8):

$$I_{in_motor} = \frac{\omega_{motor} \tau_{motor} \times \eta_{motor}(\omega_{motor}, \tau_{motor})}{V_{batt}} \quad (8)$$

The total battery current (I_{batt}) is the sum of the required motor current (I_{in_motor}) and the required electrical accessory current, as shown in (9):

$$I_{batt} = I_{in_motor} + \frac{P_{accessory}}{V_{batt}} \quad (9)$$

The battery model uses the battery current and an initial state-of-charge (SOC) value to determine the SOC and battery terminal voltage at the next simulation step. The SOC is the integral of the battery current divided by the total battery capacity (C_{batt}) as shown in (10). The battery open circuit voltage (V_{batt_oc}) is determined from a look-up table using the current SOC value. The terminal voltage (V_{batt}) is calculated from V_{batt_oc} and the internal battery resistance (R_{batt}), as shown in (11).

$$SOC(t+1) = SOC(t) + \frac{1}{C_{batt}} \int_t^{t+1} -I_{batt} dt \quad (10)$$

$$V_{batt} = V_{batt_oc} - I_{batt} R_{batt} \quad (11)$$

This study focuses on transformer aging during the peak summer loads, and thus a 1.7 kW air conditioning load is added to the baseline $P_{accessory}$ load of 300W for a total accessory load of 2 kW, in order to better represent summer driving energy usage. A 6.6 kW charging rate is assumed for all vehicles unless otherwise stated, and the EV on-board charger efficiency η_{obc} is set to 95% to account for losses during the charging process. For each driver, the logged vehicle speed is fed into the Bolt EV Simulink model as a reference speed, so that the vehicle model “drives” the speed profile of each trip of the logged days. At the end of each trip, the simulated ending SOC of that trip is saved and then fed back into the model as

the starting SOC for the next trip on that day. For example, Fig. 2.4 shows the driving pattern of Driver #1 on the logged Tuesday, where the final SOC is determined by all trips in the day. This daily final SOC value indicates how much energy is needed from the grid to fully charge the battery by the departure time of the first trip on the next day.

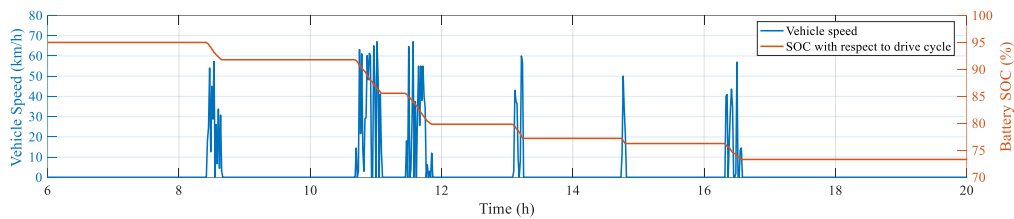


Fig. 2.4. Logged vehicle speed and simulated battery SOC for one example logged day.

The Bolt EV has a 60 kWh battery, yet the usable energy is somewhat less. This study approximates the usable energy as 90% of the total energy, meaning 54 kWh of energy is available between 5% and 95% SOC. For drivers who would need more than 54 kWh in a day, the vehicle energy use is saturated to 54 kWh per day. As indicated in Figs. 2.1 and 2.2, this battery size is capable of meeting the needs of drivers on 1017 out of 1050 logged days (96.9%). In order to quantify the extra charging needed for long-range EVs in this study, a similar analysis is also performed for short-range EVs similar to those used in previous smart-charging studies: 20 kWh battery \times 90% = 18 kWh usable energy, and only 62% of the logged driving days would have been completed with this smaller battery. This means that by considering only short-range EVs with a 20 kWh battery, 38% of the driving days would have erroneously low charging energy needs.

2.2.2 Grid Data

This study assumes a North American distribution grid with 10 houses per distribution transformer, and a maximum of one EV per house. Thus, 15 transformers are considered, meaning at 100% EV penetration, each of the 150 unique drivers is assigned to one house. For EV penetration rates less than 100%, EVs are assigned randomly within the group of 150 houses to mimic actual EV uptake within a neighborhood, from 0% to 100% EV penetration, in steps of 10%.

Fig. 2.5 shows the per house average residential load profiles for July and January without EV charging, as obtained from [31]. These profiles were generated based on detailed electricity consumption data from 200 houses in Florida, and averaged over the months of July and January, respectively. Thus, the July late afternoon peak is due to air conditioning, which is independent of people's home arrival times. Though individual homes will exhibit a noisier load profile with peaks and dips, it is assumed that when the loads from the 10 homes on the distribution circuit are summed together, many of these small peaks and dips will be cancelled out so that the sum can be approximately represented by the smooth average profile.

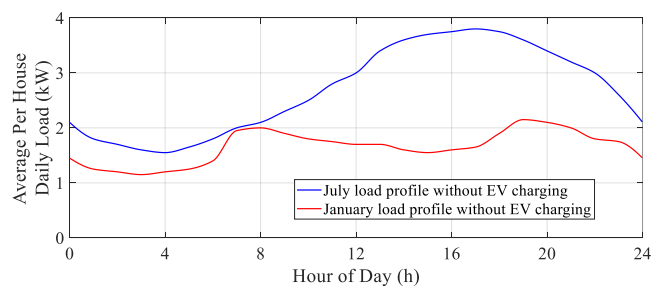


Fig. 2.5. Per house load profile without EV charging [31].

This study uses the July load profile as the worst-case scenario for EV charging stress on the distribution transformers.

Fig. 2.5 shows an average household load of 2.7 kW and a peak of 3.8 kW in July, and an average load of 1.6 kW and a peak of 2.2 kW in January. Two factors are considered while sizing transformers: (i) yearly aging factor [32], and (ii) maximum overloading [32]. The load cycle is very important for estimating the yearly aging factor. A daily variable load cycle consists of both variable loads and ambient temperatures. In the summer, high ambient temperatures and peak loads are expected during the day and reduced temperatures and loads are expected at night. The transformer modeling details in Section 2.2.4 show how an equivalent aging factor (F_{EQA}) is calculated for each load cycle. The F_{EQA} for summer is averaged with the F_{EQA} for winter to get yearly transformer aging. If the yearly $F_{EQA} = 1$, the transformer is considered correctly sized [32]. Transformer sizing must also limit short-term maximum overloading to 200% for power transformers and 300% for distribution transformers [32]. This study will mainly focus on the case of a correctly-sized transformer for a residential distribution grid that has not been oversized for potential future EV charging, as this is the case where new EV charging loads are of the most concern. A 25 kVA transformer is selected for each group of 10 homes, as this gives a summer F_{EQA} of 1.07, a winter F_{EQA} below one, and thus a yearly aging factor below one. With an assumed power factor of 0.98 [33], the peak summer load is 38.8 kVA or 155% loading, which is below the overloading limits. The analysis is then rerun for the case of a larger transformer,

37.5 kVA for 10 homes, to investigate the relative performance of each charging strategy when a transformer is oversized for the base residential load. Finally, the analysis is rerun for a 75kVA transformer servicing 30 homes, to investigate the relative performance of the charging strategies if the same ratio of homes to kVA rating is used, but with a larger transformer.

2.2.3 EV Charging Strategies

Until now, the term smart charging was typically used to describe a centralized or distributed method of controlling EV charging using significant infrastructure such as grid sensors, communication networks, central or local smart agents, connected and controllable EVSEs, and a measurement system to obtain vehicle SOC data. This chapter herein defines an alternative term, *Vehicle-Directed Smart Charging*, which describes methods that allow a standalone vehicle to more intelligently charge itself without requiring daily charging instructions from people or smart agents. Many current plug-in vehicles already provide drivers with some of these charging options. Table 2.2 summarizes the seven charging strategies analyzed in this study, including two *Vehicle-Directed Smart Charging* strategies already available in some vehicles, two proposed *Random-In-Window (RIW) Vehicle-Directed Smart Charging* strategies (with fixed or variable charging rates), and a centralized smart charging scheme representing the optimal case of flattening the transformer load from the literature [4],[6]. For all charging strategies, it is assumed that the battery will be fully charged by the driver-programmed departure

Table 2.2. Summary of Investigated EV Charging Methods

Category	Name	Status	Description
Uncontrolled Charging	Charge Right Away (CRA)	Default	Charging begins as soon as vehicle is plugged in.
	Time-of-Use (TOU)	Available in current vehicles	Driver sets charging start time, usually based on low electricity rates. This chapter investigates TOU start times of 7pm and 12am, meaning any vehicles plugged in at this time will start charging at 7pm or 12am, respectively.
Vehicle-Directed Smart Charging	Charge by Departure (CBD)	Available in current vehicles	Driver does one-time programming of daily departure times in vehicle. Vehicle starts charging when battery will be exactly fully charged by next day's first departure.
	Random (R)	From literature [26] – not implemented	Vehicle selects random charge start time between plug-in time and latest time that will give a full charge by next day's first departure.
	Random-In-Window Fixed Charge Rate (RIW-FR)	Proposed	Vehicle selects random charge start time within allowable window (details in text).
	Random-In-Window Variable Charge Rate (RIW-VR)	Proposed	Vehicle selects random charge start time within allowable window, then selects random charging rate (details in text).
Centralized	Centralized Smart Charging	From literature [4][6] - not widely implemented	Uses full smart-grid infrastructure to flatten the aggregate EV+ household load.

time of the following day – this is necessary for driver buy-in, and is how the two currently available *Vehicle-Directed Smart Charging* strategies operate.

Some prior work has considered randomness in smart-charging algorithms. Reference [23] proposes a centralized smart agent that monitors load congestion and grid voltage constraints in real-time, and when there is capacity to charge, EVs are selected randomly from the queue to charge. However, this strategy still requires the entire infrastructure needed for conventional centralized or distributed smart-charging systems. In [26], a centralized smart agent is recommended to assign random charging start times to EVs, meaning charging can occur during

times of peak household loads. Furthermore, this algorithm is only tested using normal distributions of arrival time with randomly assigned arrival SOC's, not real driving data. Reference [5] is the only chapter to the authors' knowledge to propose that the EV itself generate the random charging schedule rather than a connected smart agent. Yet [5] proposes that the EV generates random segments of charging time in 15 or 30 minute intervals, and that these charging intervals are randomly assigned anytime between plug-in time and departure time, as long as the vehicle calculates it will be fully charged by the departure time. This algorithm is unnecessarily complex, but more importantly, it did not show promising results in [5] because charging is still allowed to occur during times of peak household load early in the evening. For example, at 100% EV penetration, [5] shows a transformer lifetime of 1.36 years using its random charging strategy compared to over 100 years for a more optimal centralized smart-charging scheme.

This chapter proposes a simple but effective *Vehicle-Directed Smart Charging* concept, RIW, which automatically smooths out charging peaks by capitalizing on the inherent randomness already present within a group of EVs: a variety of next-day departure times and a variety of energy needs to be fully charged by the departure time. The proposed RIW strategy has two variants: fixed charging rate (FR) and variable charging rate (VR), which adds two additional calculation steps to the RIW-FR algorithm. The RIW algorithm first specifies a time window which defines the allowable charging start time. The window start-time (A) is constant and is set to be past the usual peak residential load. This window start-time

A could be hard-coded into the vehicle as 10 pm local time by the vehicle manufacturer, or allowed to be set to a constant value by the driver based on the local utility's recommended time for regions with different residential load profile peak times. The window end time B specifies the latest time that the vehicle can begin charging and still be fully charged by the first departure of the next day – thus the window end time B will change day-to-day, and will be equal to the charging start time of the CBD strategy described in Table 2.2. Upon plug-in, the vehicle knows time A and calculates time B to define the window. If the vehicle arrives home after time B , it must charge right away to get the most charge possible by the next day departure time, and thus smart charging cannot be applied in this case. If time B is earlier than time A (which is unusual based on the logged data), then the vehicle must start charging at time B in order to be fully charged by the next day departure. This case means the vehicle needs more time to charge than allowed by starting after time A , and includes scenarios such as: a highly depleted long-range EV, a lower charging rate, and/or a very early departure time the next morning. By far the most common scenario from the logged data is that time A is earlier than time B , creating a window where a random number generator (rand) randomly selects a charge start time C between times A and B . Since time A is after the peak household load times, the calculation of $\text{rand}(A,B)$ will select a charging start time after the peak household load, and the charge start time will be different for each vehicle running the algorithm, thus helping to smooth the charging load. This completes the calculations for RIW-FR, as all charging occurs at the fixed rate, 6.6

kW in this case. The RIW-FR algorithm is summarized in the blocks above the red dashed line in Fig. 2.6, and an example is shown in Fig. 2.7.

Two additional calculation steps are required for the second variant, RIW-VR, to also randomize the charging rate in addition to randomizing the charging start time. Let D represent the next day departure time. Thus, the minimum allowed charging rate E (in kW) for the already-selected charge start time C is:

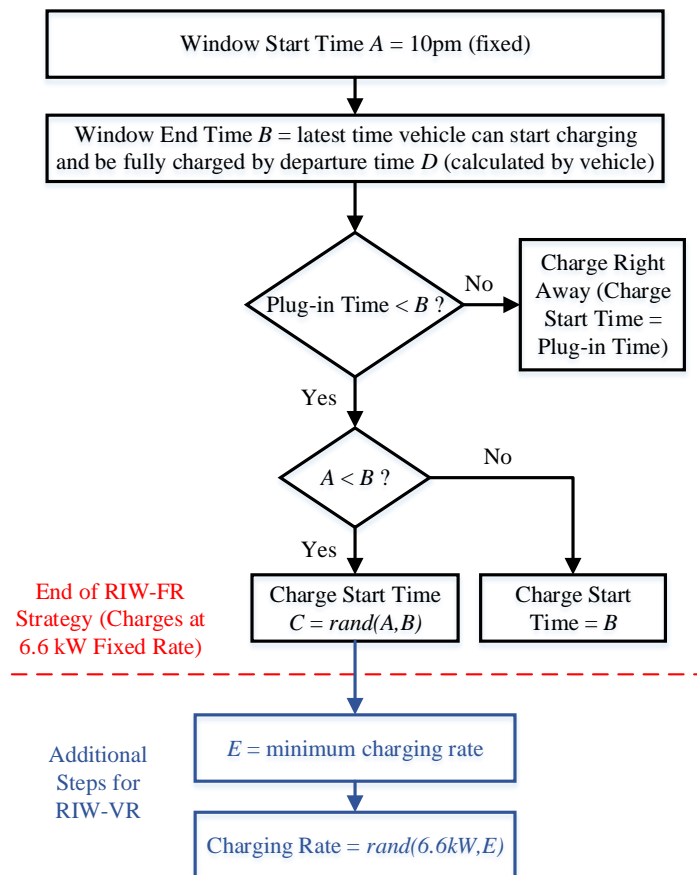


Fig. 2.6. Proposed RIW charging algorithm with RIW-FR and RIW-VR variants.

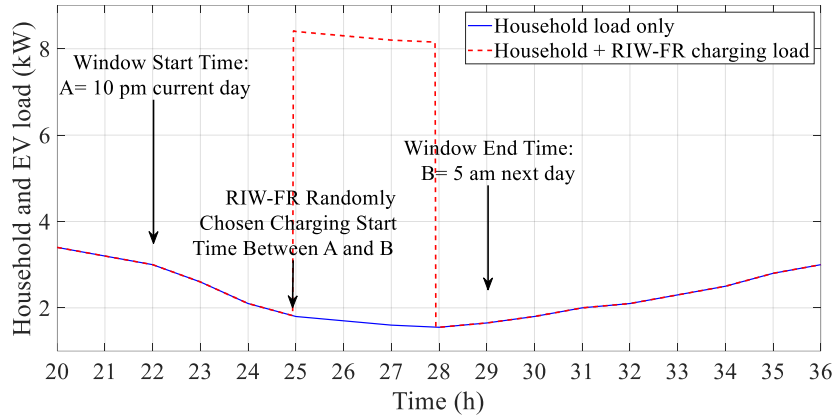


Fig. 2.7. Example of an RIW-FR charging algorithm for one driver on one day.

$$E = \frac{\text{Battery Energy Required}}{\eta_{obc} \times (\text{Maximum Charging Duration D-C})} \quad (11)$$

Lastly, the charging rate is selected randomly between the maximum rate (assumed as 6.6 kW in this case) and the minimum rate E as $rand(E, 6.6)$. These additional steps are shown in the lower portion of Fig. 2.6. The effect of the RIW-VR strategy is to lower the charge rate randomly and thus lengthen the charge duration compared to RIW-FR, while always adhering to the driver constraints of total battery energy required and next day departure time. The main difference between the proposed RIW strategies and a basic random strategy that can start charging anytime the vehicle is plugged in, is that in RIW, charging is automatically avoided during the peak household load times due to not allowing charging to start before time A, unless it is absolutely needed to fulfill the charging requirement by the next day's first departure (a rare scenario based on the logged data). This simple change makes a measurable difference in the associated distribution transformer aging, as will be shown in the next section.

The transformer load profiles generated by the RIW strategies are compared to the theoretically optimal transformer load profiles that could be generated by a centralized smart-charging scheme using full smart-grid infrastructure (smart agent, grid sensors, communication network, vehicle SOC and departure time data, and controllable EVSEs). This important comparison will indicate how close the proposed infrastructure-less *Vehicle-Directed Smart Charging* strategies can come to the optimal performance of a centralized smart-charging strategy. Reference [4] compared a complex genetic algorithm-based smart-charging strategy, which minimized transformer aging, to a strategy that flattened the transformer load (i.e., filled the valley of the overnight household load), and found virtually identical transformer aging results. Follow-up work in [6] further validated that flattening the total EV plus household load leads to minimization of transformer aging. Though previous research has focused on precisely how to flatten this load in real-time, including how to predict the overnight household load [4], the optimal end result is the same: flattening the transformer load as much as possible given the EV energy charging requirements. Thus, this chapter assumes the optimal case for the centralized smart-charging strategy: the charging start time and charging rate can be varied to precisely flatten the total transformer load. All future household loads are assumed precisely known so that no prediction is required. This creates an idealized version of a centralized smart-charging strategy to compare to the *Vehicle-Directed Smart Charging* strategies.

2.2.4 Transformer Aging Model

The primary concern in overloading distribution transformers with residential and EV charging loads is accelerated transformer aging, and thus the equivalent aging factor, F_{EQA} , is a useful metric for comparing EV charging strategies. Transformer aging specifically refers to deterioration of the insulation, which is dependent on temperature, moisture, and oxygen content. In modern oil-cooled transformers, the effect of moisture and oxygen content on insulation deterioration is negligible, and thus, the hottest-spot insulation temperature is the primary factor of accelerated aging [32]. The overhead distribution transformer aging model from IEEE C57.91-2011 provides a formulation of the hottest-spot insulation temperature through a series of non-linear equations, which contain a combination of modeled equations and parameters based on empirical test data. Based on the temperature, this document develops a transformer insulation life curve relating transformer insulation life to winding hottest-spot temperature that is equally valid for power and distribution transformers using the same type of

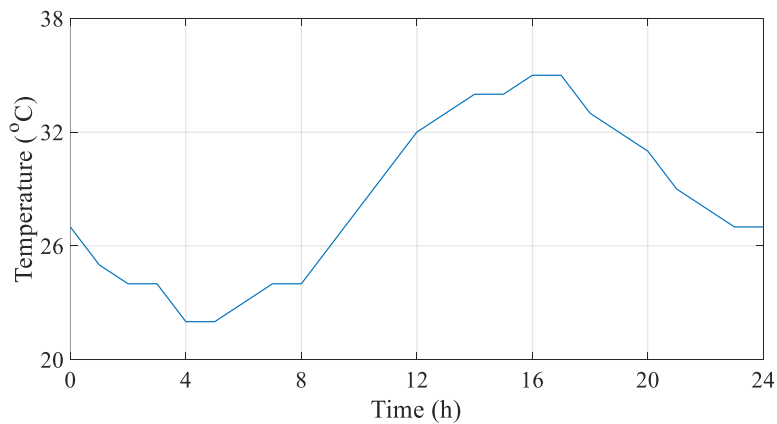


Fig. 2.8. Daily ambient temperature profile used for transformer aging model (from Toronto, Canada in July [37]).

insulation. It also demonstrates transformer life cycle calculation based on transformer loading test data. Thus, a computer program developed based on the transformer aging calculation guide [32] can provide a reasonable prediction of the transformer insulation aging rate and remaining life of the insulation. The overhead distribution transformer aging model used in this chapter from [32] is briefly described below. Full details can be accessed from [32]. Ambient temperature profiles for one week in July in Toronto, Canada were obtained from [34] for use in the model, as shown in Fig. 2.8.

The total household and EV charging load profile for each EV charging strategy is converted to an equivalent load, L_{equiv} , using (12):

$$L_{equiv} = \sqrt{\frac{L_1^2 \Delta t_1 + L_2^2 \Delta t_2 + \dots + L_n^2 \Delta t_n}{\Delta t_1 + \Delta t_2 + \dots + \Delta t_n}} \quad (12)$$

where L_1, L_2, \dots, L_n are the kVA values of household plus EV charging loads in the time intervals $\Delta t_1, \Delta t_2, \dots, \Delta t_n$. In this study, these time intervals are set to 1 minute so that high resolution charging patterns are used in the thermal analysis.

The hottest-spot temperature, θ_H , in a transformer winding is directly related to the insulation life of a transformer, and the loading of a transformer is restricted by θ_H . With temperature and time, the cellulose insulation experiences a depolymerization process [35]. In this process, the average molecular weight of the cellulose decreases, which results in shorter cellulose chains, and degraded tensile strength and elasticity of the insulation paper. In the long run, the insulation paper

becomes weak and cannot withstand regular short circuit forces and vibrations that are part of transformer operation. This process is termed “transformer aging” [35]. As the rise of temperature in the winding is mostly dependent on loading, and load management algorithms such as vehicle smart charging strategies help redistribute the loads to minimize overloading, load management algorithms can reduce θ_H and thus reduce aging. θ_H is the summation of three temperature components in °C [32] as shown in (13): ambient temperature, θ_A , delta between the top-oil temperature and the ambient, $\Delta\theta_{TO}$, and the delta between the hottest-spot temperature and the top-oil temperature, $\Delta\theta_H$.

$$\theta_H = \theta_A + \Delta\theta_{TO} + \Delta\theta_H \quad (13)$$

$\Delta\theta_{TO}$ and $\Delta\theta_H$ are dependent on the equivalent loads in each time interval, L_{equiv} and other variables as described in [32]. The equation of aging acceleration factor, F_{AA} , is an exponential function of the hottest-spot temperature θ_H as shown in (14).

$$F_{AA} = e^{\left(\frac{B}{383} - \frac{B}{\theta_H + 273}\right)} \quad (14)$$

In (14), B is the cellulose aging rate constant, with a value of 15000 obtained from the transformer insulation life curve in [32]. Transformer specification data are obtained from [36]. The equivalent aging factor, F_{EOA} , is a useful result as it represents how much faster than normal a transformer ages based on its thermal profiles. For example, $F_{EOA} = 1$ means the transformer aged 1 week over the test

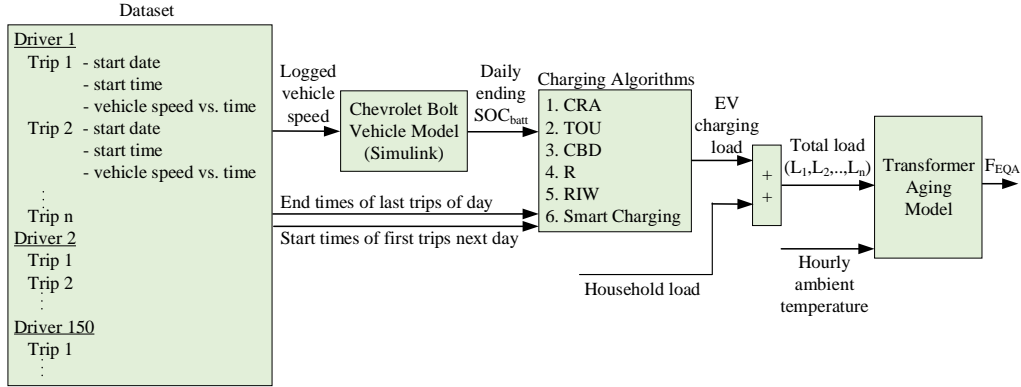


Fig. 2.9. Simulation process summary.

week period, and $F_{EQA} = 2$ means the transformer aged at double the normal rate, or 2 weeks over the test week period. F_{EQA} is described by (15), where Δt_n is each time interval, N is the total number of time intervals, and F_{AA_n} is the aging acceleration factor during the time interval, Δt_n .

$$F_{EQA} = \frac{\sum_{n=1}^N F_{AA_n} \Delta t_n}{\sum_{n=1}^N \Delta t_n} \quad (15)$$

2.2.5 Simulation Process

Fig. 2.9 summarizes the simulation process. The transformer aging model block calculates aging for each of the 15 transformers, and then averages these values to get one representative summer F_{EQA} value to use in comparing the various EV charging methods. The process is repeated for all EV penetration rates from 0% to 100%, in steps of 10%.

2.3. Results And Discussion

2.3.1 Charging Profiles

To investigate the importance of considering the effects of long-range EVs on the grid, the total household plus EV charging loads are compared for the simulated cases of long-range EVs (60kWh battery) and short range EVs (20kWh batteries) for the logged 150 drivers at 100% EV penetration (one EV per house). Figs. 2.10 to 2.15 show the results for the logged Monday for each of the charging strategies discussed in Table 2.2. This real-world data is crucial to show how often drivers make use of the longer range of 60 kWh battery EVs, as Figs. 2.1 and 2.2 show that only 62% of driving days will be satisfied with the 20 kWh battery EV. Since the daily simulated energy use is saturated to a much lower level for the short range EV, Figs. 2.10 to 2.15 show that less charging energy is needed from the grid for the 150 short-range EVs (1.77 MWh) compared to the 150 long range EVs (2.31 MWh). The difference is 541 kWh, or a 30.5% increase for long-range EVs. Table 2.3 shows charging energy difference between long- and short-range EVs on each day of the logged week. As expected, more long-range driving occurs on Friday, Saturday, and Sunday. The average increase in energy usage based on long-range EVs compared to short-range EVs is 35%.

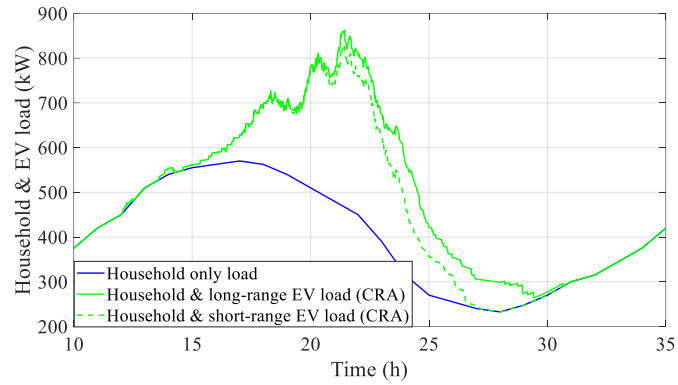


Fig. 2.10. Long-range EV and short-range EV simulated Monday load for 150 logged drivers (CRA charging strategy).

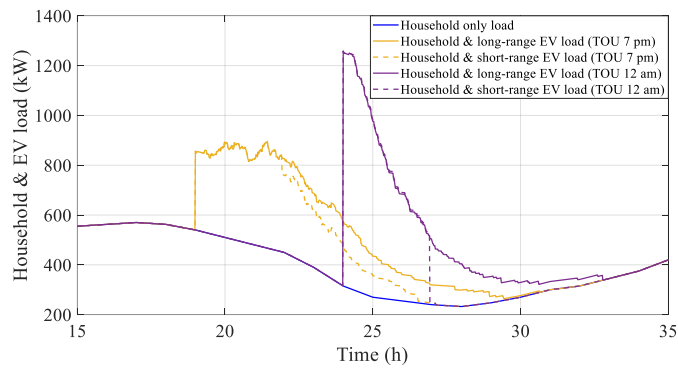


Fig. 2.11. Long-range EV and short-range EV simulated Monday load for 150 logged drivers (TOU 7pm & 12am charging strategy).

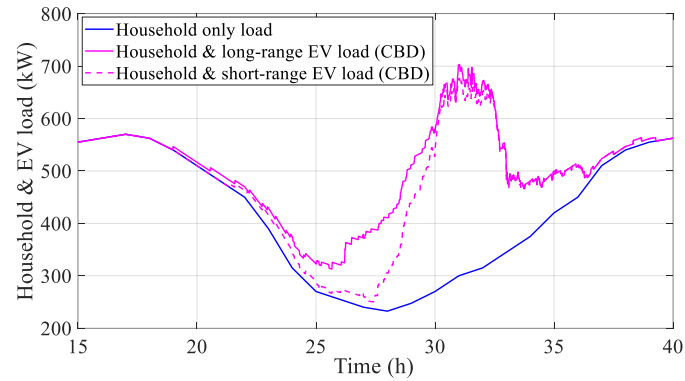


Fig. 2.12. Long-range EV and short-range EV simulated Monday load for 150 logged drivers (CBD charging strategy).

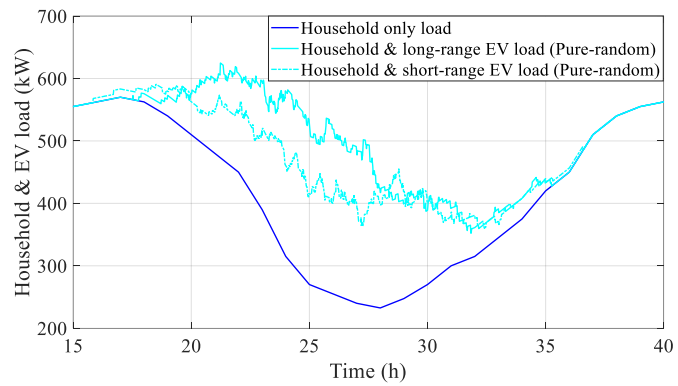


Fig. 2.13. Long-range EV and short-range EV simulated Monday load for 150 logged drivers (Random charging strategy from [26]).

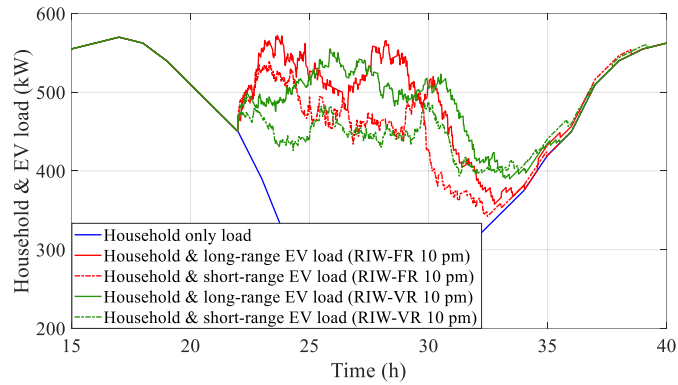


Fig. 2.14. Long-range EV and short-range EV simulated Monday load for 150 logged drivers (RIW-FR and RIW-VR charging strategies).

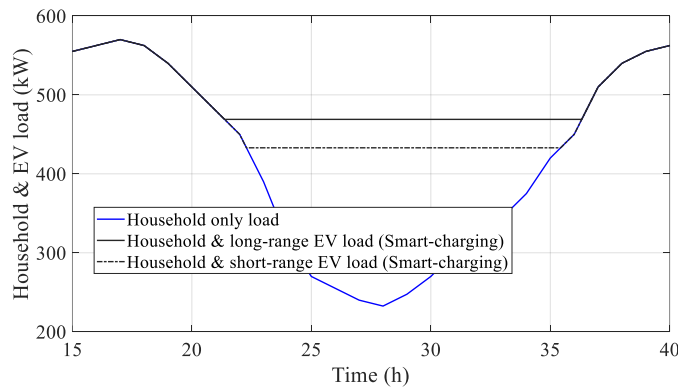


Fig. 2.15. Long-range EV and short-range EV simulated Monday load for 150 logged drivers (Idealized centralized smart-charging strategy [4],[6]).

Table 2.3. Comparison of Charging Energy Demand For Long- And Short-Range EVs For 150 Drivers

Day of Week	Short-Range EV Charging Energy (MWh)	Long-Range EV Charging Energy (MWh)	Increase in Charging Energy Required For Long-Range EVs (%)
Monday	1.77	2.31	30.5
Tuesday	1.85	2.52	36.2
Wednesday	1.83	2.43	32.8
Thursday	1.69	2.18	29.0
Friday	1.86	2.62	40.9
Saturday	1.80	2.43	35.0
Sunday	1.53	2.16	41.2

Figs. 2.16 and 2.17 compare all charging strategies for short-range EVs and long-range EVs, respectively, for all 15 transformers (150 houses) at 100% EV penetration (150 EVs) for the logged Monday evening. Both the figures show that CRA and TOU charging strategies create the highest loading peaks. This is unfortunate because TOU charging is a common way for EV drivers to reduce their charging costs. However, if many EV drivers choose the same starting times, undesired aggregate peaks will be formed. The TOU 12am peak is higher than the TOU 7pm peak (even though the household load is lower at 12am) because all or nearly all of the vehicles have arrived home by this time, and they all start charging at once. At 7pm, many vehicles are not home yet (as per Fig. 2.1), so the surge of charging power is lower. Of the charging strategies currently available in vehicles (CRA, TOU, and CBD), the CBD strategy creates the lowest charging peak. The strategies from the literature (random and centralized smart-charging), and the proposed RIW (both variants) produce charging peaks lower than CBD, and will be analyzed in detail with respect to transformer aging. To illustrate the unique loading profiles on each of the 15 transformers, Fig. 2.18 shows the detailed charging load on one of the transformers for 100% EV penetration on the logged Monday for long-range EVs.

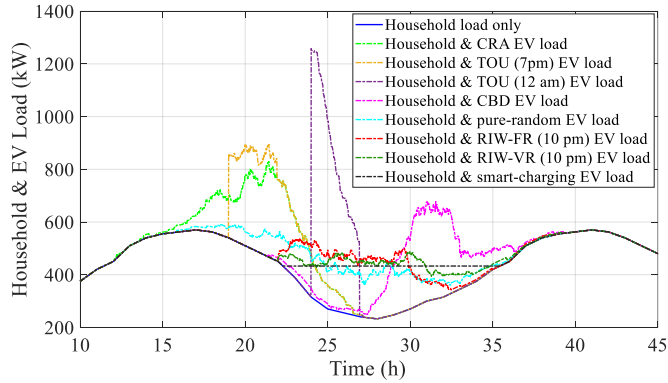


Fig. 2.16. Comparison of all charging strategies for 150 EV drivers on logged Monday evening for short-range EVs.

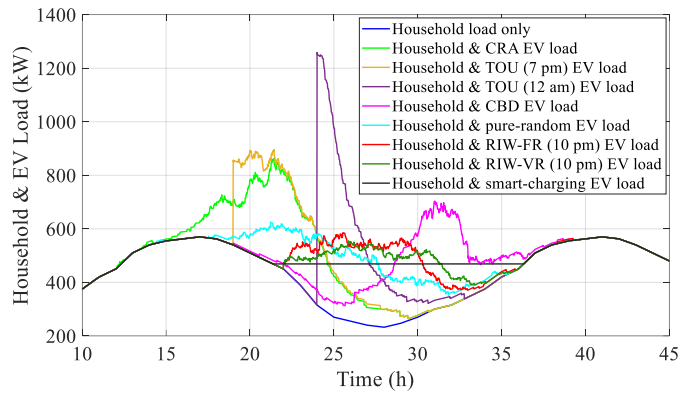


Fig. 2.17. Comparison of all charging strategies for 150 EV drivers on logged Monday evening for long-range EVs.

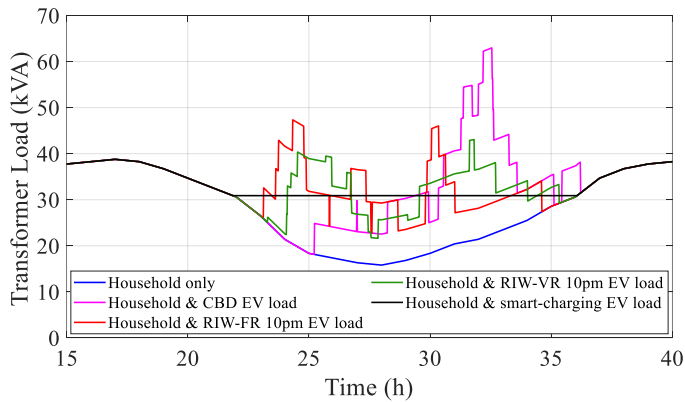


Fig. 2.18. Detailed charging load on Transformer 1 for logged Monday evening (long-range EV).

2.3.2 Average Aging of 25 kVA Transformers

The weekly loading profiles for the 15 transformers are used to calculate transformer equivalent aging factors, F_{EQA} , for each 25 kVA transformer. These 15 values are then averaged to get a single F_{EQA} value which represents the average transformer aging factor in the distribution system for a given EV penetration rate. Firstly, the pure random charging strategy [26] is compared to the proposed RIW strategies with different window start times, A . For the RIW-FR strategy, the results are shown in Fig. 2.19 for short-range EVs and in Fig. 2.20 for long-range EVs. For the RIW-VR strategy, the results are shown in Fig. 2.21 and Fig. 2.22 for short-range and long-range EVs, respectively. Since the pure random strategy allows EV charging during times of household peak load, it results in the highest equivalent aging factor for most EV penetration rates. When the RIW window start time is earlier (7pm to 9pm), there is still some overlap between EV charging and peak household load. For both variants, RIW with a window start time of 10pm provides the best balance between pushing the EV charging load later in the evening, yet still leaving enough time for the vehicles to charge overnight without creating high overnight loading peaks (which occur for window start times of 11pm and later). Thus, 10pm local time is proposed as the optimal RIW window start time for the given household load profile and logged driver dataset, and thus 10pm will be used as the window start time for both RIW-FR and RIW-VR strategies for the remainder of the analysis.

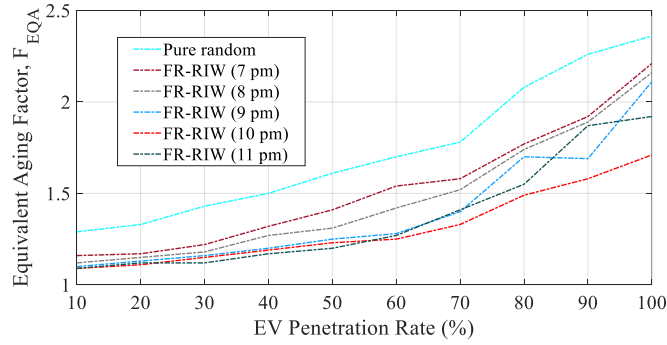


Fig. 2.19. Average weekly equivalent aging factors for random charging and RIW-FR with different window start times (A) for short-range EVs.

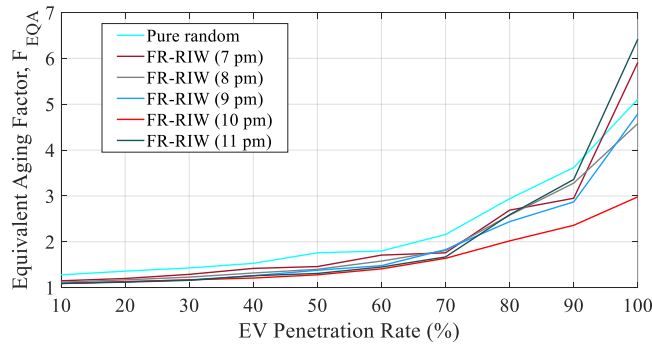


Fig. 2.20. Average weekly equivalent aging factors for random charging and RIW-FR with different window start times (A) for long-range EVs.

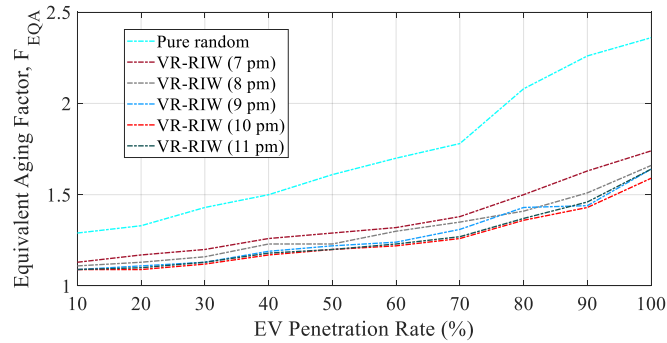


Fig. 2.21. Average weekly equivalent aging factors for random charging and RIW-VR with different window start times (A) for short-range EVs.

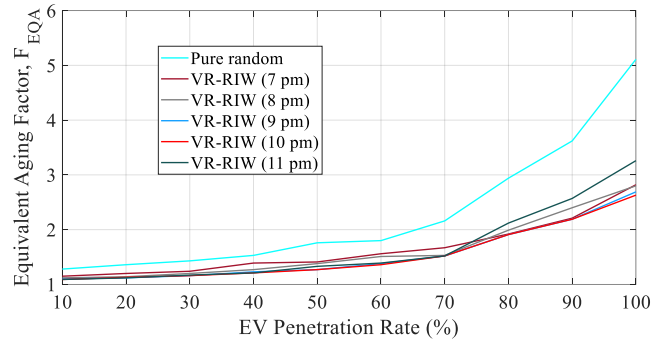


Fig. 2.22. Average weekly equivalent aging factors for random charging and RIW-VR with different window start times (A) for long-range EVs.

Fig. 2.23 shows the F_{EQA} for all charging strategies for both short-range and long-range EVs. As expected based on the charging profiles, CRA and TOU produce the highest F_{EQA} , with unfeasibly high values at high EV penetration rates. Fig. 2.24 shows a zoomed-in version of Fig. 2.23 to more clearly illustrate the equivalent aging factors at low EV penetration rates. For no EV charging (0% penetration), $F_{EQA} = 1.07$, which is as expected for a transformer that has been suitably sized for the household load. At most EV penetration rates, CRA and TOU 7pm create unsustainably high aging rates, yet the TOU 12am strategy limits aging to 2 times the normal rate up to 60% EV penetration. This occurs despite the high charging peaks because these peaks occur during the cooler overnight hours, which lessens transformer aging. However, when the EV penetration rate of the neighborhood rises to 100%, TOU 12am is worse than CRA since the EV charging peaks get very high.

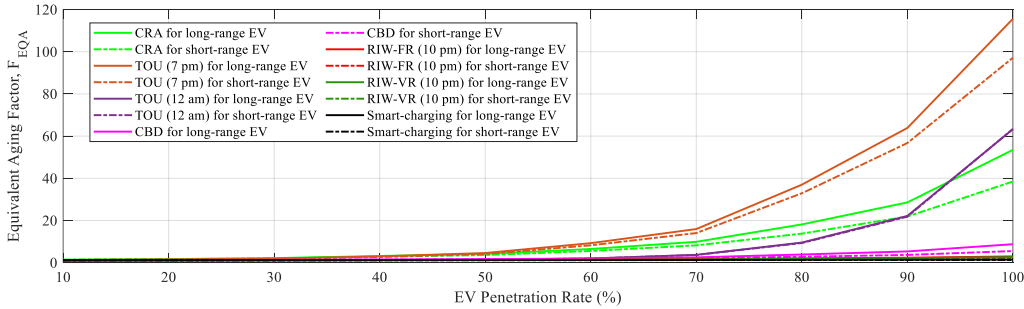


Fig. 2.23. Weekly average transformer aging factors for different charging strategies across all EV penetration rates.

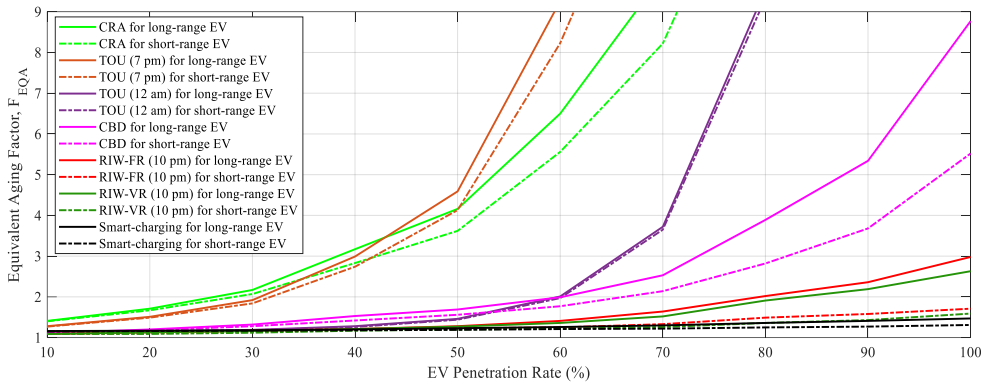


Fig. 2.24. Weekly average transformer aging factors for different charging strategies across all EV penetration rates (zoomed in).

The CBD, RIW, and centralized smart-charging strategies are the superior charging options across all EV penetration rates. For each of these strategies, Fig. 2.24 shows that there is a significant increase in transformer aging for long-range EVs compared to short-range EVs – for example, the RIW-FR F_{EQA} and RIW-VR F_{EQA} for long-range EVs at 100% EV penetration are 3 and 2.6 respectively, compared to RIW-FR $F_{EQA} = 1.7$ and RIW-VR $F_{EQA} = 1.6$ for short-range EVs, an increase in aging of 176% and 163% respectively. Since CBD is the only charging method of these three commonly available to EV drivers today, it is recommended

that EV drivers utilize this charging method until a superior charging method becomes available. However, at higher EV penetration rates, which can easily occur in neighborhood clusters, the CBD strategy is not ideal due to the larger EV charging peak that occurs in the early morning. At 100% EV penetration, the F_{EQA} for CBD reaches 8.8 for long-range EVs, which would reduce the life of a 30-year rated transformer to 3.4 years. Thus, superior charging methods are clearly required. Conversely, the RIW-FR and RIW-VR strategies produce $F_{EQA} = 3$ and $F_{EQA} = 2.6$ respectively for long range EVs at 100% EV penetration, while pure random charging produces $F_{EQA} = 5.1$ for long range EVs at 100% EV penetration.

Figs. 2.19 to 2.24 show that the proposed variants of RIW strategy produce the lowest transformer aging of all *Vehicle-Directed Smart Charging* strategies, for both long range and short range EVs, and across all EV penetration rates. Furthermore, for long-range EVs, the RIW-FR strategy produces similar transformer aging as the ideal centralized smart-charging strategy up to 50% EV penetration ($F_{EQA} = 1.28$ and $F_{EQA} = 1.23$, respectively). For RIW-VR, the aging progression is similar to centralized smart-charging strategy for up to 60% EV penetration ($F_{EQA} = 1.36$ and $F_{EQA} = 1.26$, respectively). For short-range EVs, the RIW-FR strategy produces similar transformer aging as the smart-charging strategy up to 60% EV penetration ($F_{EQA} = 1.25$ and $F_{EQA} = 1.21$, respectively). For short range RIW-VR, the aging progression is similar to centralized smart-charging strategy for up to 70% EV penetration ($F_{EQA} = 1.26$ and $F_{EQA} = 1.22$, respectively). This is a very important conclusion, as the variants of RIW strategy, which require

no smart-charging infrastructure, performs approximately the same as the centralized smart-charging strategy up to EV penetration rates of 60% for long-range EVs and up to 70% for short-range EVs. Whereas a controlled smart-charging strategy requires significant investment in grid sensors, communication networks, distributed or centralized smart agents, connected and controllable EVSEs, and a method to obtain vehicle SOC data, the proposed variants of RIW algorithm can easily be added to vehicle software by automotive manufacturers, either in new EVs, or by over-the-air software updates to already-purchased EVs. The on-board computation requirement is very low, as just one to three additional calculations are required compared to the already-implemented CBD strategy (which is the calculation of the random charge start time between times A and B for RIW-FR and two additional calculations for minimum charging rate bound and then random charge rate determination for RIW-VR). As variants of RIW are *Vehicle-Directed Smart Charging* strategies, the driver's EVSE and local grid need no updates to implement this strategy. Overall, the proposed RIW-FR and RIW-VR charging strategies are simple and low-cost methods that can be used in the near future to limit transformer aging to that expected from a full smart-charging system at moderate EV penetration rates.

2.3.3 Average Aging of 37.5 kVA Transformers

The preceding analysis is repeated for long-range EVs plugging into a distribution network using larger transformers with 37.5 kVA nameplate ratings for the same 10-home groupings per transformer. This scenario represents the case of

newer neighborhoods where the potential of future EV charging has been taken into account for transformer sizing. Fig. 2.25 shows the average equivalent aging factors for the 37.5 kVA transformers. As expected, the F_{EQA} rates are lower compared to the 25 kVA scenario. However, the pattern of accelerated aging is similar to that of the 25 kVA transformer across the charging strategies: CRA and TOU strategies produce by far the highest aging rates. RIW variants produce the lowest aging rate of the *Vehicle-Directed Smart Charging* strategies. RIW-FR produces similar aging to the ideal centralized smart-charging strategy up to EV penetration rates of 60% ($F_{EQA} = 0.67$ and $F_{EQA} = 0.63$, respectively). RIW-VR produces similar aging to the centralized smart-charging strategy up to EV penetration rates of 70% ($F_{EQA} = 0.70$ and $F_{EQA} = 0.65$, respectively). Notably, the RIW strategies limit F_{EQA} to 1 even at 100% EV penetration, whereas all other *Vehicle-Directed Smart Charging* strategies produce $F_{EQA} > 1$ for 100% EV penetration (ranging from 1.54 to 6.9).

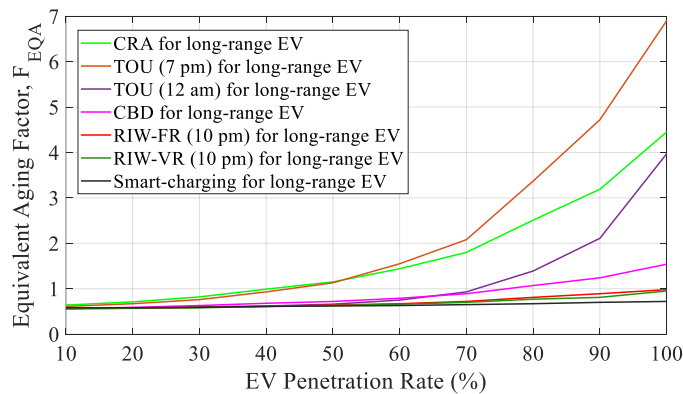


Fig. 2.25. Weekly average transformer aging factors for different charging strategies with 37.5 kVA transformer.

2.3.4 Average Aging of 75 kVA Transformers

For this analysis, the ratio of homes to transformer kVA is kept the same as the original 25 kVA transformer analysis. The purpose is to investigate if the relationships between the charging strategies still hold when larger transformers are used. Thus, in this section, 30 homes are assigned to each 75 kVA transformer, meaning the transformer is precisely sized for the homes and is not oversized for any future EV charging (the most concerning real-world case). Fig. 2.26 and Fig. 2.27 (zoomed in version of Fig. 2.26) show that the transformer aging follows a similar pattern to that of a rightly-sized 25 kVA or an oversized 37.5 kVA transformer. CRA, TOU-7pm, and TOU-12am produce the highest transformer aging rates, whereas CBD produces $F_{EQA} = 6.8$ at 100% penetration. RIW-FR and RIW-VR both produce similar transformer aging rates as the ideal centralized smart-charging method up to 60% EV penetration ($F_{EQA} = 1.77$ for both RIW variants and $F_{EQA} = 1.71$ for smart charging). Therefore, the proposed RIW strategies can be used to reduce aging in transformers of various sizes and with various base loading scenarios. Overall, the RIW strategies are simple and low-cost solutions that can be implemented without immediate distribution network upgrades and complex smart charging infrastructure installation.

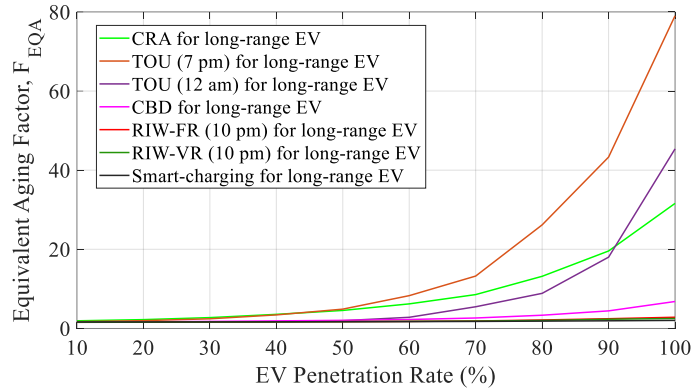


Fig. 2.26. Weekly average transformer aging factors for different charging strategies with 75 kVA transformer.

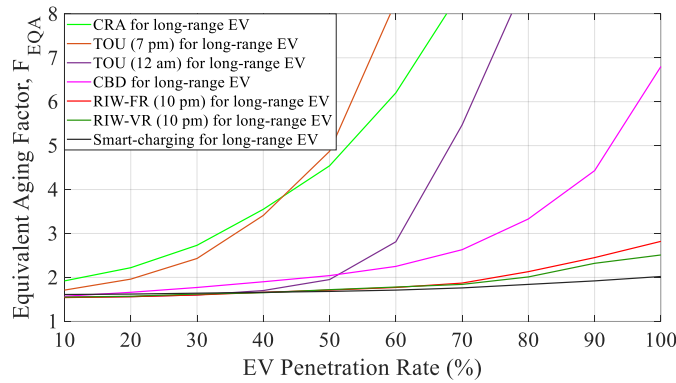


Fig. 2.27. Weekly average transformer aging factors for different charging strategies with 75 kVA transformer (zoomed-in).

2.4. Conclusions

With the introduction of reasonably-priced long-range EVs, it is crucial to investigate and mitigate the effects of the increasing adoption of these vehicles on distribution transformers. While there has been much focus on centralized and distributed smart-charging strategies, these strategies require significant infrastructure, and thus will take time and investment to be implemented. This

chapter defines *Vehicle-Directed Smart Charging* as strategies that can be implemented by a suitably-programmed EV without the need for additional infrastructure. This chapter proposes and investigates a new *Vehicle-Directed Smart Charging* concept, Random-In-Window (RIW), which has two variants: fixed rate charging (RIW-FR) and variable rate charging (RIW-VR). With two additional calculation steps, the RIW-VR is shown to be the slightly superior strategy of the two, and is shown to produce a similar transformer aging rate as a centralized smart-charging algorithm over a summer week for EV penetration rates up to 60% for long-range EVs and up to 70% for short-range EVs. Investigations of larger transformers found the same correlations. This study used an extensive logged driving dataset of 150 unique drivers over one week and short-range (20kWh battery) and long-range (60kWh battery) EV models to support the analysis. Based on the driving habits of the logged drivers in this study, it was also found that long-range EVs consume approximately 30% more charging energy than short-range EVs, and thus should be explicitly considered in future EV charging studies. It is recommended that EV manufacturers consider adding the RIW charging strategy to their on-board software, as it requires only one to three simple additional calculations compared to the already commonly implemented CBD strategy, yet it performs significantly better than the CBD strategy, especially at higher EV penetration rates.

Chapter 2 References

- [1] W.-J. Guan, X.-Y. Zheng, K. F. Chung, and N.-S. Zhong, “Impact of air pollution on the burden of chronic respiratory diseases in China: time for urgent action,” *The Lancet*, vol. 388, no. 10054, pp. 1939–1951, 2016.
- [2] Online: <https://www.chevrolet.com/electric/bolt-ev-electric-car> [Accessed May 2019]
- [3] Online: <https://www.tesla.com/model3> [Accessed May 2019]
- [4] Q. Gong, S. Midlam-Mohler, V. Marano, and G. Rizzoni, “Distribution of PEV charging resources to balance transformer life and customer satisfaction,” *Proceedings of the 2012 IEEE International Electric Vehicle Conference*, Greenville, SC, USA, 2012.
- [5] Q. Gong, S. Midlam-Mohler, V. Marano, and G. Rizzoni, “Study of PEV charging on residential distribution transformer life,” *IEEE Trans. on Smart Grid*, vol. 3, no. 1, pp. 404-412, March 2012.
- [6] Q. Gong, S. Midlam-Mohler, E. Serra, V. Marano, and G. Rizzoni, “PEV charging control considering transformer life and experimental validation of a 25 kVA distribution transformer,” *IEEE Trans. on Smart Grid*, vol. 6, no. 2, pp. 648-656, March 2015.
- [7] J. Quirós-Tortós, L. Ochoa, S. Alnaser, and T. Butler, “Control of EV charging points for thermal and voltage management of LV networks,” *IEEE Trans. on Power Systems*, vol. 31, no. 4, pp. 3028-3039, July 2016.
- [8] M. Gray and W. Morsi, “Power quality assessment in distribution systems embedded with plug-in hybrid and battery electric vehicles,” *IEEE Trans. on Power Systems*, vol. 30, no. 2, pp. 663-671, March 2015.
- [9] M. ElNozahy and M. Salama, “A comprehensive study of the impacts of PHEVs on residential distribution networks,” *IEEE Trans. on Sustainable Energy*, vol. 5, no. 1, pp. 332-342, Jan. 2014.
- [10] V. del Razo, C. Goebel, and H. Jacobsen, “Vehicle-originating-signals for real-time charging control of electric vehicle fleets,” *IEEE Trans. on Transportation Electrification*, vol. 1, no. 2, pp.150-167, Aug. 2015.
- [11] R. Abousleiman and R. Scholer, “Smart charging: system design and implementation for interaction between plug-in electric vehicles and the power grid,” *IEEE Trans. on Transportation Electrification*, vol. 1, no. 1, pp.18-25, June 2015.
- [12] J. Hu, S. You, M. Lind, and J. Østergaard, “Coordinated charging of electric vehicles for congestion prevention in the distribution grid,” *IEEE Trans. on Smart Grid*, vol. 5, no. 2, pp. 703-711, March 2014.
- [13] E. Veldman and R. Verzijlbergh, “Distribution grid impacts of smart electric vehicle charging from different perspectives,” *IEEE Trans. on Smart Grid*, vol. 6, no. 1, pp. 333-342, Jan. 2015.
- [14] N. Mehboob, M. Restrepo, C. Canizares, C. Rosenberg, and M. Kazerani, “Smart operation of electric vehicles with four-quadrant chargers considering uncertainties,” *IEEE Trans. on Smart Grids*, Early Access Article, 2018.

- [15] B. Sun, Z. Huang, X. Tan, and D. Tsang, "Optimal scheduling for electric vehicle charging with discrete charging levels in distribution grid," *IEEE Trans. on Smart Grid*, vol. 9, no. 2, pp. 624-634, March 2018.
- [16] R. Mehta, D. Srinivasan, A. Khambadkone, J. Yan, and A. Trivedi, "Smart charging strategies for optimal integration of plug-in electric vehicles within existing distribution system infrastructure," *IEEE Trans. on Smart Grid*, vol. 9, no. 1, pp. 299-312, Jan. 2018.
- [17] O. Beaude, S. Lasaulce, M. Hennebel, and I. Mohnd-Kaci, "Reducing the impact of EV charging operations on the distribution network," *IEEE Trans. on Smart Grid*, vol. 7, no. 6, pp. 2666-2679, Nov. 2016.
- [18] A. Hilshey, P. Hines, P. Rezaei, and J. Dowds, "Estimating the impact of electric vehicle smart charging on distribution transformer aging," *IEEE Trans. on Smart Grid*, vol. 4, no. 2, pp. 905-913, June 2013.
- [19] O. Ardakanian, S. Keshav, and C. Rosenberg, "Real-time distributed control for smart electric vehicle chargers: from a static to a dynamic study," *IEEE Trans. on Smart Grid*, vol. 5, no. 5, pp. 2295-2305, Sept. 2014.
- [20] S. Weckx, R. D'Hulst, B. Claessens, and J. Driesen, "Multiagent charging of electric vehicles respecting distribution transformer loading and voltage limits," *IEEE Trans. on Smart Grid*, vol. 5, no. 6, pp. 2857-2867, Nov. 2014.
- [21] L. Zhang, V. Kekatos, and G. Giannakis, "Scalable electric charging protocols," *IEEE Trans. on Power Systems*, vol. 32, no. 2, pp. 1451-1462, March 2017.
- [22] A. Bin Humayd and K. Bhattacharya, "A novel framework for evaluating Maximum PEV penetration into distribution systems," *IEEE Trans. on Smart Grid*, vol. 9, no. 4, pp. 2741-2751, July 2018.
- [23] K. Zhou and L. Cai, "Randomized PHEV Charging Under Distribution Grid Constraints," *IEEE Trans. on Smart Grid*, vol. 5, no. 2, pp. 879-887, March 2014.
- [24] R. Verzijlbergh, M. Grond, Z. Lukszo, J. Slootweg, and M. Ilić, "Network impacts and cost savings of controlled EV charging," *IEEE Trans. on Smart Grid*, vol. 3, no. 3, pp. 1203-1212, Sept. 2012.
- [25] L. Hua, J. Wang, and C. Zhou, "Adaptive electric vehicle charging coordination on distribution network," *IEEE Trans. on Smart Grid*, vol. 5, no. 6, pp. 2666-2675, Nov. 2014.
- [26] L. Fernández, T. Román, R. Cossent, C. Domingo, and P. Frías, "Assessment of the impact of plug-in electric vehicles on distribution networks," *IEEE Trans. on Power Systems*, vol. 26, no. 1, pp. 206-213, Feb. 2011.
- [27] R. Leou, C.-L. Su, and C.-N. Lu, "Stochastic analyses of electric vehicle charging impacts on distribution network," *IEEE Trans. on Power Systems*, vol. 29, no. 3, pp. 1055-1063, May 2014.
- [28] Q. Gong, S. Midlam-Mohler, V. Marano, and G. Rizzoni, "Virtual PHEV fleet study based on Monte Carlo simulation," *Int. Journal of Vehicle Design*, vol. 58, pp. 266-290, 2012.

- [29] S. Shahidinejad, S. Filizadeh, and E. Bibeau, “Profile of charging load on the grid due to plug-in vehicles,” *IEEE Trans. on Smart Grid*, vol. 3, no. 1, pp. 135–141, Mar. 2012.
- [30] P. Palcu and J. Bauman, “Whole-day driving prediction control strategy: analysis on real-world drive cycles,” *IEEE Trans. on Transportation Electrification*, vol. 4, no. 1, pp. 172-183, March 2018.
- [31] D. Parker, “Research highlights from a large scale residential monitoring study in a hot climate,” *Proceeding of International Symposium on Highly Efficient Use of Energy and Reduction of its Environmental Impact*, pp. 108-116, Japan Society for the Promotion of Science Research for the Future Program, JPS-RFTF97P01002, Osaka, Japan, Jan. 2002. Available online: <http://www.fsec.ucf.edu/en/publications/html/FSEC-PF-369-02/>
- [32] *Transformers Committee of the IEEE Power Engineering Society*, “IEEE guide for loading mineral-oil-immersed transformers and step-voltage regulators,” IEEE Std C57.91-2011, 2011.
- [33] Whitby Hydro Energy Services Corp., “Power factor correction at the residential level – pilot project: report to the LDC tomorrow fund,” September 12, 2005.
- [34] Online: <https://www.wunderground.com/history/> [Accessed May 2019]
- [35] D. J. T. Hill, T. T. Le, M. Darveniza, and T. Saha, “A study of degradation of cellulosic insulation materials in a power transformer, part 1. Molecular weight study of cellulose insulation paper”, *Polymer Degradation and Stability*, vol. 48, no. 1, pp. 79-87, 1995.
- [36] Technical Specification of the Single Phase Distribution Transformer, TUNISIE Transformateurs S.A., Available online: http://www.ttransfo.com/pdf/Mono_eng.pdf [Accessed May 2019]

Chapter 3: Solar-Charged Electric Vehicles: A Comprehensive Analysis of Grid, Driver, and Environmental Benefits

3.1. Introduction

Electric vehicles (EVs) have the potential to significantly reduce greenhouse gas emissions, regulated emissions which cause local air pollution and negative health effects [1], and society's reliance on fossil fuels. Though EV adoption has been slow in the past, the pace has recently been increasing: 2.1 million plug-in vehicles were sold globally in 2018, a 64% increase from 2017 [2]. Yet, in 2018, plug-in vehicles accounted for only 2.2% of the global light vehicle market [2]. Continuing challenges for EV adoption include cost, charging concerns, and range concerns. As EV adoption continues to increase, the generation mix and transmission limitations for charging EVs will become a pressing matter.

With regards to electricity generation, it is well known that the full environmental benefits of EVs can only be realized when charging energy is generated with zero or low CO₂ emissions (e.g., wind, solar, hydro), and that using electricity generated from coal will negate most CO₂ benefits of EVs compared to conventional internal combustion engine (ICE) vehicles. Thus, renewable energy generation and increased EV adoption must go hand-in-hand. Current photovoltaic (PV) cell technology provides energy conversion efficiency of 26.7% for the highest efficiency silicon monocrystalline cells [3], with record 1-sun efficiencies of 38.8% for lab demonstrations of multi-junction cells [4] (which are not

economically practical to date). Most notably for EVs, recent advances have created flexible thin film cells with efficiencies in excess of 20% [5]. Solar deployment has been increasing worldwide, particularly in utility-scale deployments; however, its impact at the individual level (residential rooftop solar) has been slow due to the large upfront cost for installation (e.g. \$23,000 for a 7.5 kW system) [6]. Furthermore, its intermittency (daily and seasonally) and variability (due to weather conditions) makes it an auxiliary source. Its intermittency can be addressed with energy storage, which adds additional significant cost and is a further barrier to deployment for the average homeowner. Thus, many EV owners rely on charging from their local grid, and common evening EV charging adds demand to the grid at peak load times, exacerbating grid emissions.

With regards to electricity transmission and distribution for EV charging, losses and load limitations must be considered. There is an average of 12% loss in energy from large generating stations to local residential loads [7], so for EV charging, it means the EV is actually consuming 12% more generated energy than the energy used to drive the vehicle. Furthermore, most grids present today were not designed for EV charging. Much research has investigated this issue, and a primary concern of having increasing numbers of EVs plugging into the grid to charge is the overloading of distribution transformers [8]-[12]. Most distribution transformers presently in use have been sized to provide the peak loads of the connected homes without EV charging in mind, and thus the additional loading from EV charging can cause overheating, accelerated aging, and eventual

transformer failure. Some previous research has investigated the effect of EV charging on distribution transformers with the use of residential rooftop PV generation: [13] and [14] investigated transformer overloading levels only, [15] investigated the associated transformer loss-of-life in Australia, and [16] analyzed transformer loss-of-life under North American loading conditions, finding that at 50% EV penetration, transformer replacement could be deferred by nearly 4 years when residential rooftop PV was used. Recently, [17] investigated the distribution transformer loss-of-life considering residential rooftop solar shingles, fast chargers, and second-generation battery energy storage. However, no previous work has analyzed distribution transformer overloading and accelerated aging with EVs utilizing on-board solar generation.

To improve both the solar installation cost and storage issues and the EV charging and range issues, this chapter proposes the concept of an EV with low-cost flexible thin film PV cells integrated directly onto the steel of all upwards-facing body panels of the vehicle (i.e., roof, hood, trunk). The solar intermittency issue is resolved because the EV has a large built-in battery already, and thus the required energy storage does not represent an additional cost, as it does with residential solar systems. PV integration during the vehicle manufacturing process opens up the possibility for low-cost mass production, seamless integration, and negligible additional mass of the flexible thin film cells, as opposed to the more expensive and rigid traditional monocrystalline silicon cells. Copper indium gallium selenide (CIGS) cells are currently the best available choice due to their

flexibility, proven ability to integrate onto steel [18], and high efficiency: in this study, 20% nominal efficiency is assumed, though 23.35% has been demonstrated [19], [20]. Though the solar power generated will be low compared to the power needed to accelerate a vehicle, this research will show that the energy obtained over a full day parked or driving outside is significant in terms of reduced grid charging needs at the end of the day, and for driving range extension. With a target mass-production additional cost of \$670 (\$620 for the PV cells [21] and integration and \$50 for power electronics, as discussed in Section 3.4.4), the proposed solar EV (SEV) option would be affordable for a large segment of the population buying EVs, with mature vehicle financing services making the additional cost much more manageable to the average buyer than a residential rooftop installation.

In the past, solar EVs have generally been considered niche development projects, yet some automotive companies are now starting to experiment with solar cells on passenger vehicles. For example, the Toyota Prius Prime and the Karma Revero both have solar cells integrated onto the roof, which charge the propulsion battery [22], [23]. Alta, a maker of thin-film Gallium Arsenide (GaAs) solar cells, claims solar cell efficiencies around 30% [24], though GaAs cells are currently expensive. Audi plans to integrate these Alta cells on the roof of its 2020 EV line, though the solar power will initially only power the low-voltage system, and not the propulsion battery [24]. Furthermore, Sono Motors GmbH is currently developing the Sion EV, which has monocrystalline silicon PV modules fixed onto all vehicle body panels to provide electric range extension [25]. However, this

chapter proposes that significant benefits can be achieved using low-cost thin film PV cells, even with lower nominal efficiency of 20%. Recent research also shows increasing interest in PV on vehicles: [26] proposes EV battery balancing powered by vehicle-rooftop solar panels, [27] develops an electrical architecture for charging the battery from onboard monocrystalline PV cells, [28] proposes reconfigurable PV arrays for on-vehicle use to deal with partial shading, and [29] analyses the benefits of adding monocrystalline silicon PV cells to internal combustion engine vehicles, though does not use detailed vehicle models nor real world driving data. On-board solar has also been investigated for other modes of transportation: [30] presents the design of a solar-assisted electric rickshaw, [31] presents a silicon carbide-based converter with differential power processing for a solar powered aircraft, and [32] presents a switched reluctance motor drive for a solar-assisted hybrid electric bus. However, no previous work has examined the potential system-level benefits of SEVs with low cost and widespread flexible thin film PV cell integration.

The proposed full-scale SEV concept using low-cost, light-weight PV cells integrated onto the steel of all upwards-facing vehicle body panels makes sense from many other perspectives. Firstly, there is a very direct and efficient path for solar energy from PV cell to EV battery, with fewer power conversions than a stationary PV panel charging a stationary storage battery, which later transfers energy to the EV battery. In terms of EV range extension, the full-scale SEV concept is the ultimate wireless charging solution, using free and clean solar energy

to charge the battery when driving or parked anywhere outside. Though much research has been conducted on dynamic wireless charging through the road, obstacles remain including: enormous infrastructure investment needed to retrofit roads, peak driving times often coincide with afternoon peak grid loads [33] [34] meaning new generation could be needed, local grid generation mix might not guarantee low CO₂ driving, and grid transmission losses (about 12%) still exist. From the perspective of vehicle efficiency, automotive engineers spend much effort to increase electric vehicle efficiencies by a few percent: aerodynamic improvements, more efficient motors and power electronics, etc., and there are diminishing returns in this area for the current generation of highly-efficient EVs. However, the proposed full-scale SEV can reduce charging needs by about 20% on average, depending on driving scenarios, which is analogous to an increase in efficiency of 20%. There is not a single other EV development that has the potential for such large grid energy use reductions.

There are also significant challenges to be overcome before mass-produced SEVs can become a reality. Firstly, a low-cost process must be developed to integrate PV cells seamlessly onto the automotive steel panels, with good durability in harsh weather and over time. Secondly, the configuration of series and parallel PV cells must be optimized for maximum power point tracking (MPPT) over the curved vehicle surfaces and for generating high voltages which are easier to boost to the voltage of the traction battery. Thirdly, MPPT tracking controllers must be designed to quickly respond to fast-changing partial shading patterns which can

occur when driving. Fourthly, the electrical architecture and associated power electronic converters, which transfer the PV energy to the high-voltage traction battery, must be designed and optimized for high efficiency, low cost, and low mass. Since there is much future work required to solve these challenges, it is imperative to first assess the system-level benefits of the proposed SEV concept, in order to determine if future design and development effort is warranted – this is the goal of this chapter.

Earlier related work analyzed transformer aging reductions from 10 SEV drivers in one summer week [35], and found significant benefits, indicating that further analysis of SEV system-level benefits is merited. However, actual transformer failures and replacements are based on annual equivalent transformer aging, including aging factors that are much lower in cooler months due to the lower ambient temperatures – thus, the summer-only analysis does not accurately represent annual transformer aging. Furthermore, [35] does not address driver or environmental benefits, does not model the effect of panel tilt, vehicle orientation, or partial shading, nor does it discuss practical SEV challenges. Thus, the contributions of this chapter are: (i) modeling and analyzing the effect of panel tilt, vehicle orientation, and partial shading on captured solar energy at different latitudes; (ii) adding temperature dependency to the efficiency of the solar cells; (iii) investigating grid, driver, and environmental benefits of solar-powered electric vehicles (SEVs) using logged driving cycles from 150 drivers; (iv) expanding the analysis to an entire year, which yields new results that cannot be obtained from a

summer-only analysis; (v) investigating the transformer aging benefit of SEVs in the case of delayed charging; (vi) performing a preliminary analysis on the case where extra solar energy is fed back to the home, and (vii) discussing practical engineering challenges and future trends on the path towards mass-produced SEVs. Section 3.2 describes the data sources used in this research. Section 3.3 discusses vehicle modeling, solar cell modeling and challenges, SEV electrical architecture challenges, and transformer aging modeling. Section 3.4 presents the analysis results for 3.4.1) energy use, 3.4.2) grid benefits, 3.4.3) driver benefits, 3.4.4) environmental benefits, and 3.4.5) economic analysis. Section 3.5 discusses future SEV trends, and Section 3.6 concludes the chapter.

3.2. Data Sources

3.2.1 Vehicle Data

This analysis uses one week of logged vehicle data from 150 drivers of ICE vehicles in Toronto, Canada. Dataloggers were connected to the on-board diagnostic port of each participant's vehicle to log CANbus (controller-area-network) signals including date, time, and second-by-second vehicle speeds of each trip. Since altitude signals were not available on the CANbus, the road grade of each trip is unknown and thus grade is assumed to be zero. ICE driving data is an excellent data source for EV modeling because the logged drivers have no daily range limitations and can thus drive as they naturally need to. MATLAB scripts were created to organize the driving days, which were assumed to start at 12am. Figs. 3.1 and 3.2 show the driving habits of the logged drivers for the 5 weekdays

and 2 weekend days logged – the distribution curves of these datasets are described mathematically in [36]. The logged speed from driving data is fed directly into the SEV Simulink model. The simulated per-day energy use was based on a vehicle model of a Chevrolet Bolt driving the logged cycles, which will be described in Section 3.3. The simulated battery energy use for this base case assumes a 2 kW accessory power load, and a useable battery capacity of 54 kWh, thus there is a spike in the histograms at 54 kWh energy use to account for the ICE vehicles that drove further than the Chevrolet Bolt model could drive.

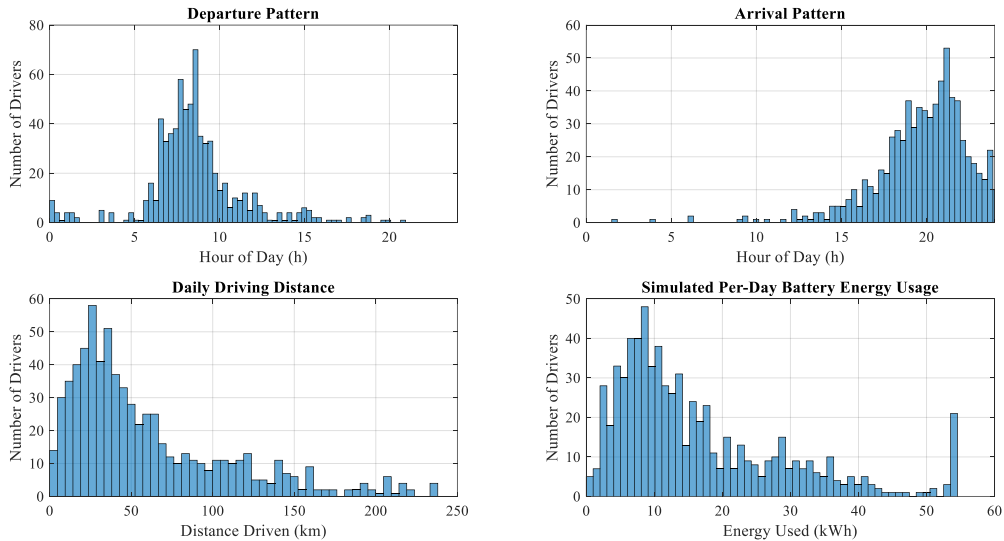


Fig. 3.1. Distribution of departure and arrival times, daily distance travelled, and simulated daily energy requirement for 150 logged drivers over 5 weekdays.

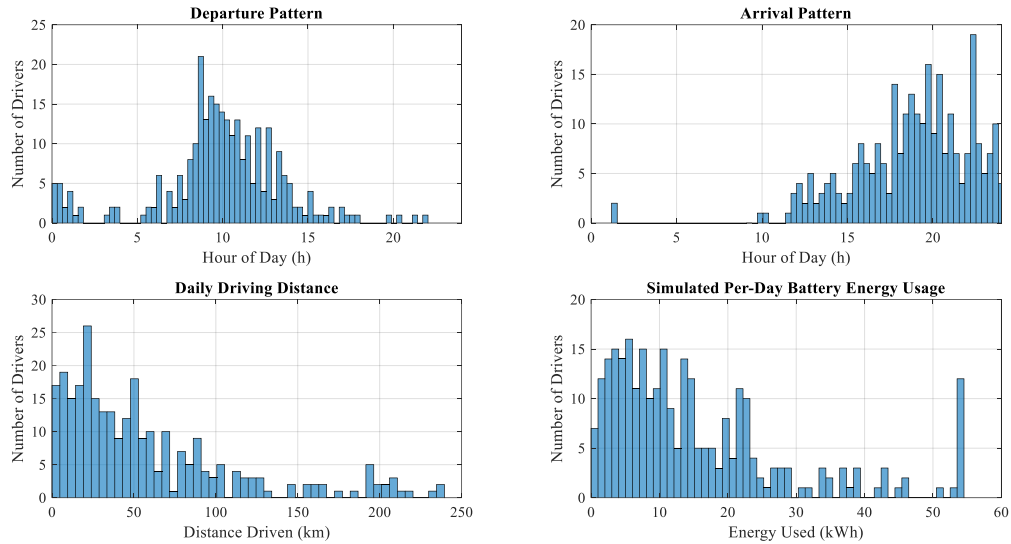


Fig. 3.2. Distribution of departure and arrival times, daily distance travelled, and simulated daily energy requirement for 150 logged drivers over 2 weekend days.

3.2.2 Grid Data

The transformer aging analysis relies on the relationship between the quantity and timing of EV charging to the distribution transformer ratings. This study assumes a distribution grid with 10 houses per distribution transformer, and a maximum of one EV per house. Thus, 15 transformers are considered, meaning at 100% EV penetration (ratios of EVs to homes), each of the 150 unique drivers is assigned to one house. Thus, in an area that commonly has two cars per home, a 100% EV penetration rate would mean that 50% of the cars on the road are electric. This is considered as the upper limit in this study, which could be approached in certain neighborhood clusters or regions in the mid-to-long-term future. For EV penetration rates less than 100%, EVs are assigned randomly within the group of 150 houses to mimic actual EV uptake within a neighborhood, from 0% to 100%

EV penetration, in steps of 10%. Fig. 3.3 shows the monthly per house average residential load profiles without EV charging, as obtained from [37]. In [37], data for every second month of the year was gathered from 200 houses in Florida, and then averaged. In this study, profiles for every month have been generated by averaging the two months around the skipped month. The exception is August, where the load profile is set equal to the July profile. Fig. 3.3 shows an average household load of 2.7 kW and a peak of 3.8 kW in July, and an average load of 1.6 kW and a peak of 2.2 kW in January.

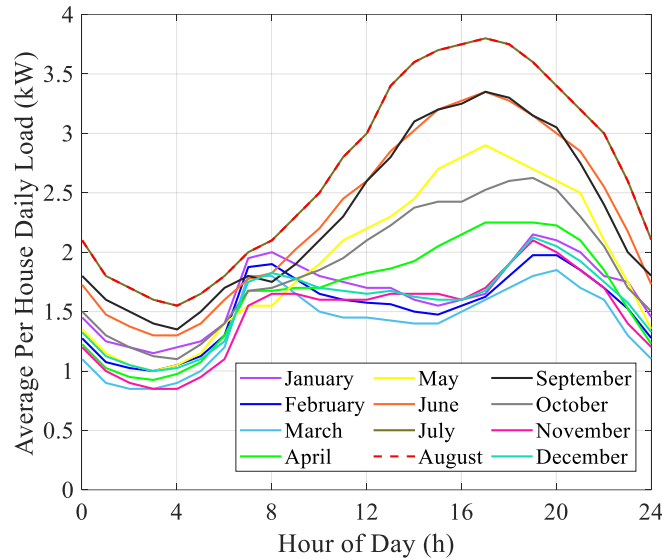


Fig. 3.3. Monthly per house load profile without EV charging.

Distribution transformers sizes are often chosen based on: (i) yearly aging factor, and (ii) maximum overloading. The aging factor will vary month-to-month based on changing loads and the ambient temperature. The transformer is sized so that even with planned overloading, the annual equivalent aging factor (F_{EQA})

equals one, meaning the transformer has aged one year over one year of use. Secondly, maximum transformer overloading must not exceed 200% for power transformers and 300% for distribution transformers [38]. For the given grid load profile, a 25 kVA transformer is selected for each group of 10 houses, and the power factor is assumed to be 0.98 [39]. Thus, the July peak is 38.8 kVA, which is equivalent to 155% loading. With no EV charging, F_{EQA} is calculated to be 1.37 in July in Los Angeles, and 1.07 in July in Detroit, two representative cities that are analyzed in the following sections. Winter F_{EQA} is well below one in both cities, and thus the annual F_{EQA} is less than one for both cities. Thus, a 25 kVA transformer is reasonably sized for the residential load requirements. This study uses a transformer sized well for the residential load, and not oversized for potential future EV charging needs, as this is the most critical concern in current-day distribution systems, as EV penetration rates begin to rise.

3.2.3 Solar and Temperature Data

This study investigates the benefits of solar-charged EVs using annual solar radiation and temperature data for two major U.S. cities: Los Angeles and Detroit. The solar radiation data is obtained from the 1998–2014 National Solar Radiation Database produced by the National Renewable Energy Laboratory using the Physical Solar Model (PSM) [40]. Figs. 3.4 and 3.5 show the annual solar radiation data for Los Angeles and Detroit respectively, both for the case of full sun (as an upper bound) and for the average cloud case. Daily solar radiation profiles are averaged over a month for 21 years (1998 to 2018) to get a single profile to

represent the average daily radiation profile of that month, as shown in Figs. 3.4 and 3.5. On sunny days, peak solar radiation in Detroit is only 7% less than peak solar radiation in Los Angeles. However, on days with average cloud, peak Detroit solar radiation is 19% less than that in Los Angeles. Monthly ambient temperatures of Los Angeles and Detroit, which are used in the transformer aging model, are obtained from [41] and are shown in Fig. 3.6. Temperature profiles for each month represent the average daily temperature profile of the respective month.

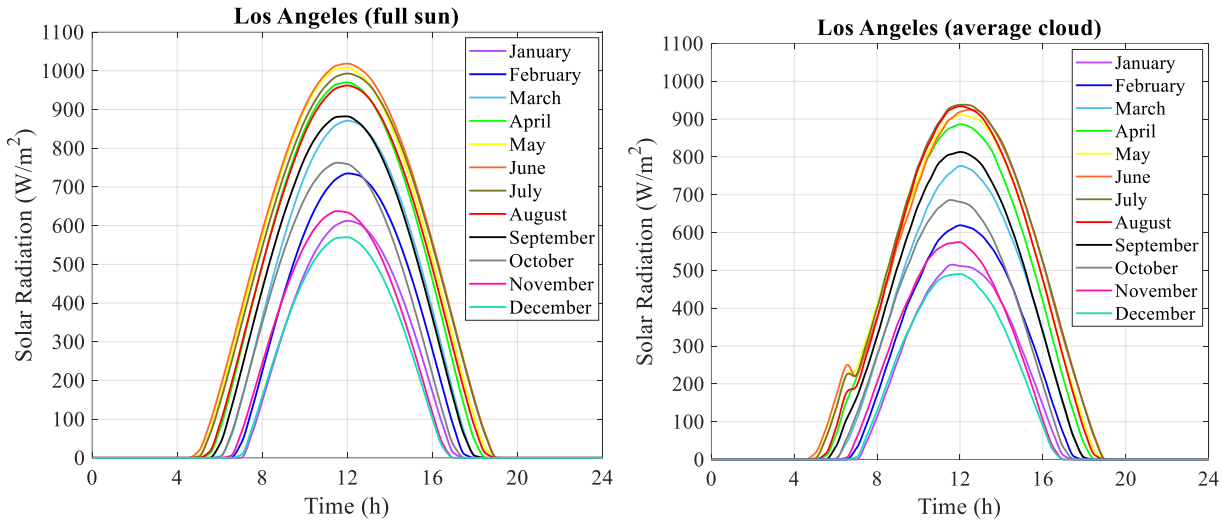


Fig. 3.4. Monthly solar radiation in Los Angeles for sunny and average cloud condition days.

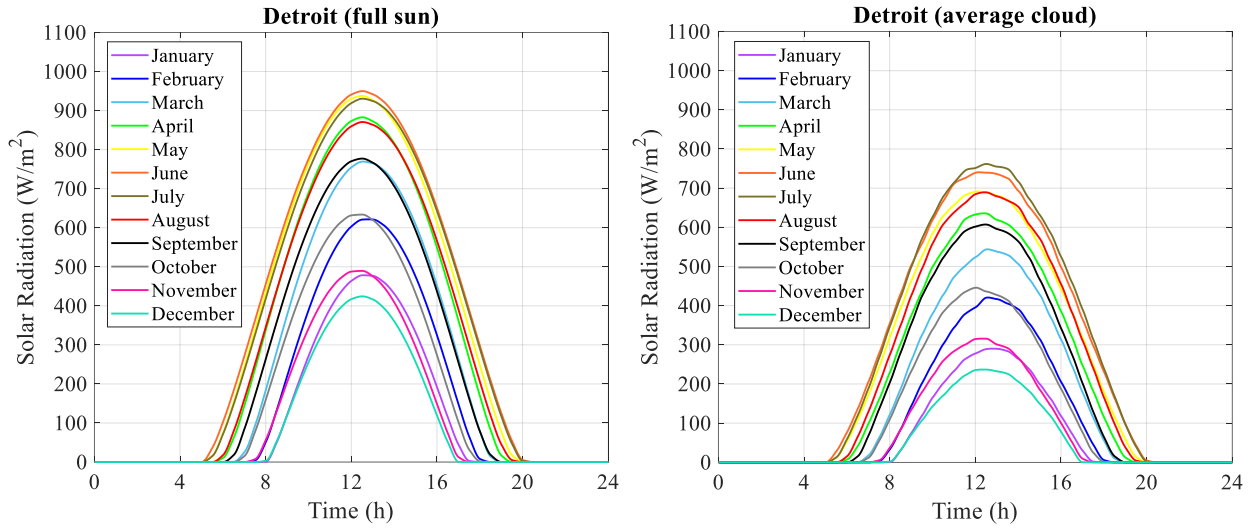


Fig. 3.5. Monthly solar radiation in Detroit for sunny and average cloud condition days.

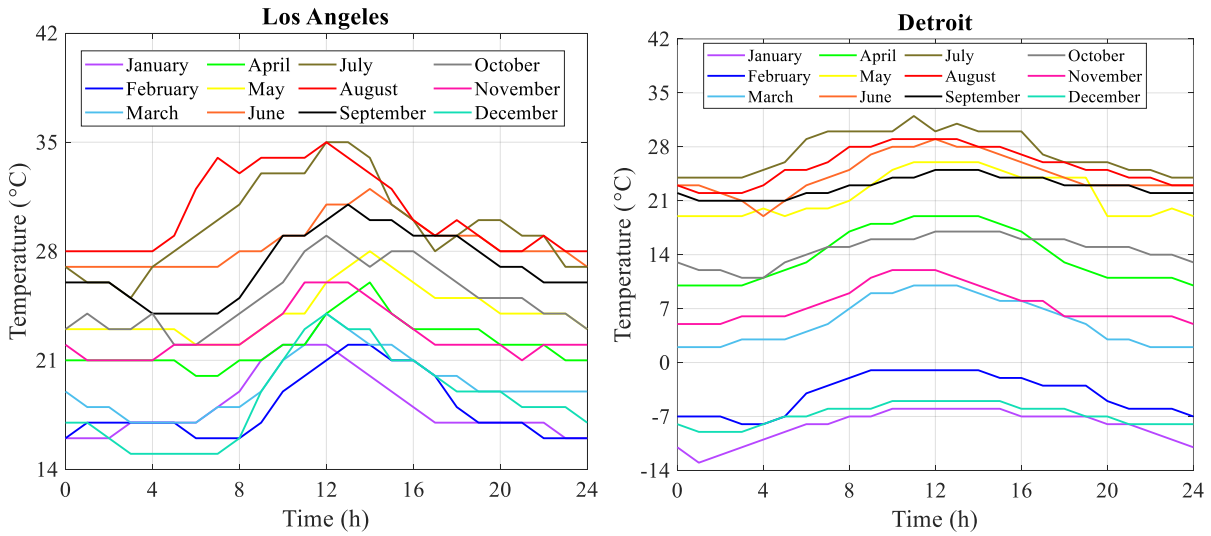


Fig. 3.6. Average daily ambient temperature profile for each month of the year in Los Angeles and Detroit.

3.3. SEV Modeling

3.3.1 Vehicle Modeling

A forward-looking vehicle model of the Chevrolet Bolt EV was created in MATLAB/Simulink, as described below. The non-solar EV version was validated to be within 1.6% of EPA energy usage from dynamometer testing on city and highway drive cycles, as described in [42]. Fig. 3.7 shows a block diagram of the model with the proposed on-board solar assembly included. The on-board solar

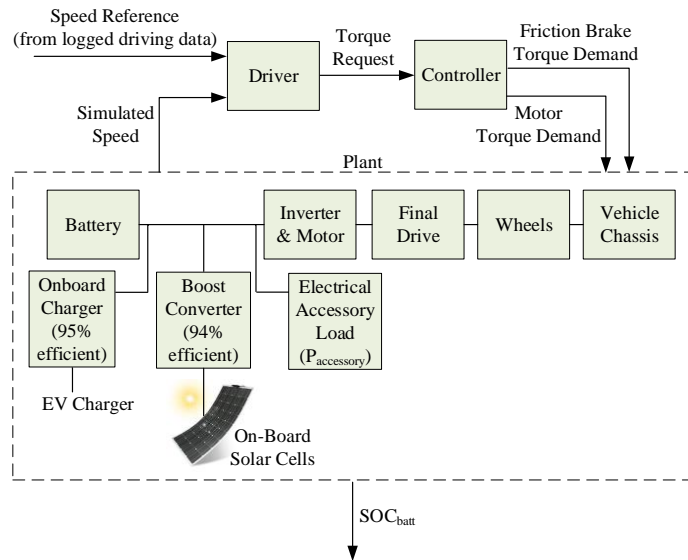


Fig. 3.7. Block diagram of SEV vehicle model.

cells are further discussed in Section 3.3.2 and the solar boost converter and associated power electronics are further discussed in Section 3.3.4. The driver is modeled as a simple PI loop so that the driver torque request is adjusted to follow the speed reference, which is input from the logged drive cycles. The controller block creates the motor torque command and the friction brake command subjected to the driver torque request and the motor speed-torque limits. In the plant model,

the vehicle speed (in m/s) at the next simulation step, $v_{chas}(t+1)$, is calculated from the force out of the wheel block and the chassis aerodynamic losses, as shown in (1):

$$v_{chas}(t+1) = v_{chas}(t) + \left(\frac{1}{m} \int_t^{t+1} \left(F_{out_wheel} - \frac{1}{2} \rho_{air} A C_d v_{chas}^2(t) dt \right) \right) \quad (1)$$

where m is vehicle mass in kg, ρ_{air} is air density (1.23 kg/m³), A is vehicle frontal area in m², and C_d is the coefficient of drag. The force out of the wheel block is calculated from the torque into the wheel block (τ_{in_wheel}), the friction braking torque ($\tau_{friction_brake}$), and the rolling resistance losses, as shown in (2):

$$F_{out_wheel} = \frac{\tau_{in_wheel} + \tau_{friction_brake}}{r_{wheel}} - (\mu_1 + \mu_2 v_{chas}) mg \quad (2)$$

where r_{wheel} is the wheel radius in meters, μ_1 and μ_2 are rolling resistance coefficients, and g is gravitational acceleration (9.81 m/s²). The torque into the wheel block is equal to the motor output torque (τ_{motor}) multiplied by the final drive ratio (r_{fd}) and the final drive efficiency (η_{fd}), as shown in (3):

$$\tau_{in_wheel} = \tau_{motor} r_{fd} \eta_{fd} \quad (3)$$

The motor speed in rad/s is calculated using (4):

$$\omega_{motor} = \frac{v_{chas} r_{fd}}{r_{wheel}} \quad (4)$$

The motor and inverter are modeled as a lumped 2-dimensional efficiency table, with inputs of motor speed and motor torque. The motor/inverter block calculates the DC input current required from the battery using (5):

$$I_{in_motor} = \frac{\omega_{motor} \tau_{motor} \times \eta_{motor}(\omega_{motor}, \tau_{motor})}{V_{batt}} \quad (5)$$

The total battery current (I_{batt}) is the sum of the required motor current (I_{in_motor}) and the required electrical accessory current, minus the current provided by the solar DC/DC boost converter (with efficiency $\eta_{solar_DC/DC} = 94\%$), as shown in (6). It is assumed that solar energy is available when the vehicle is driving or stationary.

$$I_{batt} = I_{in_motor} + \frac{P_{accessory}}{V_{batt}} - \frac{P_{solar} \eta_{solar_DC/DC}}{V_{batt}} \quad (6)$$

The battery model uses the battery current and an initial state-of-charge (SOC) value to determine the SOC and battery terminal voltage at the next simulation step. The SOC is the integral of the battery current divided by the total battery capacity (C_{batt}) as shown in (7). The battery open circuit voltage (V_{batt_oc}) is determined from a look-up table using the current SOC value. The terminal voltage (V_{batt}) is calculated from V_{batt_oc} and the internal battery resistance R_{batt} , as shown in (8). The Bolt EV has a 60 kWh battery, yet the usable energy is somewhat less. This study approximates the usable energy as 90% of the total energy, meaning 54 kWh of energy is available between 5% and 95% SOC. Two grid-connected charging methods are considered: (i) charging is assumed to start at home after the

last trip of the day, known as *Charge Right Away* (CRA), and (ii) charging is delayed until the overnight and early morning times using an available in-vehicle charging method called *Charge By Departure* (CBD). All charging is assumed to occur at a rate of 6.6 kW with an on-board charger efficiency of 95%.

$$SOC(t+1) = SOC(t) + \frac{1}{C_{batt}} \int_t^{t+1} -I_{batt} dt \quad (7)$$

$$V_{batt} = V_{batt_oc} - I_{batt} R_{batt} \quad (8)$$

Though vehicle heating and air conditioning (HVAC) loads will vary driver-to-driver due to personal preferences and weather conditions, it is important to create a model that realistically captures the differences in vehicle energy use across seasons and locations. Maximum continuous heating power is estimated at 4 kW and maximum continuous air conditioning power is estimated at 2 kW. In order to get realistic values of vehicle energy, a look-up table (Fig. 3.8) is added to the Bolt model to approximate HVAC loads based on the external ambient temperature data. An additional 300 W load is added to the HVAC loads for other accessories such as controllers, lights, power steering, etc.

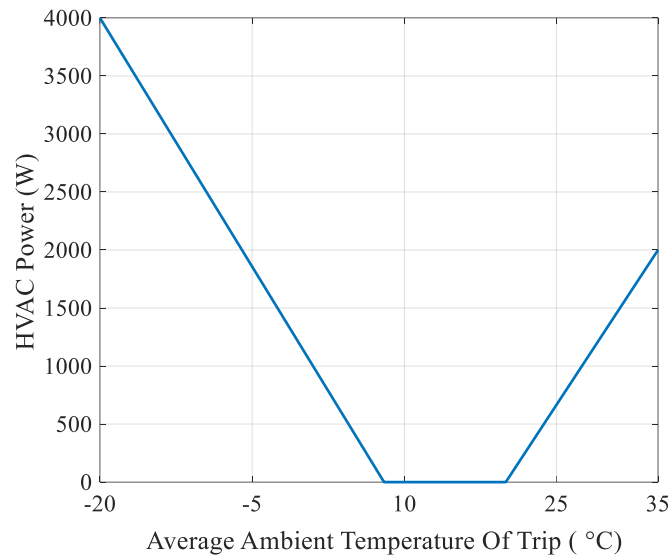


Fig. 3.8. Modeled relation between HVAC power use and trip average ambient temperature.

3.3.2 On-Board Solar Cell Modeling

For the solar cell modeling and analysis of the proposed SEV concept, this section uses parameters from currently available technology to evaluate the plausibility and benefit of a fully integrated SEV, with the understanding that work remains to be done to demonstrate its technical and economic viability. While fixed PV installations are typically installed tilted at latitude in a southward facing direction, a mobile SEV creates new and unique challenges. For a SEV, all directions must be considered equally likely, leading to a strong preference for horizontal and near horizontal surfaces in overall energy capture. However, since vehicles have body panel sections tilted at various angles from horizontal to vertical, the effect of panel tilt on energy capture is an important design consideration. At a high level, the proposed approach is to calculate the energy

capture for a certain panel tilt, θ_t , and then convert this to an energy capture ratio relative to a horizontal (zero tilt) panel. In order to estimate the effect of panel tilt on the energy captured by a SEV panel, calculation of the energy impinging on a tilted solar panel must be averaged over all panel rotation angles Φ , because it is equally likely that a vehicle is facing any direction relative to the sun. This corresponds to a uniform distribution of vehicle orientations. The first step is to calculate the angle Ψ , between the panel normal and the solar direction, and find based on spherical trigonometry that [43]

$$\cos \Psi = \sin \theta_t \sin \theta_z \sin \Phi + \cos \theta_t \cos \theta_z \quad (9)$$

The function $\cos \Psi$ is the projection of the incident solar flux onto the tilted solar panel. Referring to Fig. 3.9, the solar direction is given by the solar zenith angle, θ_z , and the solar azimuth angle (not shown). The panel direction is given by its tilt with respect to the horizontal, θ_t , and its rotation angle, Φ , around the zenith. The solar zenith angle is the angle between the sun's direction and the zenith, a fictitious point infinitely far away, normal to the earth's surface at the position under consideration. With this definition, the zenith angle is 0° when the sun is directly overhead and 90° when the sun is at the horizon. The solar azimuth angle is the rotation angle around the zenith direction, relative to an arbitrary reference angle (such as north), of the vector from the observer to the sun. This angle is not required in the present calculations because of the angle averaging over Φ [43].

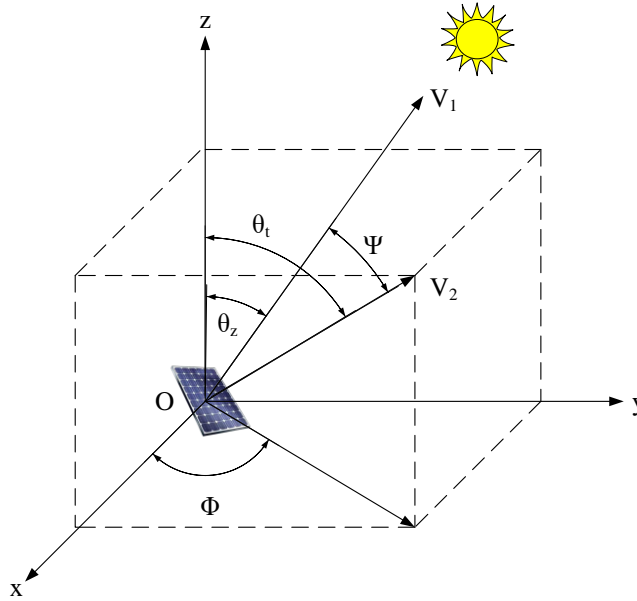


Fig. 3.9. Diagram of the spherical coordinate system used for calculating the projection cosine, $\cos \Psi$. The vector \vec{V}_1 points from the observer, O, towards the sun and is tilted by an angle θ_z from the zenith direction. The vector \vec{V}_2 is normal to the solar panel, which is tilted by an angle θ_t from the horizontal and rotated by an angle Φ around the zenith. The angle Ψ is the angle between \vec{V}_1 and \vec{V}_2 .

The projection cosine, $\cos \Psi$, is then averaged over all angles Φ such that the sun is impinging on the front side of the solar panel to give a function $C(\theta_z, \theta_t)$. Next, for a given latitude, θ_L , the distribution function, $P(\theta_z, \theta_L)$, is calculated for all zenith angles throughout the year (for $0 < \theta_z < 90^\circ$) to weight the projection cosine average in arriving at an annual average [43]. Since the air mass increases as the zenith angle increases, and with it the optical absorption increases, the optical transmission versus zenith angle is also used as a weighting function [43]. The Kasten and Young formulation [44] for the air mass dependence on zenith angle is used, with a function $AM(\theta_z)$, and the Meinel and Meinel treatment [45] of the dependence of the optical transmission with a function $T(AM)$ is also used.

Together, this gives an expression for the annual average solar energy impinging on a tilted solar panel, averaging over all panel presentation angles (because the vehicle is equally likely to face in any direction), as shown in (10) [43].

$$E(\theta_t, \theta_L) = \frac{2}{\pi} \int_0^{\frac{\pi}{2}} C(\theta_z, \theta_t) \cdot P(\theta_z, \theta_L) \cdot T(AM(\theta_z)) d\theta_z \quad (10)$$

For simplicity, the assumption is made that all solar illumination is direct, neglecting the more complex dependence of the small diffuse component on zenith angle and also neglecting variations in aerosol and other atmospheric components. Finally, to facilitate correction of modelled global horizontal irradiance, the energy capture, $E(\theta_t, \theta_L)$, is referenced to that for an untilted panel, $E(0, \theta_L)$, with the results plotted in Fig. 3.10 [43]. While this treatment does not include cloud cover, as a relative quantity it is expected that this energy capture will provide a reasonable estimate of the dependence on panel tilt.

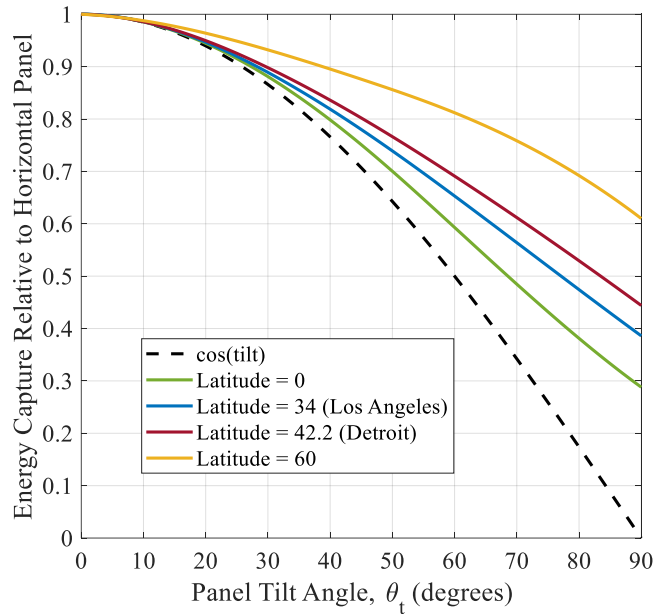


Fig. 3.10. Energy capture on an annual basis vs. tilt of a SEV panel (relative to horizontal) and vs. latitude, with latitude legend in degrees. The energy capture is referenced to the values for horizontal panels (i.e., 0° tilt) [43].

Fig. 3.10 shows that for any latitude and panel tilt, the relative energy capture exceeds the $\cos \theta_t$ dependence shown for reference [43]. At low tilt angles, the decreased power when the panel rotation is such that the panel is tilted further away from the sun is exactly compensated for by the increased power when the panel rotation is such that the panel is tilted towards the sun, leading to a slow (cosine) variation with panel tilt angle [43]. At higher tilt angles, the energy capture falls more slowly than a cosine function with tilt angle because the sun is at high zenith angles that impinge on the tilted solar panel at many times of the day and year [43]. While the *absolute* energy capture (not shown) decreases with latitude, the *relative* energy capture as shown in Fig. 3.10 increases with latitude, since the

average zenith angle increases with latitude, making the tilted panels relatively more effective [43].

In this work, the Chevrolet Bolt is used as the reference vehicle, as shown in Fig. 3.11. In order to apply the results obtained in Fig. 3.10 to the vehicle model, equivalent horizontal solar surface areas are calculated for each city studied, and used in the main simulation. The physical dimensions of the Bolt show an approximately horizontal surface area of 2.33 m^2 (most of the roof) and an 18° slanted surface area of about 1.05 m^2 (including the hood and a slanted portion at the front of the roof). For the locations considered in this work, the relative energy capture for a tilt of 18° is 0.9566 in Los Angeles (downrating of 4.3%) and 0.9583 in Detroit (downrating of 4.2%). For the Bolt, an equivalent effective surface area is calculated as 3.334 m^2 in Los Angeles and 3.336 m^2 in Detroit, corresponding to total downrating factors of 1.35% and 1.30%, respectively.



Fig. 3.11. Reference Chevy Bolt as solar-charged electric vehicle (SEV).

This calculation also permits the evaluation of using vertical solar panels in an SEV context. Fig. 3.10 shows that the relative energy capture for vertical panels

is 0.386 for Los Angeles and 0.444 for Detroit. Due to the significantly lower energy capture for vertical panels and their greater susceptibility to shading in normal traffic conditions, their inclusion would not be justifiable from a cost standpoint and thus have been omitted in the proposed SEV concept. Similarly, it is possible to consider the integration of a transparent PV module into the vehicle's front windshield, but the lost power in the visible part of the spectrum would greatly diminish the potential benefit. Finally, a comparison of the energy capture of a horizontal SEV panel to an optimally tilted fixed PV installation gives a ratio of 0.88 in Los Angeles and 0.81 in Detroit, indicating that SEVs would make a contribution comparable to rooftop installations on a per area basis.

The global PV market is dominated by flat PV modules comprised of monocrystalline or multicrystalline silicon solar cells which achieve high efficiency at low cost. Thin film solar cell technologies are also implemented in flat modules for utility-scale deployment. For the SEV application, this work proposes that a thin film technology with proven mechanical flexibility is the better choice to take full advantage of the benefits of PV integration in a SEV. While other thin film options may emerge in the future, this chapter suggests that copper indium gallium selenide (CIGS) cells are currently the best available choice due to their flexibility, proven ability to be integrated onto steel, and high efficiency [46]. With respect to other thin film PV technologies currently available, CdTe is unlikely to be permitted [47] in new automotive applications due to the chemical toxicity of cadmium, while amorphous silicon has a substantially lower efficiency than CIGS. CIGS cells are

manufactured in moderately high volumes and flexible versions have been successfully deployed for roof applications. A record energy conversion efficiency of 23.35% has recently been demonstrated [19][20] for a research-scale 1.043 cm² area, and 19.2% for a fully integrated module, 841 cm² in area [48]. Based on the record performance module, for illustrative purposes, typical module performance would be $V_{oc} = 0.7$ V, $J_{sc} = 38$ mA/cm² and $FF = 75\%$ under the standard AM1.5G testing spectrum and at 25°C, where J_{sc} is the short circuit current density and V_{oc} is the open circuit voltage. The fill factor FF is defined by $FF = (J_m V_m) / (J_{sc} V_{oc})$, where V_m and J_m , are the voltage and current density at the maximum power point, such that the efficiency, $\eta_{solar} = J_m V_m / P_0$, where P_0 is the incident solar flux.

PV efficiency decreases as cell temperature increases. CIGS cells have a relative efficiency downrating of 0.36% per °C, referenced to 25°C [49]. In this study, 20% module efficiency (η_{solar}) at the nominal 25°C is assumed as a realistic number attainable over the next 5 years. The resulting PV efficiency as a function of cell temperature is shown in Fig. 3.12. The cell temperature is calculated based on the ambient temperature (T_{Air}) and the solar insolation (S) in W/m², as shown in (11) [50]. In order to find an approximate peak solar power for sizing the electrical system, P_{solar} , S should be set high such as 1000 W/m², and T_{Air} should be set low, such as 10°C. Using the effective horizontal solar area of 3.334 m² in Los Angeles, this results in a cell efficiency of 18.6%, with peak generated solar power, P_{solar} , equal to 620 W.

$$T_{Cell} = T_{Air} + 0.035S \quad (11)$$

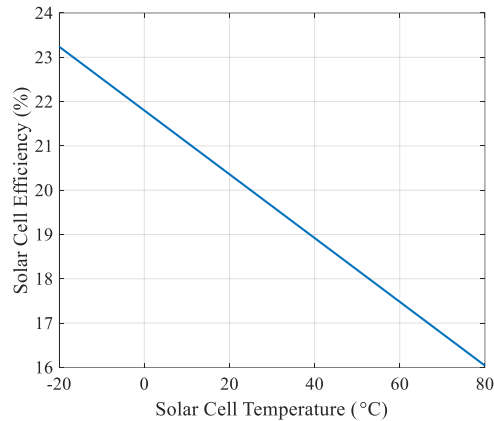


Fig. 3.12. Estimated CIGS cell efficiency as a function of cell temperature.

As a fairly mature technology, the environmental impact of CIGS cell manufacture and deployment through its life cycle is well understood [51]. While the cells are comprised of gallium and indium, which are neither inexpensive nor earth abundant, their use in a thin film format is believed to be feasible for SEV applications even at global scale [52], particularly if CIGS is not widely deployed in the utility-scale market and if recycling is implemented. Selenium is also moderately rare and since its compounds are toxic in high doses it must be recycled and disposed of with appropriate caution. CIGS cells commonly include a very thin layer of CdS, but can be made cadmium- and lead-free. Solar panels of any type have not yet been in production for long enough at scale to have an established recycling protocol in all countries [53]. Outside of Europe, discarded PV panels are considered ‘general waste’ whereas within Europe panel disposal falls under the Waste Electrical and Electronic Equipment (WEEE) Directive [54]. Laws and

regulations governing end of life recycling of automobiles are expected to be sufficient to ensure that CIGS cells are properly recycled or disposed of, such as the European Union's End of Life Vehicles (ELV) Directive [55]. Recycling of the rare elements in CIGS cells has been demonstrated, and due to the high cost of gallium and indium is considered economically very advantageous [56]. Via accelerated testing protocols, CIGS cells have been demonstrated to have usable lifetimes in the field, with typical power degradation of less than 10% over 10 years and less than 20% over 25 years, a standard warranty requirement for utility-scale PV [57]. While high temperature processing is used in the manufacture of CIGS cells, as a thin film technology the energy input is low, leading to an energy payback time of less than 1 year, depending on manufacturing process and location of deployment [58].

In the manufacture of a CIGS module, the device layers are deposited in a batch fabrication process, sectioned into multiple electrically isolated cells which are then interconnected into a series string via a set of patterning processes [59]. This architecture is generally referred to as monolithic cell interconnection and requires an insulating layer or substrate in order to enable electrical isolation of the cells. Without this sectioning, a single 1 m^2 CIGS cell would have $V_{oc} = 0.70 \text{ V}$ and $I_{sc} = 380 \text{ A}$. By sectioning into 100 cells, with a series interconnection, this becomes a much more manageable $V_{oc} = 70 \text{ V}$ and $I_{sc} = 3.8 \text{ A}$, which is typical for rooftop and utility scale applications. Such series-connected panels are then combined in parallel to provide more overall power. There are several potential benefits to a

greater level of sectioning for the SEV application under consideration. Firstly, the voltage can be increased to be closer to the EV battery voltage (250 to 450 V), meaning less voltage boost is needed in the DC/DC converter and thus higher DC/DC converter efficiency can be obtained. Secondly, by achieving a higher voltage and lower current, losses associated with series resistances are reduced. This also permits the use of thinner wires, reducing cost and weight. A real advantage of thin film PV is that there is tremendous flexibility in the level of sectioning and even the opportunity to adapt the cell size and interconnection pattern to take full advantage of curved surfaces on automotive sections. This is in contrast to silicon PV technology where individual cells are batch fabricated in a fixed size format, such as $15 \times 15 \text{ cm}^2$. A novel approach to boosting voltage via series-connected PV strings is by stacking cells vertically with cell thicknesses adjusted to maintain a current-matched condition. This concept has been demonstrated in monolithically-grown GaAs photoreceivers with stacks of over 20 lattice matched cells [60], employed for telecommunications applications. For SEV applications, some optimization in cell size and interconnection pattern will be required to achieve the best overall energy yield. The flexibility provided by thin film sectioning and/or cell stacking provides additional degrees of freedom to do so.

CIGS cells are most typically grown on a rigid glass substrate that also serves as mechanical support for the PV module. However, commercial CIGS cells are also made on flexible substrates, using roll-to-roll manufacturing [59]. In order

to implement monolithic cell interconnection as described above, the flexible substrate must either be insulating or a flexible metal foil with an intervening insulating layer. In the latter case, the insulating layer can also serve as a source of sodium dopants and/or as a diffusion barrier from impurities in the metal substrate. High quality CIGS cells have been grown on stainless steel using SiO_2 , Al_2O_3 or Si_3N_4 insulating layers [59]. The record efficiency to date for CIGS on stainless steel is 20.56% for a research-scale 0.86 cm^2 area [61]. More recently, high quality CIGS cells have also been demonstrated on mild steel substrates [62], suggesting that CIGS cells could be grown directly on automotive steel parts with suitably optimized layers for insulation, doping, corrosion protection and for inhibiting impurity diffusion. CIGS cell growth is typically followed by a polymer encapsulant such as EVA, providing long term hermeticity. In an SEV context, the encapsulant needs to be replaced with an automotive paint that is hermetic, provides mechanical protection and is optically transparent over the relevant part of the spectrum ($\sim 350\text{-}1100 \text{ nm}$ for CIGS), which includes the entire visible spectrum. This constraint would likely limit the aesthetic design flexibility and may limit consumer acceptance; however, creative marketing, such as what Tesla has done for EVs in general, may minimize this issue. For a CIGS cell fully integrated onto the automotive steel and encapsulated as described, the incremental mass from the CIGS layers would be only $\sim 40 \text{ g/m}^2$, for a total mass of 133 g. The overall mass increase is likely to be dominated by wiring, bypass diodes and DC/DC conversion components, which are estimated to be less than 4 kg for a 700 W system.

This analysis assumes low-cost 20% efficient (nominal) CIGS thin film PV cells because this approach is currently feasible for the proposed SEV application. However, the resulting benefits will increase if more efficient cells are used, such as GaAs thin film PV cells with 29% efficiency. The manufacturing cost of GaAs thin film cells is currently very high, but cost reduction is an active area of III-V semiconductor PV research [63]. The high cost is due to contributions from an expensive GaAs growth substrate and the high cost of ownership of the metal-organic chemical vapor deposition (MOCVD) reactors used to grow the cells, due to the relatively slow growth process [64]. The substrate costs can be substantially mitigated by epitaxial lift-off from the parent wafer and subsequent wafer reuse. The MOCVD-related costs can be reduced by the development of higher growth rate processes [63], the use of larger wafers and larger batch sizes, and improved precursor utilization. Thus, higher efficiency GaAs thin film cells may become viable options for SEVs in the future. Alta Devices, which holds the GaAs efficiency record [65], is currently developing GaAs cells for a number of high-end transportation applications.

3.3.3 Modeling of Partial Shading

The range of potential partial shading scenarios is wide and will depend on each driver's unique environment (urban, country, nearby buildings and/or trees). Thus, this research will study one representative case that can offer insight into the effects of typical shading scenarios. In this case, a vehicle is parked 5 ft away from a 15 ft tall structure, where the vehicle and structure direction are set to the worst

case where the sun rises directly behind the structure. To represent changing vehicle positions over a day, the case is modeled such that in each hour of the day, the structure is on the left side of the vehicle for 20 minutes, the structure is on the right side of the vehicle for 20 minutes, and the structure is absent for 20 minutes. This pattern is repeated through the day, as the sun changes position.

Fig. 3.13 shows the case with the structure on the left side of the vehicle, where the average height of the vehicle's solar panels is estimated at 5 ft. The sun will start shining on the far side of the vehicle when the zenith angle, θ_{z1} , decreases to 42.98° . As the sun moves, the radiation on the vehicle solar panels will increase – the solar panels will be in full sun when the zenith angle, θ_{z2} , decreases to 26.57° .

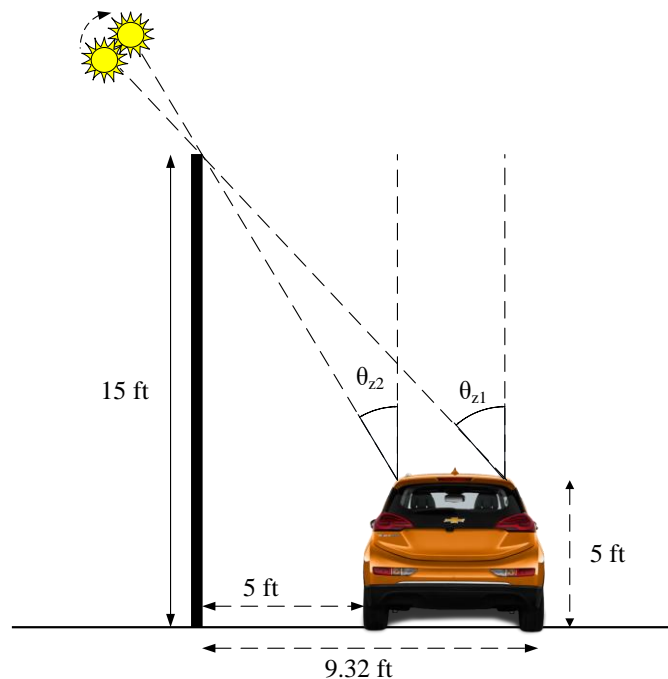


Fig. 3.13. Example case for partial shading modeling (structure on left side of vehicle).

This analysis leads to two important findings: (i) since the peak solar radiation

occurs around midday, when the zenith angle is the lowest, partial shading will have little or no impact on the solar energy captured during this peak solar energy time (i.e., when the sun is high in the sky, more directly above the vehicle), and (ii) since the zenith angle does not reach 26.57° in the winter and some spring and fall months of the year (as shown in Fig. 3.14), there will be zero solar energy captured in these months when the structure is between the sun and the vehicle.

When the partial shading hourly pattern is repeated as described over a day, the solar radiation pattern becomes choppy and variable, as shown in Fig. 3.15. The monthly solar energy generated decreases the most in the winter months due to the high zenith angles – by about 33% in January in both Los Angeles and Detroit. However, in July, the solar energy reductions are only 13.8% and 17.3% in Los Angeles and Detroit respectively, due to the lower zenith angles of the sun. The

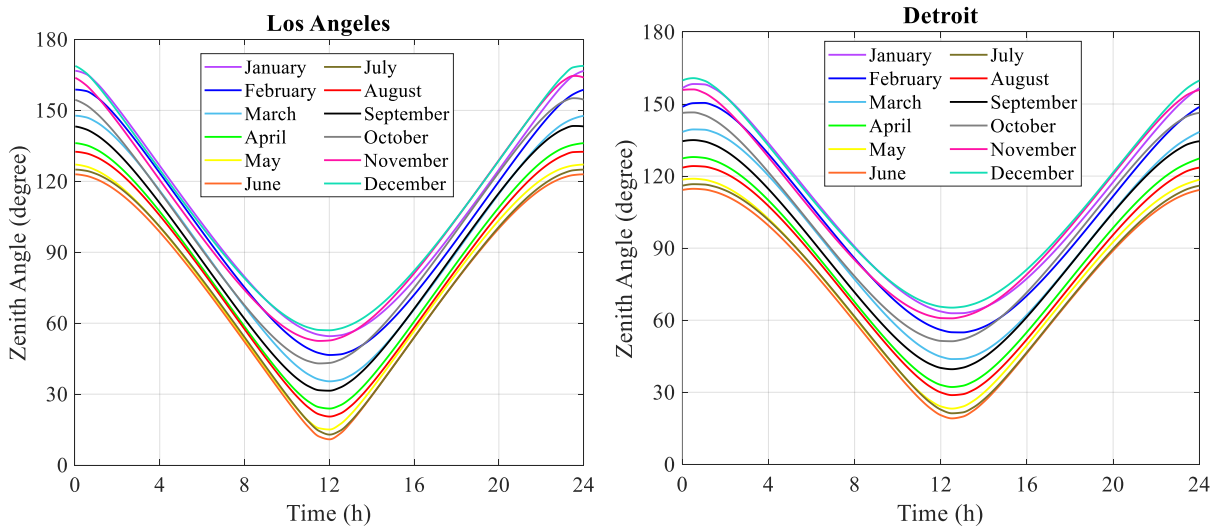


Fig. 3.14. Monthly average zenith angle profile for Los Angeles and Detroit.

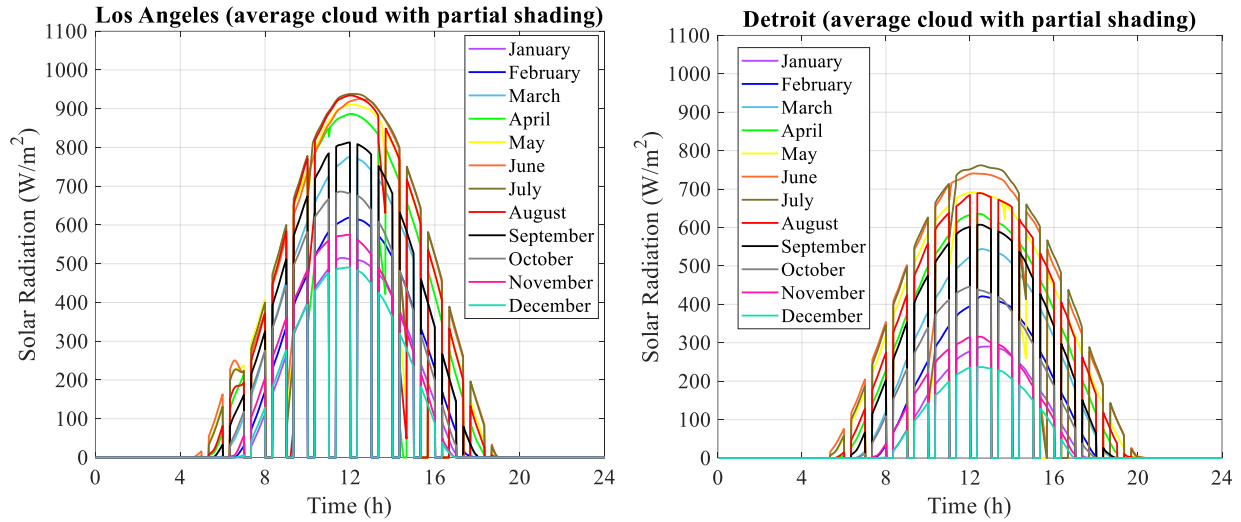


Fig. 3.15. Monthly partial shading solar radiation models for Los Angeles and Detroit.

solar radiation curves shown in Fig. 3.15 are based on average cloud conditions, and will be used for the partial shading simulations in this work.

3.3.4 SEV Electrical Architecture and Challenges

Though this chapter focuses on the system-level benefits of SEVs to investigate if further detailed engineering work is warranted, it is also important to understand the technical challenges of designing a low-cost and high-efficiency SEV electrical architecture. The optimal design of the electrical architecture for a SEV is a multi-faceted problem because it depends on the PV cell size and connection scheme, the PV cell voltages, and the power electronic converters, where optimal converter choices can change depending on the first two variables. This section will discuss design issues on the path towards a low-cost, low-mass, and high-efficiency SEV electrical architecture.

With regards to PV cell size, the proposed thin-film CIGS material can be used to effectively make cells of various sizes. Larger cell sizes mean fewer interconnections are needed, but lower voltage is produced from a string of cells connected in series. A related challenge is to decide how many cells should be connected in series and parallel. More cells in series connection boosts the resulting voltage, but if any shading occurs in the series string, the solar power will be reduced for the entire string. Since much of the harvested solar energy may be obtained while the vehicle is parked, an optimal design should allow for maximum solar power production even when parts of the vehicle body are in the shade. However, if fewer cells are connected in series, the low resulting voltage will require high boost to the traction battery voltage, which generally leads to poor efficiency. Previous research on MPPT for partially shaded PV cells indicates that the most common methods for dealing with partially shaded cells are to use bypass diodes (low cost) or to add DC/DC converters to each cell (higher efficiency, higher cost) [66]-[68]. Also related to MPPT is the issue of the slightly curved nature of some vehicle surfaces, such as the hood. Since PV panels are generally considered as flat surfaces, further research is required to determine how to extract the maximum solar power from PV cells distributed over a curved surface. However, the problem is similar to that of partial shading in that each cell along the curve will have a different maximum power point, so similar techniques may be able to be applied to this problem. In this research, it is assumed that MPPT is used in the system, meaning the full available solar energy can be captured.

The main power electronic challenge is to boost the PV voltage to the high traction battery voltage, which commonly varies between 250 V and 450 V in EVs. Though a 12 V battery is used in EVs for low-voltage accessories, the energy capacity of these often lead-acid batteries is not sufficient to store solar energy gathered over long periods of time. Many architectures can be considered and Fig. 3.16 shows two potential strategies: (1) keep the PV voltage low (by using a low number of cells in series) and reuse the bidirectional high-voltage to 12 V DC/DC converter already present in most EVs, or (2) create high PV voltages using vertically stacked cells and/or more cells connected in series, and then boost the voltage to the traction battery voltage using dedicated DC/DC converters. The advantage of Option 1 is that cost is reduced by re-using the existing DC/DC converter for the main voltage boost to the traction battery voltage. The disadvantage of Option 1 is that lower efficiency is expected due to: (i) higher currents in each MPPT converter due to the lower input voltage, (ii) the existing bidirectional DC/DC converter is usually sized between 2 kW and 4 kW, and thus may have poor efficiency at the 200 W to 620 W level of solar power in the proposed SEV, and (iii) solar power must be processed by two DC/DC converters before reaching the traction battery. The advantages of Option 2 are: (i) higher voltages are used, generally leading to higher efficiency, and (ii) the dedicated DC/DC converters will be higher efficiency due to less voltage boost required and the possibility to optimize the design solely based on the lower solar power levels. Yet the high step-up MPPT boost converters in Option 2 will add additional cost

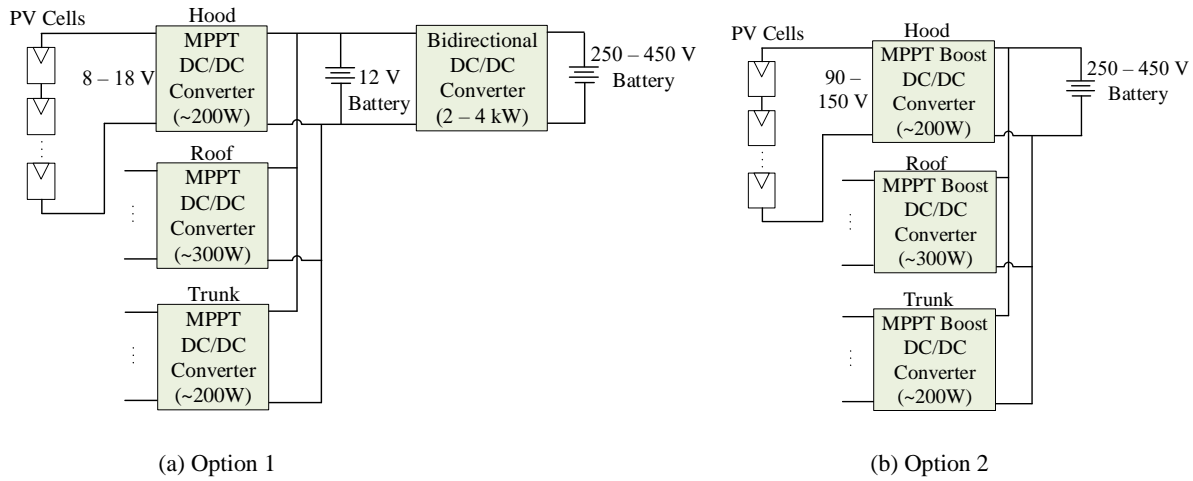


Fig. 3.16. Two potential electrical architecture options for the proposed SEV.

compared to Option 1. For a system-level analysis, it is not critical to design the details of the SEV electrical architecture, yet a reasonable approximation of losses in the architecture must be used so that harvested solar energy is correctly estimated. In this work, Option 2 is assumed and the total efficiency of the power electronic converters in the path from the PV cells to the traction battery is estimated at 94% based on similar high step-up boost converters [69], [70].

3.3.5 Transformer Aging Model

The main concern in overloading distribution transformers with household and EV charging loads is accelerated transformer aging. Thus, the equivalent aging factor, F_{EQA} , is a useful metric for comparing the EV charging effect on transformers. Transformer aging is mostly due to the degradation of the insulation; this depends on temperature, moisture, and oxygen content. In modern oil-cooled transformers, the effect of moisture and oxygen content on insulation deterioration can be neglected. Thus, transformer accelerated aging is mainly related to the

hottest-spot insulation temperature [38]. This study uses the overhead distribution transformer aging model from IEEE C57.91-2011 [38], as summarized below (full details are given in [38]).

The total household load plus the simulated EV charging load are converted to an equivalent load, L_{equiv} , using (12):

$$L_{equiv} = \sqrt{\frac{L_1^2 \Delta t_1 + L_2^2 \Delta t_2 + \dots + L_n^2 \Delta t_n}{\Delta t_1 + \Delta t_2 + \dots + \Delta t_n}} \quad (12)$$

where L_1, L_2, \dots, L_n are various kVA load values including the baseline household load and the EV charging load that has been simulated for that particular driver on each day of the logged week, and for each month where HVAC loads vary by the month. These L_1, L_2, \dots, L_n , loads are specified in one-minute intervals $\Delta t_1, \Delta t_2, \dots, \Delta t_n$ respectively, so that high resolution charging patterns are used in the transformer aging analysis.

The hottest-spot temperature, θ_H , is the summation of three temperature components in °C [38] as shown in (13): ambient temperature, θ_A , delta between the top-oil temperature and the ambient, $\Delta\theta_{TO}$, and delta between the hottest-spot temperature and the top-oil temperature, $\Delta\theta_H$.

$$\theta_H = \theta_A + \Delta\theta_{TO} + \Delta\theta_H \quad (13)$$

θ_H is directly related to the insulation life of the transformer. $\Delta\theta_{TO}$ and $\Delta\theta_H$ are dependent on L_{equiv} and other variables as described in [38]. F_{AA} is defined as

the aging acceleration factor, and is an exponential function of the hottest-spot temperature θ_H as shown in (14).

$$F_{AA} = e^{\left(\frac{B}{383} - \frac{B}{\theta_H + 273}\right)} \quad (14)$$

In (14), B is the cellulose aging rate constant, with a value of 15,000 based on the transformer insulation life curve in [38]. The transformer specification data were obtained from [71].

The equivalent aging factor, F_{EQA} , is a useful parameter because it represents how fast a transformer ages based on its thermal profiles compared to the normal condition. For example, $F_{EQA} = 1$ means the transformer has aged 1 week over the test week period, and $F_{EQA} = 2$ means the transformer has aged at double the normal rate, or 2 weeks over the test week period. F_{EQA} is described by (15), where Δt_n is each time interval, N is the total number of time intervals, and F_{AA_n} is the aging acceleration factor during the time interval, Δt_n .

$$F_{EQA} = \frac{\sum_{n=1}^N F_{AA_n} \Delta t_n}{\sum_{n=1}^N \Delta t_n} \quad (15)$$

3.3.6 Simulation Process

The first step in the simulation process is to consolidate individual logged trips into driving days, where the end of the last trip before 12am constitutes the end of a driving day, with the next driving day starting on the next trip after 12am.

For each trip, the logged data gives the actual date and start time of the trip – using this data, the correct “day of the week” is assigned to each driving day, as, for example, the driving patterns on a Wednesday will differ significantly from those on a Saturday. Thus, the logged driving data gives a very accurate account of an actual week of driving for each of the 150 participants. For each driver, the Bolt EV model is simulated on the speed profiles of each trip of the logged days and the simulated ending battery state-of-charge (SOC) of one trip is fed back into the vehicle model as the starting SOC for the next trip that day.

To create an annual analysis, this work assumes that the driving pattern of an individual will remain static across all weeks of the year. The simulation process is summarized in Fig. 3.17, where “LUT” represents a look-up table. For each of the 12 months of the year, the driving week for each participant is simulated under ambient temperature and solar radiation conditions (full sun, average cloud, and average cloud with partial shading) for Los Angeles and Detroit. The result is 12 unique monthly values for vehicle energy used and grid charging energy needed for

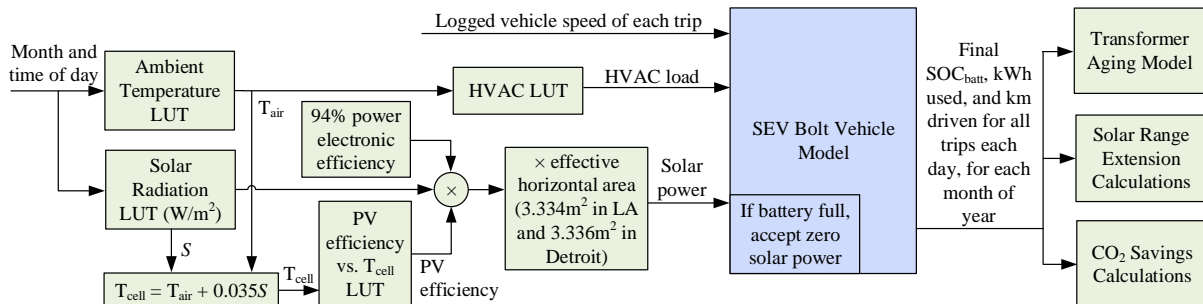


Fig. 3.17. Summary of simulation process. This process is looped: for 150 drivers, for each day of the week, for each month of the day, for full sun, average cloud, and average cloud with partial shading conditions, and in two cities. This is also then rerun with solar radiation = 0 to represent the non-solar EV case.

each driver in each city, which are used in the transformer aging model to obtain an annual transforming aging estimate. These simulation results are also used in the solar range extension and CO₂ savings calculations, as part of the driver and environmental analysis. For all simulations, a case is also run with solar radiation set to zero to represent the non-solar EV case.

To illustrate the simulation result details, Fig. 3.18 shows the driving pattern and resulting battery SOC of Driver #1 on one logged day, both with and without using on-board solar energy. The results show that the battery pack cannot start storing solar energy until the vehicle starts driving for the day (with the assumption that full charge is obtained from the grid overnight), and that significant solar energy can be stored during the parked times of the day thereafter. On a sunny July day, if both EVs start at 95% SOC, the SEV SOC ends at 80.54% and the non-solar EV SOC ends at 73.31%. Thus, at the end of the day, the SEV needs 8.68 kWh of charge from the grid and the non-solar EV needs 13.01 kWh, a reduction of 4.33 kWh or 33.3%. Solar charging stops in the late afternoon due to sunset.

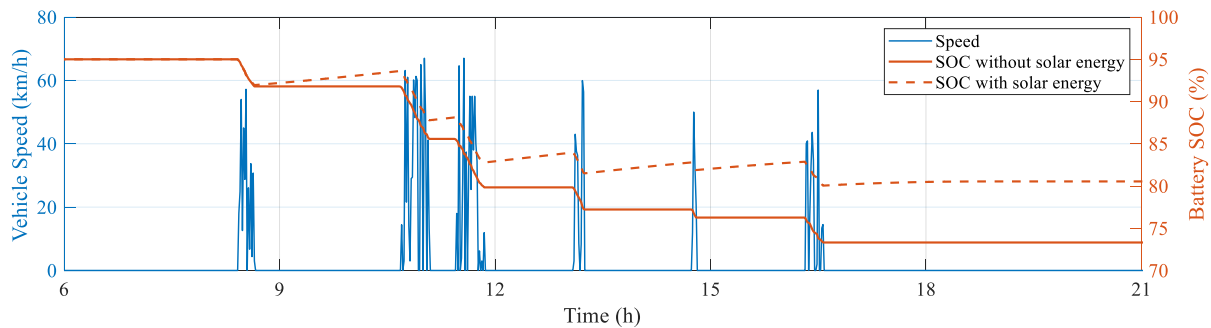


Fig. 3.18. Vehicle speed and battery SOC for driver #1 over one example day, both for an EV without on-board solar, and the proposed SEV.

3.4. Simulation Results and Discussion

3.4.1 Energy Use

All grid, driver, and environmental benefits ultimately stem from the reduced net vehicle energy consumption of SEVs compared to non-solar EVs. For the proposed large-scale integrated SEV concept in average cloud conditions, the annual vehicle energy consumption is reduced by 21.5% in Los Angeles and by 17.5% in Detroit. For comparison purposes, the sun rich location of Solar Village, Saudi Arabia (latitude 24.91° and relative energy capture 0.9555) is also analyzed, as it has excellent solar radiation data available [72]. A combination of high incident solar energy and high ambient temperatures, as shown in Fig. 3.19 [41][72], result in high vehicle HVAC energy use during most of the months and an annual vehicle energy consumption reduction of 22.7% in average cloud conditions compared to a non-solar EV in Saudi Arabia. Furthermore, the analysis was also performed for Los Angeles using a small vehicle rooftop solar panel such as that on the Toyota Prius Prime [22]. With a peak claimed output of 180 W [22], the panel size is estimated at 1 m^2 assuming the same efficiency as the cells modeled in this study. For comparison purposes, this vehicle rooftop solar panel would result in 7.6% reduction in annual vehicle energy consumption in Los Angeles under average cloud conditions, compared to a non-solar EV.

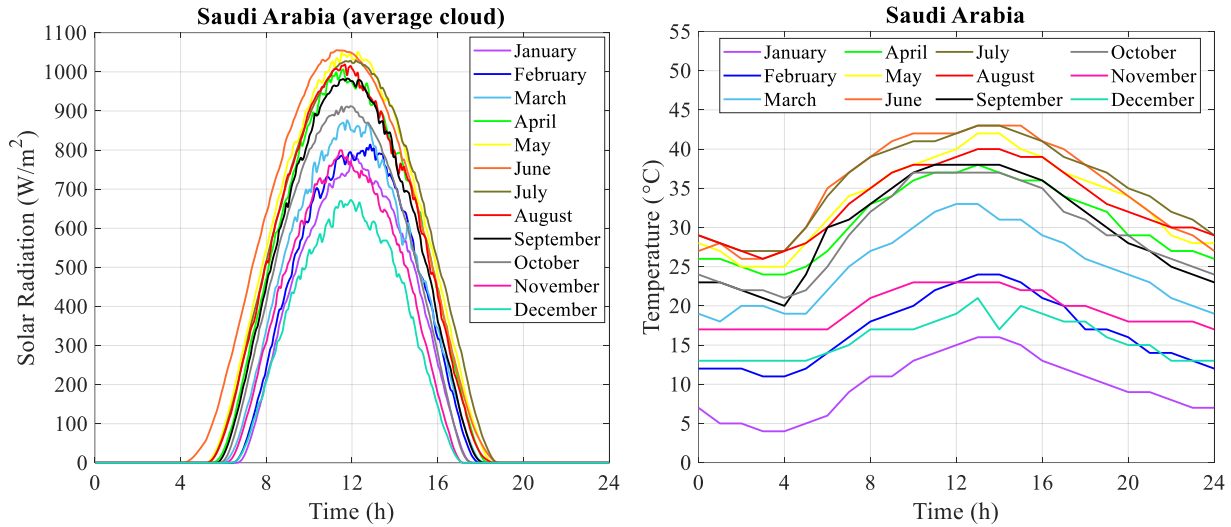


Fig. 3.19. Average daily radiation and ambient temperature profile for each month of the year in Saudi Arabia.

3.4.2 Grid Benefits

The main grid benefit of utilizing SEVs instead of non-solar EVs is the reduction in load during peak times of the day – this will lead to lower loads on distribution transformers (and thus lower aging), lower loads on transmission lines (and thus lower losses and lower potential for overload), and lower peak energy generation. This research focuses on modeling the reduction in aging of distribution transformers with the use of SEVs, as this is a pressing concern as EV adoption rises in neighborhoods with older distribution grids. EV charging has been simulated based on the simulated energy use of each logged driver and the unique arrival time home of each logged driver. The total load (residential + EV charging load) for 150 EV drivers (100% EV penetration) using *CRA* charging is shown in Fig. 3.20 for the logged Wednesday in July. The temperature profiles in this hot month are similar for both the cities, and therefore the vehicle energy consumption

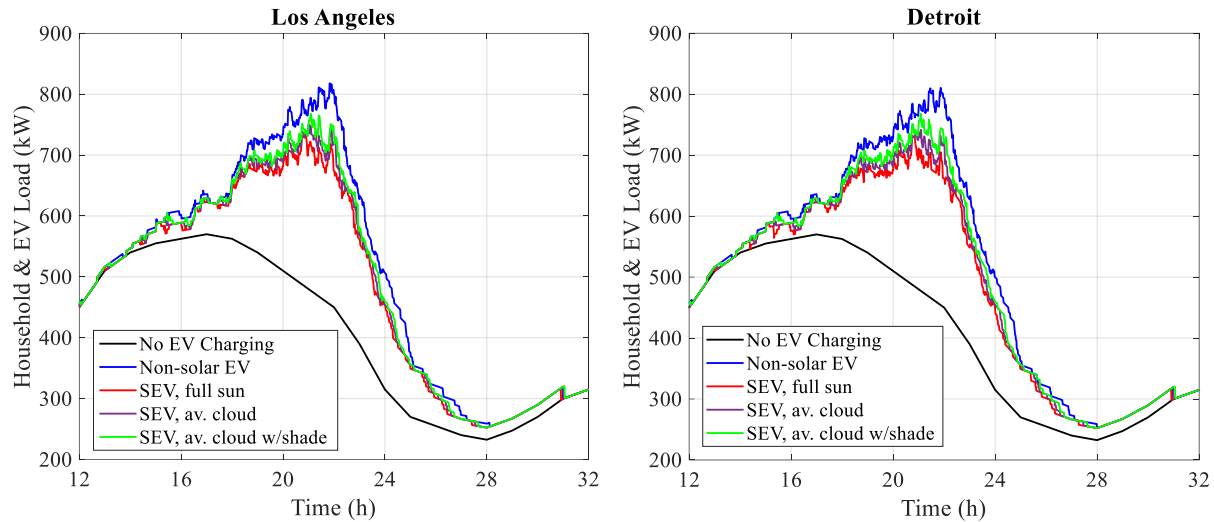


Fig. 3.20. Household and EV charging load for 150 EVs and 150 houses for non-solar EV, SEV on a day with full sun, average cloud conditions, and average cloud conditions with partial shading (CRA charging).

due to HVAC is similar for both cities. The total charging energy consumed by 150 EVs at the plug in Los Angeles and Detroit on a typical Wednesday in July is 2.20 MWh and 2.14 MWh, respectively. When these EVs are replaced by SEVs, the charging energy consumption is reduced to 1.61 MWh, 1.63 MWh, and 1.68 MWh for full sun, average cloud, and average cloud with partial shading cases in Los Angeles, and 1.53 MWh, 1.59 MWh, and 1.66 MWh, for the same cases in Detroit. The peak power reduces from 817 kW to 735 kW in Los Angeles and from 810 kW to 732 kW in Detroit for the SEV full sun case. The main effect of the SEV is that although charging start times remain the same compared to the case of non-solar EVs, the charging end times are earlier (though unique for each driver) due to the higher ending SOC of the vehicle at the end of the driving day for SEVs. As shown in Fig. 3.20, this reduced charging duration significantly lowers the total load in the evening.

The 15 distribution transformers are not evenly loaded as every EV has its own charging requirement. Fig. 3.21 shows the detailed charging profile of one

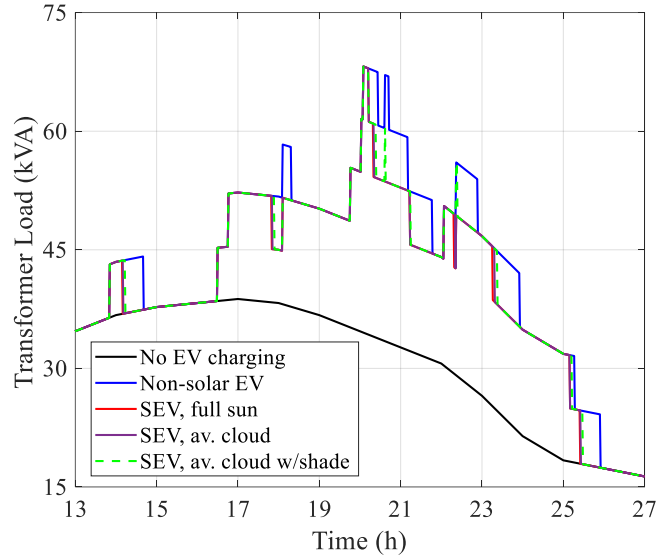


Fig. 3.21. Household and EV charging load for one transformer for non-solar EV, SEV on a sunny day, SEV on a day with average clouds, and SEV on a day with average clouds and partial shading (CRA charging).

transformer feeding 10 homes simulated with 10 SEVs and with 10 non-solar EVs using *CRA* charging on a Wednesday for Los Angeles in the month of July. Since the transformer aging equations for F_{EQA} are non-linear, a moderate difference in the transformer charging energy makes a large difference in F_{EQA} . For example, in Los Angeles, the energy required from the grid to charge the 10 non-solar EVs on the simulated Wednesday is 168.5 kVAh, and the energy needed to charge the SEVs on the same day is 137.5 kVAh (full sun), 138.5 kVAh (average cloud), and 141.2 kVAh (average cloud with partial shading). Thus, the use of the SEVs has reduced grid energy charging needs by 18.4%, 17.8%, and 16.2% respectively. However, when considering the transformer F_{EQA} for the same day, the non-solar EV

transformer has $F_{EQA} = 35$ and the SEV transformer has $F_{EQA} = 19.3$ (full sun), $F_{EQA} = 19.4$ (average cloud), and $F_{EQA} = 19.6$ (average cloud with partial shading) which is about a 45% reduction in transformer aging using SEVs for this day. The peak transformer power for the case of SEVs is equal or 6.6 kW less than for the case of the non-solar EVs – thus, transformer aging is not solely dependent on peak power, but has a more complex relationship with the whole charging profile and associated heating. A moderate reduction in charging energy during peak load times of the day results in a significant reduction in transformer aging.

Depending on the variable temperatures throughout the year as shown in Fig. 3.6, the vehicle HVAC energy consumption varies from month to month, and the EV charging energy thus varies accordingly. Furthermore, the grid energy generated at the generator is about 12% higher than the distribution demand at the point of load due to transmission and distribution losses [7]. Fig. 3.22 shows the generated grid energy required to charge 150 EVs per month for the cases considered in Los Angeles and Detroit. It can be seen that the required grid charging energy is lowest in the winter months and highest in the summer months in Los Angeles. The reason is that the winters in Los Angeles are mild, and generally do not require cabin heating, whereas the summers are hot and will often require the use of cabin air conditioning. Conversely, in Detroit, the winter months have the highest EV charging loads due to the high energy consumption required to heat the cabin in cold ambient temperature. In spring and fall, vehicle energy consumption decreases due to milder temperatures not requiring any cabin HVAC, and then

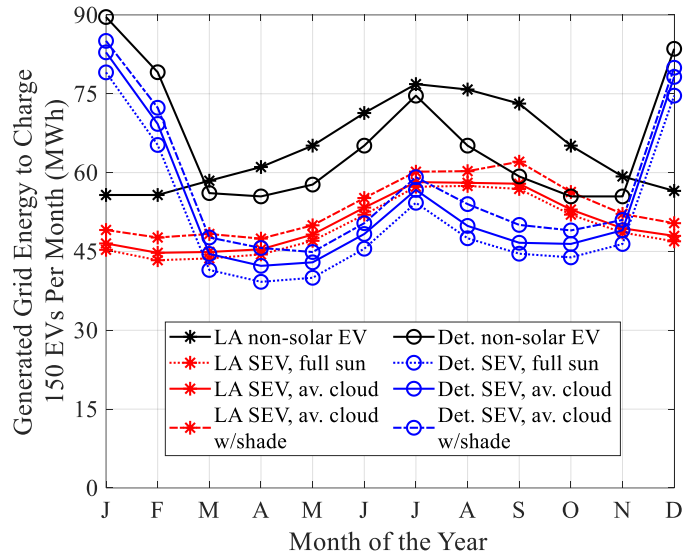


Fig. 3.22. Generated grid energy required to charge 150 EVs in each month of the year in Los Angeles and Detroit (CRA charging).

cabin air conditioning increases the energy use again in the summer, but to a lower value than the heating required in the winter. SEVs can reduce the energy generation demand in a sunny July month in Los Angeles by 25% and in Detroit by 27%, which is an important time for reducing energy use due to the otherwise peaking grid load. The annual average monthly generated grid energy required to charge 150 EVs is summarized in Fig. 3.23. In the presence of moderate partial shading, the average reduction in grid energy generation is 17.5% in Los Angeles and 13.5% in Detroit.

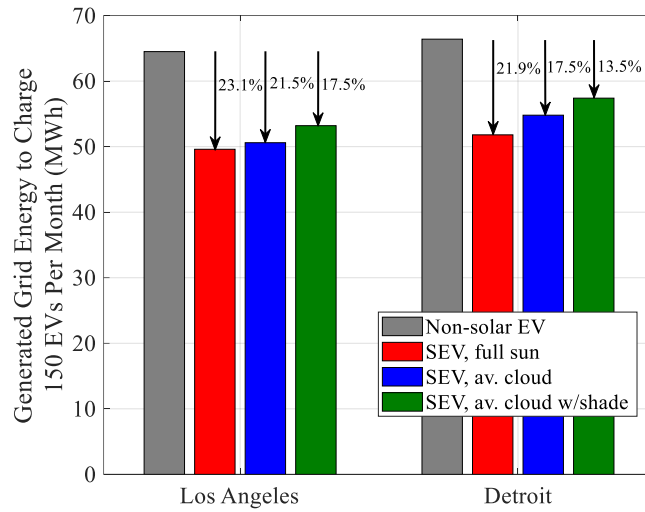


Fig. 3.23. Annual average monthly generated grid energy required to charge 150 EVs (CRA charging).

Based on the charging profiles for each day of the week, the equivalent aging factors, F_{EQA} , are calculated for each of the 15 transformers in each city and in each month of the year. The average monthly aging factors for all 15 transformers for 4 months for each EV penetration rate are shown in Fig. 3.24. Fig. 3.24 shows

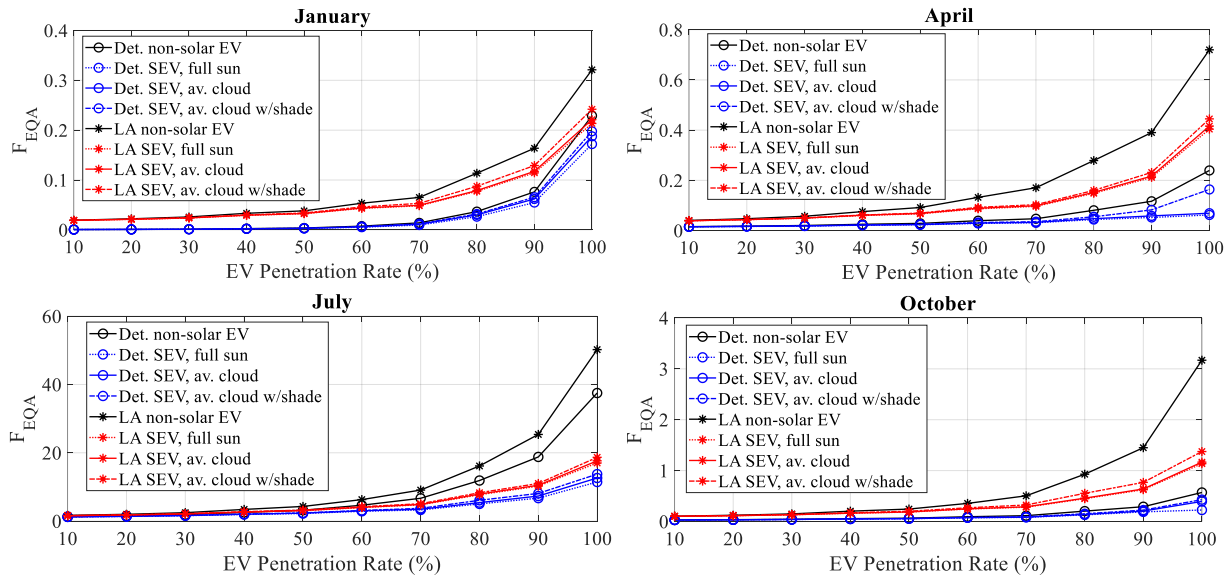


Fig. 3.24. Average monthly equivalent aging factors for non-solar EVs and SEVs in Detroit and Los Angeles (LA) (CRA charging).

that for non-solar EVs, the equivalent transformer aging factor is less than one for 100% EV penetration in the colder month of January, for both Los Angeles and Detroit. Thus, the cooler ambient temperatures are a larger factor in transformer aging than the high charging energy needed in the coldest months due to vehicle HVAC use. In the warmer months, SEVs offer significant improvement in transformer aging compared to the non-solar EV. To quantify the annual effect on transformer aging of SEVs, Fig. 3.25 shows the corresponding average annual aging factors. For moderate and high EV penetration rates, which can occur even

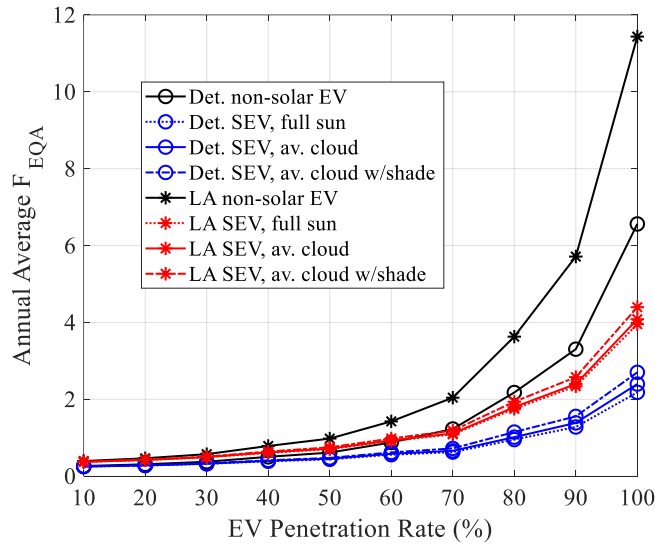


Fig. 3.25. Average annual equivalent aging factors for non-solar EVs and SEVs in Detroit and Los Angeles (LA) (CRA charging).

today in neighborhood clusters, the reduction in transformer aging from using SEVs is significant. For example, at 80% EV penetration, the proposed SEV concept would reduce transformer aging by around 50% in either city compared to the non-solar EV case, effectively doubling the lifetime of distribution transformers. Specifically, at 80% EV penetration, the Los Angeles annual F_{EQA} would reduce

from 3.6 to 1.8 (with standard deviation across the 15 transformers equal to 1.1), and the Detroit annual F_{EQA} would reduce from 2.2 to 1.0 (with standard deviation across the 15 transformers equal to 0.54).

While the preceding analysis assumes drivers charge their EVs immediately upon arriving home from their last trip of the day, it is well known that delaying EV charging events can reduce stress on distribution transformers by spreading out the EV load away from the hours of the peak household load [9]-[12],[36]. Many current EVs provide a *Charge By Departure* (CBD) charging option which allows drivers to set a standard daily departure time, and the vehicle calculates the overnight time that the vehicle must start charging to be fully charged by the programmed next-day departure time. This charging start time will vary day-to-day, and vehicle-to-vehicle, depending on the amount of energy needed by each vehicle on each night. The *CBD* strategy reduces transformer aging the most out of the currently-available in-vehicle options [36], without the need for grid sensors, smart agents, communication networks, connected and controllable EV chargers, or a method to obtain proprietary vehicle battery SOC data from a variety of EV models. Thus, the *CBD* charging strategy is studied here to analyze its effect compared to, and combined with, SEVs.

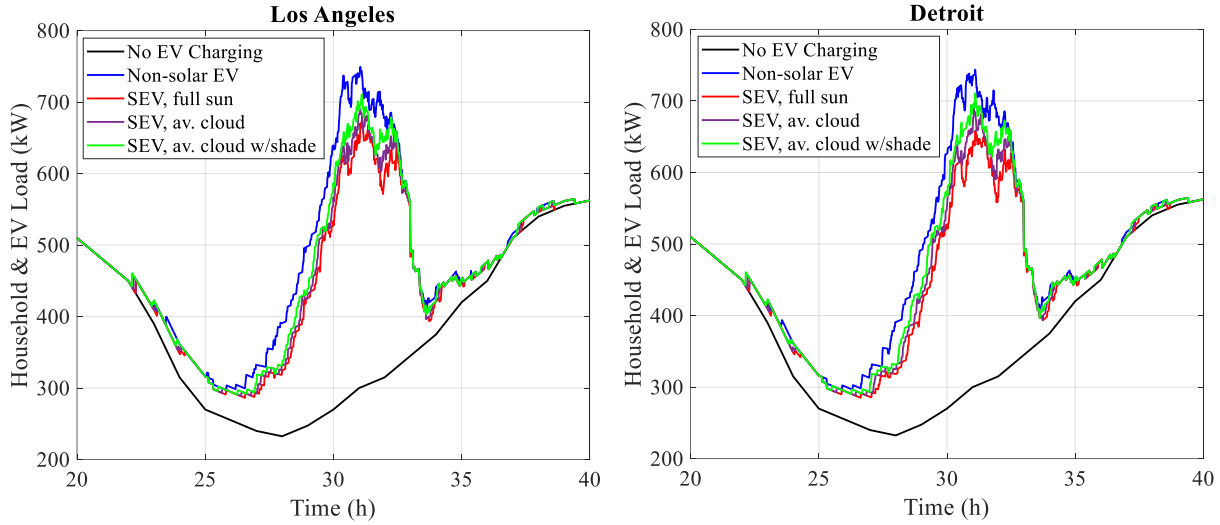


Fig. 3.26. Household and EV charging load for 150 EVs and 150 houses using CBD charging strategy.

Fig. 3.26 shows the household and EV charging load for 150 EVs and 150 homes using the *CBD* charging strategy on a Wednesday night in July. The amount of charging energy reduction from SEVs is the same as with the previous *CRA* approach, but the EV charging has been shifted to occur mainly overnight and in the early morning. This shift has a large beneficial effect on the associated transformer aging, as the EV load is more spread out, has a lower peak, and occurs during the cooler overnight and early morning hours. The resulting annual average F_{EQA} is shown in Fig. 3.27. *CBD* charging with non-solar EVs reduces transformer aging slightly more than the use of SEVs with *CRA* charging; for example, in Los Angeles at 80% EV penetration, $F_{EQA} = 3.6$ for *CRA* with non-solar EVs, $F_{EQA} = 1.8$ for *CRA* with SEVs, and $F_{EQA} = 1.2$ for *CBD* with non-solar EVs. The best case is to combine SEVs with *CBD* charging, which results in average $F_{EQA} = 0.83$ (with standard deviation 0.61 across the 15 transformers). In Detroit, SEVs combined with *CBD* charging reduced F_{EQA} to 0.53 (with standard deviation 0.38) at 80% EV

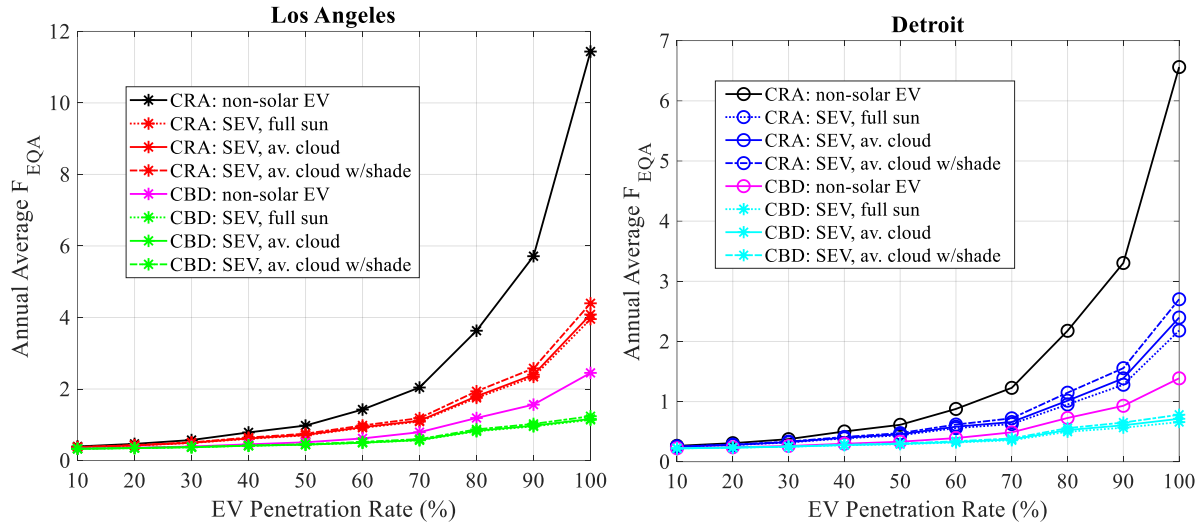


Fig. 3.27. Average annual equivalent aging factors for non-solar EVs and SEVs for CRA and CBD EV charging strategies.

penetration. While charging strategy selection is the personal choice of each driver, and is thus difficult to enforce, it is clear that SEVs can make a significant reduction in transformer aging with either charging strategy.

3.4.3 Driver Benefits

A driver driving a SEV or a user having the advantage of an autonomous SEV- the main benefits they both can obtain from SEVs are the range extension and reduced charging costs. Therefore, the word “Driver” would mean both a driver in case of a SEV and a user in case of an autonomous SEV in the rest of this thesis. Both of these driver benefits stem from an increase in vehicle efficiency in terms of driving distance possible per unit of grid energy charged from the plug. EV energy consumption is commonly expressed in terms of kWh/100km. In the case of SEVs, the solar energy gained over a day can be considered “free”, and thus a more useful measure of vehicle energy consumption is “grid kWh/100km”. Fig.

3.28 shows the grid kWh/100km results for non-solar and solar EVs in Los Angeles and Detroit, where the results are calculated using each driver's particular logged drive cycles. This means that these results account for the fact that if a driver does not leave home until late in the morning or in the afternoon, their vehicle will have

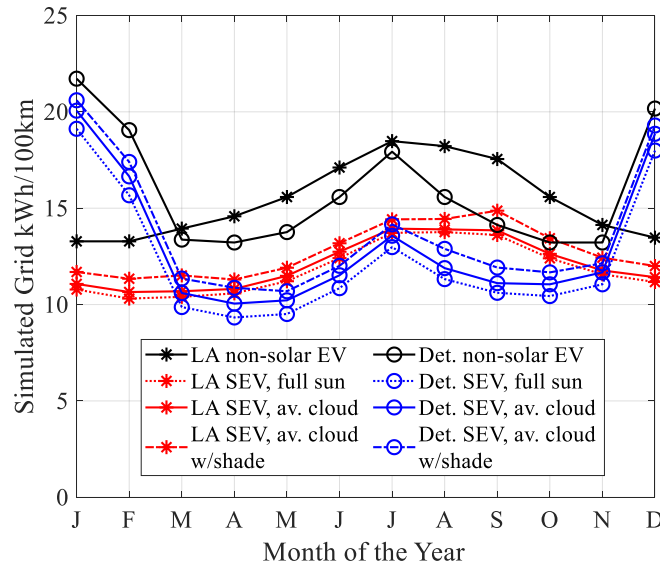


Fig. 3.28. Simulated average grid energy consumption in grid kWh/100km in Los Angeles and Detroit.

been unable to absorb solar charging energy until it begins driving (since in this study, each vehicle is assumed to be fully charged from the grid overnight).

Fig. 3.28 shows that in both cities, vehicle energy consumption is high in the summer months due to higher HVAC loads. Fortunately, the most solar energy is also available during these months, meaning the use of SEVs has a significant impact in these months. Fig. 3.29 summarizes the annual average grid kWh/100km. The percentage charging reduction is, as expected, the same as the grid generated energy reductions in Fig. 3.23. The interesting perspective for the driver is to benefit from essentially a more efficient vehicle. For example, in Los Angeles, the

annual energy consumption drops from 15.4 kWh/100km for a non-solar EV to 12.7 kWh/100km for a SEV with average cloud conditions with partial shading, or

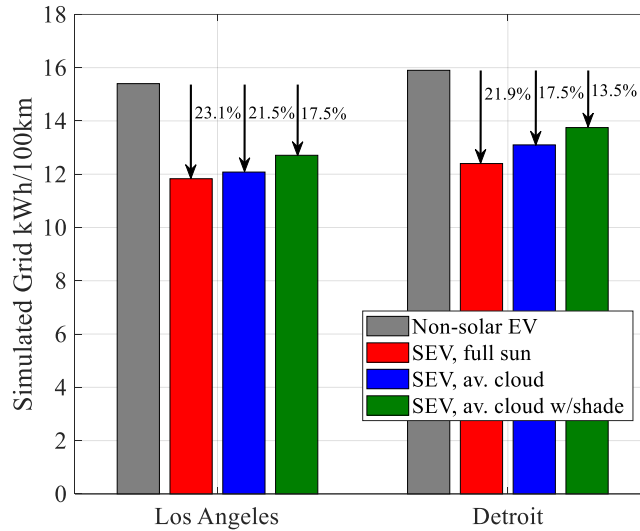


Fig. 3.29. Simulated annual average grid energy consumption in grid kWh/100km.

equivalently, fuel economy rises from 136 MPGe to 165 MPGe.

The gained solar energy allows for range extension during the day's drive, given the fixed amount of grid energy from the plug from the previous overnight charging session. For the range extension analysis only, it is assumed that the driver leaves in the morning so that full solar energy can be captured during the day, in order to find the upper bound of range extension in each month. Range extension will vary by month because of varying solar radiation, and also because the vehicle energy consumption varies by month due to varying HVAC loads. Thus, daily solar range extension is calculated per month using (16), where the units are shown in square brackets. $FC_{non-solarEV}$ is the fuel consumption of the non-solar EV as shown in Fig. 3.28, and E_{solar} is the total daily solar energy available to the EV battery each

day, after considering temperature-dependent PV cell efficiency (20% nominal) from Fig. 3.12 and the 94% power electronic converter efficiency. The average

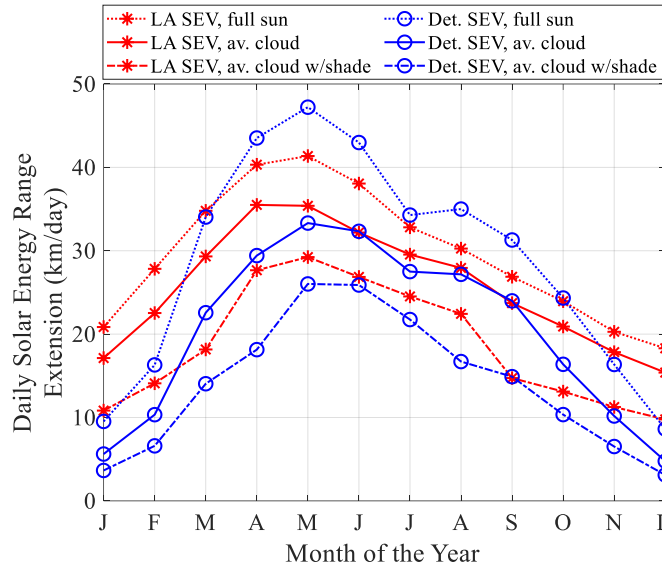


Fig. 3.30. Daily solar energy range extension in Los Angeles and Detroit.

daily per-driver solar range extension results are shown in Fig. 3.30.

$$\text{Solar Range Extension} \left[\frac{\text{km}}{\text{day}} \right] = \frac{E_{\text{solar}} \left[\frac{\text{kWh}}{\text{day}} \right]}{FC_{\text{non-solarEV}} \left[\frac{\text{kWh}}{100\text{km}} \right]} \times 100 \quad (16)$$

The solar range extension in Los Angeles is highest in April, May, and June because a significant amount of solar radiation is available and the base EV energy consumption is low since air conditioning use is not yet high. Though more solar radiation is available in July and August, the solar range extension is lower because the vehicle is using more energy due to higher air conditioning use. In average cloud conditions, all the months of the year give a solar range extension of at least 15 km in Los Angeles. Interestingly, the maximum solar range extension of either city

occurs in Detroit in May, and the extensions in April and June are also higher than even the peak solar range extension in Los Angeles. The reason is that in the spring months, Detroit has high solar radiation, but moderate temperatures, meaning HVAC use is low or zero. Since the vehicle is obtaining large amounts of extra solar energy, but also driving in a very efficient way due to low HVAC use, the solar range extension is highest at this time. In average cloud conditions, 8 months of the year give a solar range extension of at least 15 km in Detroit. On an annual average, the daily solar range extensions for Los Angeles are 30 km for full sun, 26 km for average cloud conditions, and 19 km for average cloud conditions with partial shading. On an annual average, the daily solar range extensions for Detroit are 29 km for full sun, 20 km for average cloud conditions, and 14 km for average cloud conditions with partial shading.

The second driver benefit of SEVs is charging cost reduction. Time-of-Use (TOU) electricity billing has been assumed for all drivers in each state. In Los Angeles, there are three TOU billing rates: *base*, *low-peak*, and *high-peak*. In Detroit, there are two TOU billing rates known as *off-peak* and *on-peak*. Table 3.1 summarizes the TOU billing rates across all months in both Los Angeles and Detroit [73] [74].

EV charging cost is calculated using (17):

$$\text{Charging Cost} = E_{TOU1}C_{TOU1} + E_{TOU2}C_{TOU2} + E_{TOU3}C_{TOU3} \quad (17)$$

Table 3.1. Electricity Price Rate In LA & Detroit [73] [74]

Month	Los Angeles Consumption Charge (USD/kWh)			Detroit Consumption Charge (USD/kWh)	
	Base M-F 8pm- 10am, Sat, Sun	Low-peak M-F 10am- 1pm & 5pm- 8pm	High-peak M-F 1pm- 5pm	Off-peak M-F 7pm- 7am, Sat, Sun	On-peak M-F 7am-7pm
January - March	0.17051	0.17405	0.17405	0.05818	0.27710
April – May	0.17463	0.17817	0.17817	0.05818	0.27710
June	0.17073	0.19446	0.25657	0.05818	0.27710
July - September	0.17542	0.20286	0.26126	0.05818	0.27710
October - December	0.16788	0.17142	0.17142	0.05818	0.27710

where E_{TOU1} is the energy consumed in kWh by the charging vehicles in the first TOU category (i.e., base rate for Los Angeles), C_{TOU1} is the \$/kWh cost for the first TOU category as per Table 3.1, and subscripts 1, 2, 3 refer to each TOU category (with only two categories used for Detroit). Taxes of the respective cities are then added to this consumption charge (10% for Los Angeles [75] and 4% for Detroit [76]). Fig. 3.31 shows the monthly EV charging cost savings per driver for using SEVs in place of non-solar EVs. Summer months provide the highest cost savings for SEVs because there is higher solar incident energy. For days with average cloud conditions, the annual projected charging cost savings are \$182 in Los Angeles and \$73 in Detroit, which are 21.6% and 19.3% of total EV charging costs respectively, as shown in Fig. 3.32.

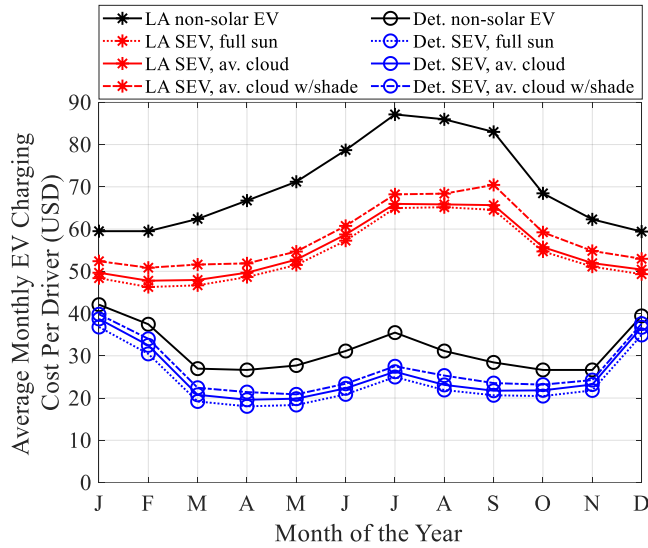


Fig. 3.31. SEV effect on monthly EV charging costs per driver in Los Angeles and Detroit.

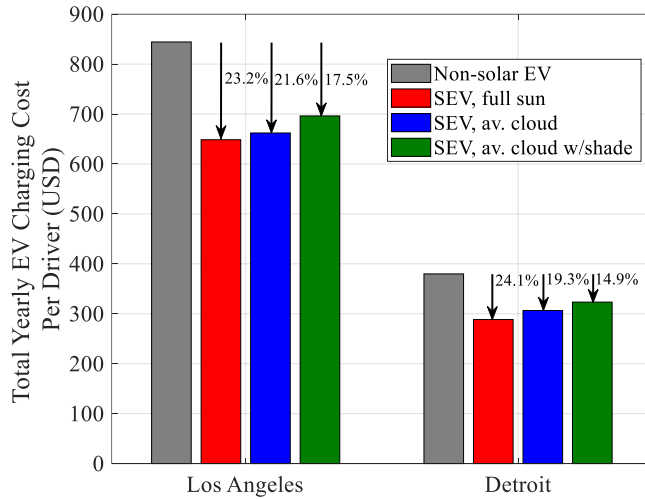


Fig. 3.32. SEV effect on annual EV charging costs per driver.

3.4.4 Environmental Benefits

The main environmental benefit of widespread SEV use is a reduction in electricity-related emissions due to the displacement of grid charging with on-board solar charging. This analysis quantifies the reduction in CO₂ emissions specifically, as it is a prevalent greenhouse gas. The carbon intensity for the current grid mix in California is 215 kg/MWh, and the carbon intensity in Michigan is currently 520 kg/MWh [77]. California has a much lower carbon intensity than Michigan because its grid mix consists of 37% natural gas and 63% non-emitting sources (nuclear, hydroelectric, solar, and wind), whereas the Michigan grid is powered by 37% coal and 27% natural gas, with non-emitting sources providing the other 36% [78]. Fig. 3.33 shows the amount of CO₂ produced monthly to meet the charging demand of 150 EVs for the non-solar EV and SEV cases in Los Angeles and Detroit. Fig. 3.34 shows the comparison of annual CO₂ production in both the cities to charge 150 non-solar EVs and 150 SEVs in case of full sun, average cloud conditions, and average cloud conditions with partial shading. Annually, the use of SEVs instead of non-solar EVs would reduce CO₂ emissions approximately by 239 kg per driver in California (21.5%) and by 484 kg per driver in Detroit (17.5%) considering average cloud conditions throughout the whole year. California currently has about 500,000 EVs on the road [79]. If SEV emission reductions are projected across this fleet, the annual CO₂ reduction for this state is 119,500 tonnes.

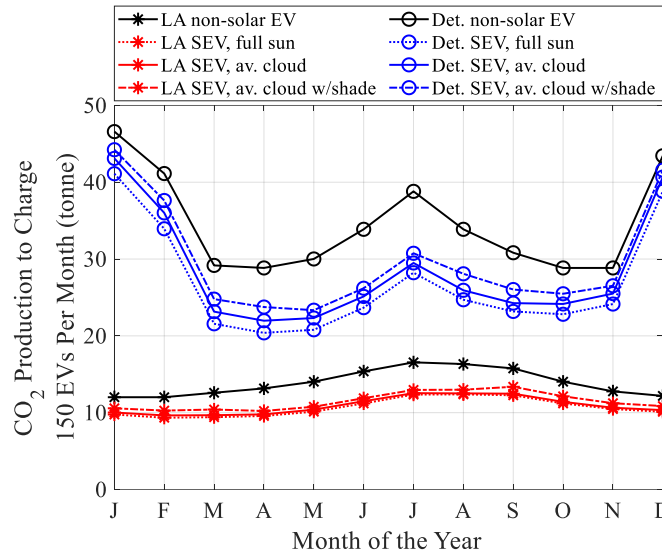


Fig. 3.33. CO₂ production to charge 150 EVs monthly in Los Angeles and Detroit.

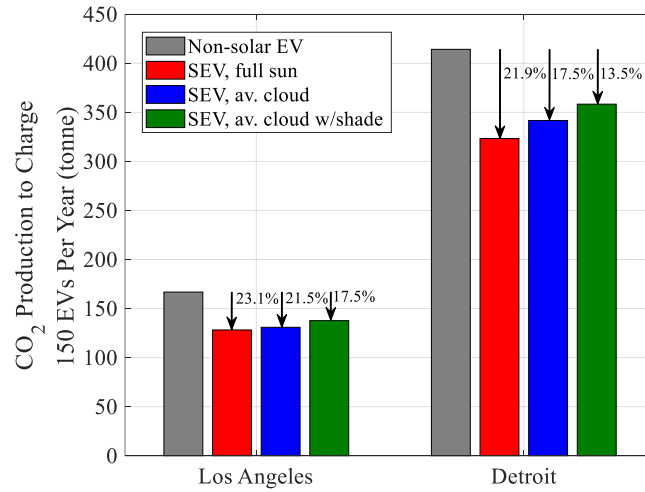


Fig. 3.34. Annual CO₂ production to charge 150 EVs.

3.4.5 Economic Analysis

The cost of PV integration is a crucial factor in the viability of the SEV concept. Utility-scale PV costs are useful for these estimates, where silicon module costs have fallen to <\$0.25/W [80] with installed costs <\$0.89/W [81]. Cell and

module costs have fallen for decades due to the experience curve and this trend is expected to continue for some time. Full integration of the cell manufacture brings the installation costs into a highly automated vehicle manufacturing environment, with opportunities for significant cost reduction as compared to highly labor-intensive PV installation. Furthermore, the energy intensive racking components for PV installation are not required. From this point of view, the manufactured cost of PV for SEVs could be reduced well below the installed cost for utility-scale PV. This study conservatively estimates the PV cell and integration costs to be \$1.00/W, based on an estimated CIGS cell cost of \$0.50/W [21] and an additional \$0.50/W for the PV integration with the automotive steel, totaling \$620 for a 620 W peak power system. While this delineation is artificial in an integrated process, the latter cost recognizes the process development and infrastructure updates with respect to the conventional automotive manufacturing process. For this SEV application, the PV balance of system costs are from the DC/DC converters required to control and step-up the solar power. The DOE has set a target of \$50/kW in 2020 for automotive-grade DC/DC converters [82]. Thus, this study estimates the cost of a 620 W DC/DC converter at \$31 plus \$19 for wiring, for a total of \$50. This brings the total mass-produced cost premium for a SEV to \$670, which is on par or less than many other options offered on new vehicles. These rough cost estimates are predicated upon achieving the full benefits of a fully integrated process implemented *at scale*.

By considering only the driver's charging costs, the payback period for the driver assuming a \$670 premium for the SEV is 3.7 years in Los Angeles and 9.2 years in Detroit. However, these metrics do not fully capture the other SEV benefits, such as driving range extension, reduction in CO₂ emissions, and benefits to the grid. This fact highlights one current difficulty in moving towards mass-produced SEVs: the benefits are widespread across numerous players, so motivation for investment by single parties, such as vehicle manufacturers, is not yet high. This is analogous to the high current payback periods for drivers considering EVs compared to ICE vehicles – the environmental benefits add additional purchase incentive beyond traditional payback periods.

3.5. SEV Future Trends

This chapter has focused on analyzing system-level SEV benefits for a typical passenger vehicle under the standard one-driver model. Future SEV applications could also include autonomous and ride-sharing EVs. For a fully autonomous EV, the vehicle auxiliary electrical load is expected to increase by a few kilowatts for powering sensors and additional on-board computers [83]. This additional load would increase EV charging power needs and reduce driving range. For a one-driver autonomous vehicle, low-cost integrated PV cells are an attractive option because the harvested solar power could help offset the increased energy consumption of the vehicle compared to a baseline EV. Ride-sharing of a non-autonomous vehicle would change the drive cycle dramatically such that the vehicle would likely drive for much more time in the day compared to the one-driver data

used in this analysis. This could increase the vehicle energy expenditure significantly over a 24-hour period, with a potential for near-constant driving conditions. For a ride-sharing SEV, even though the solar energy captured would be equal to that in a one-driver SEV, the percentage of SEV energy use reduction (and the associated benefits) would be smaller due to the larger energy expenditure. Overall, autonomous vehicles and ride-sharing models increase vehicle energy use – SEVs can play an important role in partially mitigating these increases, though the percentage of SEV benefits will reduce with larger and larger vehicle energy consumption requirements.

There has been recent industry interest in using thin-film solar panels on Class 8 tractors and trailers [84]. For both diesel and electric tractors, the energy savings percentage from using on-board solar is small due to the large size and mass of the truck, and the fact that it can drive for the majority of the day, leading to enormous daily energy needs. However, on-board solar can help with idle reduction and jump-start reduction (from drained batteries) by powering electrical loads like trailer refrigerators, lift-gates, and HVAC. This use of on-board solar with diesel trucks can increase driver convenience and extend battery life.

SEVs also present the opportunity to use EVs as decentralized solar generation systems if a bidirectional on-board charger is included in the vehicle. Much prior work has focused on the design and control of bidirectional on-board chargers for EVs for the purpose of providing power from the EV battery to the grid for V2G functionality [85-88], but no work has considered its use in solar-charged EVs.

Bidirectional chargers are more expensive than unidirectional chargers because switches must be used in place of the AC/DC rectifying diodes. A further difficulty is that the control complexity is increased. For the proposed SEV concept with a bidirectional on-board charger, vehicles fully charged overnight and at home for part or all of the following day could power the house, reducing electricity costs and acting as a decentralized solar generation system with built-in energy storage. The benefit would depend on the amount of time the vehicle is parked at home while fully-charged, which would change driver-to-driver.

To quantify the potential benefit, an additional analysis was run on the 150 unique drivers using a 94% efficient bidirectional on-board charger, where a fully charged SEV provides power to the house before the first departure of the day. In this case, the annual projected net charging cost savings are \$218 in Los Angeles and \$99 in Detroit, which are 25.8% and 26.0% respectively of the total charging costs. Though the amount of energy gained by the home is relatively small, the high TOU electricity prices in the daytime mean a reasonable benefit is achieved, on average. Of course, for drivers who regularly leave early in the morning, the benefit of bidirectional power flow would be negligible, and for drivers who regularly leave later in the day, the benefit would be significant. An error analysis shows that across the 150 drivers, the standard deviation of total charging cost savings in Los Angeles is \$56.50 and, in Detroit, \$37.60 with the availability of SEV2G feature. To analyze the economic feasibility, the approximate cost increase of a bidirectional on-board charger compared to a unidirectional on-board charger is calculated as follows:

Infineon switches IPW65R080CFDA (\$10.78 each) are assumed to replace 8 diodes (IDFW40E65D1E at \$5.55 each) in an on-board charger, 100% of the switch cost is added for gate drivers and thermal management of the switches, and the total cost difference is halved to account for the large purchasing volumes of the automotive sector. The resulting hardware cost increase is \$64 per charger, meaning the average payback period in Los Angeles is 3.5 months and in Detroit, 7.8 months, for the bidirectional charger. This does not account for the extra initial development costs of the bidirectional on-board charger. Overall, this analysis shows that adding a bidirectional charger to a SEV to further reduce net charging costs reduces the total payback period (3.4 years in Los Angeles and 7.4 years in Detroit).

When considering the environmental benefits, a bidirectional solar power V2G feature would reduce the total annual CO₂ emissions by 290 kg per driver in Los Angeles (standard deviation 70.6 kg across 150 drivers) and by 563 kg per driver in Detroit (standard deviation 129.5 kg across 150 drivers), compared to non-solar EVs. This V2G concept can be further extended to a smarter SEV2G energy management system. With the usual V2G framework, a vehicle discharges its battery to provide services to the grid – this involves a trade-off between battery energy needed by the driver and the value of the energy provided to the grid. For a SEV, this trade-off changes because the vehicle is a mobile solar energy generating station, and thus could be more able to exchange power with the grid with minimal

impact to the driver. Thus, future research on reducing the cost and complexity of bidirectional on-board chargers would be valuable to SEVs.

Though the fully-integrated SEV concept proposed here has been shown to have promising benefits on a system level, there are numerous practical challenges to be considered in the future. Firstly, one concern is how to deal with automobile accidents which damage one or more of the solar body panels. For damaged body panels, it is currently common for whole panels to be replaced with new panels from the vehicle manufacturer. For the SEV case, the difference would be that the new panel with integrated solar cells would be slightly more expensive than the non-solar panel. However, if the mass production of solar cells integrated onto the steel is able to reduce costs to a reasonable level for whole vehicle purchase, then the cost of a solar replacement panel could similarly be in a reasonable range.

Secondly, there will be a challenge of developing a marketing strategy for SEVs. The environmentally-friendly aspect of SEVs will be important, just as people buy EVs today that cost more than their ICE counterparts, often for environmental reasons. The aesthetics of a SEV may also be a marketing challenge, but there is potential to turn it around as a positive point if the SEV can be made a desirable status symbol – this is similar to the Tesla EV marketing strategy. Furthermore, SEVs will be less suitable, and less popular for drivers that routinely park indoors during the day, and may be less desirable to drivers living in more northern and/or cloudy cities – this will affect the marketing plan and business model.

Thirdly, since the proposed SEV concept includes many critical parts from different fields, it is important that the cross-functional team working on its production perform a Failure Mode Effects Analysis (FMEA) to identify potential failures in a wide range of areas, including solar-steel integration, PV durability in harsh weather and over time, and power electronic converter reliability. Finally, a major challenge is the investment needed to develop the process to integrate the PV directly onto the steel, including smooth adhesion over curved surfaces and durability concerns over many years of use in potentially harsh weather. As described in this chapter, many parties can benefit from SEVs, but one party must ultimately become motivated enough to invest in this integration process.

3.6. Conclusions

The big-picture benefits of SEVs have not yet been realized because the thinking has been small (vehicle rooftop panels) and limited in scope (considering only driver benefit). This study has modeled the effect of panel tilt, vehicle direction, and partial shading on solar generation, and has shown that the proposed low-cost SEV concept offers real benefits to the grid, the driver, and the environment, indicating that further research is warranted to address the design and manufacturing challenges of SEVs. For the given dataset of 150 drivers over one week, the use of SEVs (compared to non-solar EVs) would reduce the annual net vehicle energy consumption by 21.5% in Los Angeles and by 17.5% in Detroit under average cloud conditions, and including temperature-dependent PV efficiency. The peak solar range extension is 47 km/day in Detroit on a sunny day

in May and charging costs are reduced by about 20% for average cloud conditions. Though each benefit is useful alone, the real potential of SEVs is clear when considering the combination of these results together. Thus, a low-cost SEV has the potential to empower a massive transition to solar power on a distributed scale of individual car owners.

Chapter 3 References

- [1] W.-J. Guan, X.-Y. Zheng, K. F. Chung, and N.-S. Zhong, “Impact of air pollution on the burden of chronic respiratory diseases in China: time for urgent action,” *The Lancet*, vol. 388, no. 10054, pp. 1939–1951, 2016.
- [2] R. Irle, “Global EV Sales for 2018 – Final Results”, *EV Volumes*, www.ev-volumes.com/country/total-world-plug-in-vehicle-volumes [Accessed April 2020]
- [3] K. Yoshikawa, H. W. Yoshida, et al. “Silicon heterojunction solar cell with interdigitated back contacts for a photoconversion efficiency over 26%”, *Nature Energy*, 2017;2(5):17032.
- [4] P.T. Chiu, D.L. Law, R.L. Woo, et al. “35.8% space and 38.8% terrestrial 5J direct bonded cells,” in *Proc. 40th IEEE Photovoltaic Specialist Conference*, Denver, pp. 11–13, June 2014.
- [5] J. Wu, Y. Hirai, T. Kato, H. Sugimotor, V. Burmudez, “New world record efficiency up to 22.9% for Cu (In,Ga)(Se,S)₂ thin-film solar cell,” *7th World Conference on Photovoltaic Energy Conversion (WCPEC-7)*, June 10–15, 2018, Waikoloa, HI, USA.
- [6] Energyhub.org, “Cost of solar power in Canada 2019”, <https://energyhub.org/cost-solar-power-canada/> [Accessed April 2020]
- [7] A. Nourai, V. Kogan, and C. Schafer, “Load leveling reduces T&D line losses,” *IEEE Transactions on Power Delivery*, vol. 23, no. 4, pp. 2168–2173, Oct. 2008.
- [8] Q. Gong, S. Midlam-Mohler, V. Marano, and G. Rizzoni, “Study of PEV charging on residential distribution transformer life,” *IEEE Trans. on Smart Grid*, vol. 3, no. 1, pp. 404–412, March 2012.
- [9] Q. Gong, S. Midlam-Mohler, E. Serra, V. Marano, and G. Rizzoni, “PEV charging control considering transformer life and experimental validation of a 25 kVA distribution transformer,” *IEEE Trans. on Smart Grid*, vol. 6, no. 2, pp. 648–656, March 2015.
- [10] J. Quirós-Tortós, L. Ochoa, S. Alnaser, and T. Butler, “Control of EV charging points for thermal and voltage management of LV networks,” *IEEE Trans. on Power Systems*, vol. 31, no. 4, pp. 3028–3039, July 2016.
- [11] M. Gray and W. Morsi, “Power quality assessment in distribution systems embedded with plug-in hybrid and battery electric vehicles,” *IEEE Trans. on Power Systems*, vol. 30, no. 2, pp. 663–671, March 2015.

- [12] M. ElNozahy and M. Salama, “A comprehensive study of the impacts of PHEVs on residential distribution networks,” *IEEE Trans. on Sustainable Energy*, vol. 5, no. 1, pp. 332–342, Jan. 2014.
- [13] M. S. ElNozahy and M. M. A. Salama, “Studying the feasibility of charging plug-in hybrid electric vehicles using photovoltaic electricity in residential distribution systems,” *Elect. Power Syst. Res.*, vol. 110, pp. 133–143, May 2014.
- [14] F. M. Uriarte, A. Toliyat, A. Kwasinski, and R. E. Hebner, “Consumer data approach to assess the effect of residential grid-tied photovoltaic systems and electric vehicles on distribution transformers,” in *Proc. IEEE 5th Int. Symp. Power Electron. Distrib. Gener. Syst. (PEDG)*, Galway, Ireland, pp. 1–8, June 2014.
- [15] T. J. Geiles and S. Islam, “Impact of PEV charging and rooftop PV penetration on distribution transformer life,” in *Proc. IEEE Power Energy Soc. Gen. Meeting*, Vancouver, BC, Canada, pp. 1–5, July 2013.
- [16] S. Abdelsamad, W. Morsi, and T. Sidhu, “Probabilistic impact of transportation electrification on the loss-of-life of distribution transformers in the presence of rooftop solar photovoltaic,” *IEEE Trans. on Sustainable Energy*, vol. 6, no. 4, pp. 1565–1573, Oct 2015.
- [17] S. El-Bataway and W. Morsi, “Distribution transformer’s loss of life considering residential prosumers owning solar shingles, high-power fast chargers and second-generation battery energy storage,” *IEEE Trans. on Industrial Informatics*, vol. 15, no. 3, pp. 1287–1297, March 2019.
- [18] R. Wuerz, A. Eicke, F. Kessler, et al. “CIGS thin-film solar cells and modules on enameled steel substrates,” *Solar Energy Materials & Solar Cells*, 100, pp. 132–137, 2012.
- [19] M. Nakamura, K. Yamaguchi, Y. Kimoto, Y. Yasaki, T. Kato, and H. Sugimoto, “Cd-free Cu (In,Ga)(Se,S)₂ thin-film solar cell with a new world record efficacy of 23.35%,” in *Proc. 46th IEEE Photovoltaic Specialists Conference (PVSC 46)*, Chicago, IL, June 19, 2019.
- [20] Online: www.solar-frontier.com/eng/news/2019/0117_press.html [Accessed April 2020]
- [21] K. Horowitz, R. Fu, X. Sun, T. Silverman, M. Woodhouse, and M. Alam, “An analysis of the cost and performance of photovoltaic systems as a function of module area,” *National Renewable Energy Laboratory (NREL), U.S. Department of Energy*, Technical Report NREL/TP-6A20-67006, April 2017.
- [22] Panasonic, “Panasonic’s photovoltaic module HIT adopted for Toyota Motor’s new Prius PHV,” Available online:

- <https://news.panasonic.com/global/press/data/2017/02/en170228-3/en170228-3.html> [Accessed April 2020]
- [23] Online: <https://karmaautomotive.com/> [Accessed April 2020]
- [24] Online:
<https://www.engineering.com/ElectronicsDesign/ElectronicsDesignArticles/ArticleID/15611/2020-Vision-Audi-Electric-Vehicles-Go-Solar.aspx>
[Accessed April 2020]
- [25] Online: <https://sonomotors.com> [Accessed April 2020]
- [26] C. Duan, C. Wang, Z. Li, J. Chen, S. Wang, A. Snyder, and C. Jiang, “A solar power-assisted battery balancing system for electric vehicles”, *IEEE Transactions on Transportation Electrification*, vol. 4, no. 2, pp. 432-443, June 2018.
- [27] M. Grosso, D. Lena, A. Bocca, A. Macii, and S. Rinaudo, “Energy-efficient battery charging in electric vehicles with solar panels”, *2016 IEEE 2nd International Forum on Research and Technologies for Society and Industry Leveraging a Better Tomorrow (RTSI)*, pp. 1-5, 2016.
- [28] C. Ding, H. Li, W. Zheng, and Y. Wang, “Reconfigurable photovoltaic systems for electric vehicles,” *IEEE Design & Test*, pp. 37-43, Nov./Dec. 2018.
- [29] M. Abdelhamid, I. Haque, S. Pilla, Z. Filipi et al., “Impacts of adding photovoltaic solar system on-board to internal combustion engine vehicles towards meeting 2025 fuel economy CAFÉ standards,” *SAE Int. J. Alt. Power*. 5(2):237-248, 2016.
- [30] P. Mulhall, S. Lukic, S. Wirasingha, Y. Lee, and A. Emadi, “Solar-assisted electric auto rickshaw three-wheeler,” *IEEE Transactions on Vehicular Technology*, vol. 59, no. 5, pp. 2298-2307, June 2010.
- [31] A. Diab-Marzouk and O. Trescases, “SiC-based bidirectional Cuk converter with differential power processing and MPPT for a solar powered aircraft,” *IEEE Transactions on Transportation Electrification*, vol. 1, no. 4, pp. 369-381, Dec. 2015.
- [32] C. Gan, N. Jin, Q. Sun, W. Kong, Y. Hu, and L. Tolbert, “Multiport bidirectional SRM drives for solar-assisted hybrid electric bus powertrain with flexible driving and self-charging functions,” *IEEE Transactions on Power Electronics*, vol. 33, no. 10, pp 8231-8245, Oct. 2018.
- [33] S. Debnath, A. Foote, O. Onar, “Grid impact studies from dynamic wireless charging in smart automated highways,” in *Proc. 2018 IEEE Transportation*

- Electrification Conference and Exp (ITEC)*, Long Beach, CA, June 13–15, 2018.
- [34] C. Ou, H. Liang, W. Zhuang, “Investigating wireless charging and mobility of electric vehicles on electricity market,” *IEEE Transactions on Industrial Electronics*, vol. 62 no. 5, pp. 3123–3133, 2015.
- [35] M. H. Mobarak, R. Kleiman, and J. Bauman, “Investigation of grid benefits from a solar-powered electric vehicle using real-world driving data,” *IEEE Transportation Electrification Conference (ITEC)*, Detroit, MI, June 19-21, 2019.
- [36] M. H. Mobarak, and J. Bauman, “Vehicle-Directed Smart Charging Strategies to Mitigate the Effect of Long-Range EV Charging on Distribution Transformer Aging,” *IEEE Transactions on Transportation Electrification*, vol. 5, no. 4, pp 1097-1111, Dec. 2019.
- [37] D. Parker, “Research highlights from a large scale residential monitoring study in a hot climate.” *Proceeding of International Symposium on Highly Efficient Use of Energy and Reduction of its Environmental Impact*, pp. 108-116, Japan Society for the Promotion of Science Research for the Future Program, JPS-RFTF97P01002, Osaka, Japan, Jan. 2002. Available online: <http://www.fsec.ucf.edu/en/publications/html/FSEC-PF-369-02/> [Accessed April 2020]
- [38] *Transformers Committee of the IEEE Power Engineering Society*, IEEE Std C57.91-2011, 2011, IEEE Guide for Loading Mineral-Oil-Immersed Transformers, IEEE.
- [39] Whitby Hydro Energy Services Corp., “Power Factor Correction at the Residential Level – Pilot Project: Report to the LDC Tomorrow Fund,” September 12, 2005.
- [40] Available online: https://rredc.nrel.gov/solar/old_data/nsrdb/ [Accessed April 2020]
- [41] Available online: <https://www.wunderground.com/history/> [Accessed April 2020]
- [42] P. Palcu and J. Bauman, “Whole-Day Driving Prediction Control Strategy: Analysis on Real-World Drive Cycles,” *IEEE Trans. on Transportation Electrification*, vol. 4, no. 1, pp. 172-183, March 2018
- [43] M. H. Mobarak, R. N. Kleiman and J. Bauman, "Solar-Charged Electric Vehicles: A Comprehensive Analysis of Grid, Driver, and Environmental Benefits," *IEEE Trans. Transp. Elec.*, vol. 7, no. 2, pp. 579-603, June 2021.

- [44] F. Kasten, and A. T. Young, “Revised optical air mass tables and approximation formula”, *Applied Optics*, vol. 28, pp. 4735–4738, 1989.
- [45] A. B. Meinel, and M. P. Meinel, *Applied Solar Energy*, Addison Wesley Publishing Co., 1976.
- [46] L. Zortea, S. Nishiwakia, T. P. Weiss, S. Haass, J. Perrenoud, L. Greutera, T. Feurera, G. Palaniswamy, S. Buechelera, and A. N. Tiwaria, “Cu(In,Ga)Se₂ solar cells on low cost mild steel substrates,” *Solar Energy*, vol. 175, pp. 25–30, 2018.
- [47] Access to European Union Law, “Directive 2000/53/EC of the European Parliament and of the Council of 18 September 2000 on end-of life vehicles.”
- [48] H. Sugimoto, “High efficiency and large volume production of CIS-based modules,” in *Proc. 40th IEEE Photovoltaic Specialists Conference*, Denver, June 2014.
- [49] A. Virtuani, D. Pavanello, and G. Friesen, "Overview of Temperature Coefficients of Different Thin Film Photovoltaic Technologies", *25th European Photovoltaic Solar Energy Conference and Exhibition / 5th World Conference on Photovoltaic Energy Conversion*, 6-10 September 2010, Valencia, Spain.
- [50] R.G. Ross, “Flat-Plate Photovoltaic Array Design Optimization,” *14th IEEE Photovoltaic Specialists Conference*, San Diego, CA, pp. 1126-1132, 1980. Available online: <https://www.pveducation.org/pvcdrom/modules-and-arrays/nominal-operating-cell-temperature> [Accessed April 2020]
- [51] Life Cycle Inventories and Life Cycle Assessments of Photovoltaic Systems, IEA PVPS Task 12, Subtask 2.0, LCA Report IEA-PVPS 12-04:2015, January 2015.
- [52] L. Grandell, and M. Höök, “Assessing Rare Metal Availability Challenges for Solar Energy Technologies,” *Sustainability*, vol. 7, pp. 11818-11837, 2015.
- [53] Online: <http://www.pvcycle.org/> [Accessed April 2020]
- [54] Online: <http://eur-lex.europa.eu/LexUriServ/LexUriServ.do?uri=OJ:L:2012:197:0038:0071:EN:PDF> [Accessed April 2020]
- [55] Online: <https://eur-lex.europa.eu/legal-content/EN/TXT/PDF/?uri=CELEX:02000L0053-20130611&qid=1405610569066&from=EN> [Accessed April 2020]
- [56] N.C. McDonald, and J. M. Pearce, “Producer Responsibility and Recycling Solar Photovoltaic Modules”, *Energy Policy*, vol. 38, pp. 7041-7047, 2010.

- [57] D. J. Coyle, H. A. Blaydes, R. S. Northey, J. E. Pickett, K. R. Nagarkar, Ri-An Zhao, and J. O. Gardner, “Life prediction for CIGS solar modules part 2: degradation kinetics, accelerated testing, and encapsulant effects,” *Prog. Photovolt: Res. Appl.*, 2011.
- [58] M.J. de Wild-Scholten, “Energy Payback Time and Carbon Footprint of Commercial Photovoltaic Systems,” *Solar Energy Materials & Solar Cells*, vol. 119, pp. 296–305, 2013.
- [59] Y. Wang, T. Wu, and Y. Chueh, “A Critical Review on Flexible Cu(In, Ga)Se₂ (CIGS) Solar Cells,” *Materials Chemistry and Physics*, vol. 234, pp. 329–344, 2019.
- [60] S. Fafard, F. Proulx, M. C. A. York, L. S. Richard, P. O. Provost, R. Arès, V. Aimez, and D. P. Masson, “High-photovoltage GaAs vertical epitaxial monolithic heterostructures with 20 thin p/n junctions and a conversion efficiency of 60%,” *Appl. Phys. Lett.*, vol. 109, pp. 131107, 2016.
- [61] Online: <http://miasole.com/miasole-achieves-flexible-substrate-thin-film-solar-cell-efficiency-of-20-56-percent/> [Accessed April 2020]
- [62] R. Wuerz, A. Eicke, F. Kessler, et al. “CIGS thin-film solar cells and modules on enameled steel substrates,” *Solar Energy Materials & Solar Cells*, vol. 100, pp. 132–137, 2012.
- [63] K. L. Schulte, J. Simon, and A. J. Ptak, “Multijunction Ga_{0.5}In_{0.5}P/GaAs solar cells grown by dynamic hydride vapor phase epitaxy,” *Prog Photovolt Res Appl*. 2018; 26(11): 887-893, Nov. 2018.
- [64] M. Woodhouse and A. Goodrich, “A manufacturing cost analysis relevant to single and dual junction photovoltaic cells fabricated with III–Vs and III–Vs grown on Czochralski Silicon,” NREL: Washington, DC, USA, NREL Rep. No. PR-6A20-60126 92 (2014).
- [65] B. M. Kayes, H. Nie, R. Twist, S. G. Spruytte, F. Reinhardt, I. C. Kizilyalli, G. S. Higashi, “27.6% Conversion efficiency, a new record for single-junction solar cells under 1 sun illumination,” in *Proceedings of the 37th IEEE Photovoltaic Specialists Conference*, WA, USA, 2011.
- [66] A. Ramyar, H. Iman-Eini, and S. Farhangi, “Global maximum power point tracking method for photovoltaic arrays under partial shading conditions,” *IEEE Trans. on Industrial Electronics*, vol. 64, no. 4, pp. 2855-2864, 2017.
- [67] J. Saikrishna Goud, R. Kalpana, and B. Singh, “A hybrid global maximum power point tracking technique with fast convergence speed for partial-shaded PV systems,” *IEEE Trans. on Industry Applications*, vol. 54, no. 5, pp. 5367-5376, 2018.

- [68] P. Sharma and V. Agarwal, "Exact maximum power point tracking of grid-connected partially shaded PV source using current compensation concept," *IEEE Trans. on Power Electronics*, vol. 29, no. 9, pp. 4684-4692, 2014.
- [69] S. M P, M. Das and V. Agarwal, "Design and development of a novel high voltage gain, high-efficiency bidirectional DC–DC converter for storage interface," *IEEE Transactions on Industrial Electronics*, vol. 66, no. 6, pp. 4490-4501, June 2019.
- [70] S. Hasanpour, A. Baghrmian and H. Mojallali, "A modified SEPIC-based high step-up DC–DC converter with quasi-resonant operation for renewable energy applications," *IEEE Transactions on Industrial Electronics*, vol. 66, no. 5, May 2019.
- [71] Technical Specification of the Single Phase Distribution Transformer, TUNISIE Transformateurs S.A., Available online: http://www.ttransfo.com/pdf/Mono_eng.pdf [Accessed April 2020]
- [72] National Renewable Energy Laboratory, "NASA Remote Sensing Validation Data: Saudi Arabia". Available online: <https://www.nrel.gov/grid/solar-resource/saudi-arabia.html> [Accessed April 2020]
- [73] Electric Rate Schedules, Los Angeles Department of Water and Power (LADWP). Available online: https://www.ladwp.com/ladwp/faces/ladwp/aboutus/a-financesandreports/a-fr-electricrates/a-fr-electricrateschedules?_afLoop=991116924199422&_afWindowMode=0&_afWindowId=14pig7wmp8_1#%40%3F_afWindowId%3D14pig7wmp8_1%26_afLoop%3D991116924199422%26_afWindowMode%3D0%26_adf.ctrl-state%3Dhzruxpkzd_4 [Accessed April 2020]
- [74] Electric Rates for Michigan Customers, June 2018. Available online: https://www.we-energies.com/business/elec/mi_rates.pdf [Accessed April 2020]
- [75] Los Angeles Times. Available online: <https://www.latimes.com/opinion/op-ed/la-oe-lippe-dwp-rate-increase-20150814-story.html> [Accessed April 2020]
- [76] Michigan Taxes, Michigan Department of Treasury. Available online: https://www.michigan.gov/taxes/0,4676,7-238-43519_43529-154427--,00.html [Accessed April 2020]
- [77] U.S. Energy Information Administration, 2019. Available online: <https://www.eia.gov/electricity/state/michigan/index.php> [Accessed April 2020]

- [78] U.S. Energy Information Administration, 2019. Available online: <https://www.eia.gov/state/?sid=MI#tabs-4> [Accessed April 2020]
- [79] V. Kljaic, “Brief glimpse into California’s electric car market: sales approach 500,000”, Inside EVs, Sept. 2018, Available online: <https://insideevs.com/news/340564/brief-glimpse-into-californias-electric-car-market-sales-approach-500000/> [Accessed April 2020]
- [80] Online: <http://pvinsights.com/> [Accessed April 2020]
- [81] Online: <https://www.statista.com/statistics/971982/solar-pv-capex-worldwide-utility-scale/> [Accessed April 2020]
- [82] U.S. Department of Energy, “Electrical and Electronics Technical Team Roadmap”, June 2013. Available online: https://www1.eere.energy.gov/vehiclesandfuels/pdfs/program/eett_roadmap_june2013.pdf [Accessed April 2020]
- [83] J. A. Baxter, D. A. Merced, D. J. Costinett, L. M. Tolbert, and B. Ozpineci, “Review of Electrical Architectures and Power Requirements for Automated Vehicles,” in *Proc. 2018 IEEE Transportation Electrification Conference and Expo (ITEC)*, 2018.
- [84] North American Council for Freight Efficiency. Available online: <https://nacfe.org/technology/solar-panels-2/> [Accessed April 2020]
- [85] B.-K. Lee, J.-P. Kim, S.-G. Kim, J.-Y. Lee, “An isolated/bidirectional PWM resonant converter for V2G(H) EV on-board charger,” *IEEE Transactions on Vehicular Technology*, vol. 66, no. 9, pp. 7741-7750, 2017.
- [86] B. Lin, Q. Li, F. Lee, Z. Liu, Y. Yang, “A high-efficiency high-density wide-bandgap device-based bidirectional on-board charger,” *IEEE Journal of Emerging and Selected Topics in Power Electronics*, vol. 6, no. 3, pp. 1627-1636, 2018.
- [87] M. Kwon, S. Choi, “An electrolytic capacitorless bidirectional EV charger for V2G and V2H applications,” *IEEE Transactions on Power Electronics*, vol. 32, no. 9, pp. 6792-6799, 2017.
- [88] D. Das, N. Weise, K. Basu, R. Baranwal, N. Mohan, “A bidirectional soft-switched DAB-based single-stage three-phase AC-DC converter for V2G application,” *IEEE Transactions on Transportation Electrification*, vol. 5, no. 1, pp. 186-199, 2019.

Chapter 4: A Fast Parabolic-Assumption Algorithm for Global MPPT of Photovoltaic Systems Under Partial Shading Conditions

4.1. Introduction

When considering the practical challenges related to optimizing and manufacturing the large-scale SEV concept proposed in Chapter 3, one main concern is to maximize the capture of solar energy at all times of the day, even under partial shading conditions when the vehicle is driving. Though much work has been done to utilize maximum power point tracking (MPPT) in large scale or distributed stationary solar generation to maximize the solar energy captured in varying radiation conditions [1], there has not been much focus on very fast algorithms suitable for a moving vehicle. Thus, this chapter proposes a new MPPT algorithm that is much faster than prior algorithms, for use with the proposed large-scale SEV.

A PV module's maximum power point (MPP) is situated at the knee of the current-voltage (I-V) characteristic curve, which is unique to each module, and changes with ambient or environmental disturbances. Since PV module voltages are typically low, multiple modules are often connected in series to create a higher-voltage PV array. A bypass diode is connected across each module to allow that module to be bypassed when partial shading conditions (PSCs) occur.

When all modules in an array get the same solar radiation, the I-V curve of the PV array has a single knee, and the power-voltage (P-V) characteristic curve

produces a single peak, meaning conventional MPPT algorithms can easily find the MPP. However, if the radiation levels on the PV modules are not uniform, meaning partial shading is occurring, the I-V and P-V curves have multiple peaks. Finding the global MPP (GMPP) is difficult in this case for conventional MPPT algorithms like hill-climbing [2], perturb and observe [3], and incremental conductance [3], because they can easily get “trapped” at one of the multiple local MPPs. PSCs can often occur from shadows of clouds, buildings, trees, etc. For example, [4] studied rooftop PV systems in Germany and found that 41% of PV arrays had been affected by shading resulting in up to 10% energy loss. Further, [5] found up to a 70% energy loss from partially shaded PV arrays due to failure in detecting the GMPPT.

GMPPT techniques for PSCs can be categorized into two groups: hardware-based and software-based techniques. Some hardware methods include adding a small buck converter to each PV module [6], switching-based reconfigurations of PV modules [7], [8], and voltage equalizer circuits [9]. Furthermore, [10] proposes a hardware-based distributed maximum power point tracking (DMPPT) strategy based on a multi-winding forward-based converter, which acts as a current balancing differential power processing converter. The converter is configured so that each port is connected in parallel with an individual PV module to ensure module-level maximum power extraction. Reference [11] proposes a new DMPPT control algorithm by introducing coordination between the distributed and centralized control to improve dynamic performance while dealing with PSCs. A novel approach in [12] uses the image of the shaded and unshaded PV modules

from an optical camera to calculate the GMPP, though infrastructure cost is high and the optimal camera itself may add shading. Though many of these hardware methods are good in terms of GMPPT efficiency (meaning how close they operate to the true GMPPT) and convergence speed, the practical usefulness is limited due to the cost and complexity of the additional hardware required.

Software GMPPT methods operate based on setting different duty cycles at the DC-DC converter until the GMPP is reached. The event of setting a single duty cycle at the converter will be called a “step” in this chapter. As no literature proposed to date as per the authors’ knowledge can calculate the position of the GMPP during any PSC, every software-based GMPPT method proposed to date has tried to minimize both the number of steps and search space along the P-V curve to reach the GMPP by proposing various techniques for faster convergence. These methods can be categorized into two groups: modifications to conventional MPPT algorithms and optimization-based algorithms. In the first group, [13] presents a modified hill climbing (HC) algorithm that measures the PV array current at multiples of 80% of the module’s open circuit voltage, calculates the number and length of segments in the I-V curve to find the local MPPs, then uses hill climbing to find the GMPP. The main drawbacks are the slow convergence speed due to the need to scan a major portion of the P-V curve with several steps, and the fact that with an increase in the number of series-connected modules, the algorithm can miss the GMPP. This occurs when the algorithm’s predicted position for the last peak moves to the left of the actual position of the last peak, due to the right shifting

property of peaks under PSCs. For S series modules in an array, there is a chance that the algorithm will scan for the S^{th} peak in $(S-1)^{\text{th}}$ zone of the I-V curve. Further examples include a scanning technique with separate controllers for each level module [14], the use of a cubic spline algorithm [15], the combination of the hill-climbing algorithm with detection of dP/dV sign change [16], a fast GMPPT algorithm that requires additional current sensors for each PV module [17], the combination of the perturb and observe (P&O) algorithm with variation of the ramp of the duty cycle change during P-V curve sampling [18] (though the GMPP may be missed for a higher ramp of duty cycle changes), and a skipping mechanism to improve convergence speed by discarding unwanted search areas in the scan which requires two sensors, increasing cost [19]. Overall, these modified GMPPT techniques are efficient but have slow convergence speeds due to numerous steps and/or require additional sensors, increasing cost.

Optimization-based GMPPT algorithms include conventional and modified particle swarm optimizations (PSOs) [20], [21], [22], artificial bee colony (ABC) [23], genetic algorithm based fuzzy-MPPT [24], greywolf optimization [25], crowded plant height optimization [26], team game optimization [27], fusion firefly algorithm [28], chaotic flower pollination [29], and artificial neural network algorithm [30]. Many of these cannot differentiate between uniform radiation and PSCs, so [31] proposes a combination of the hill-climbing (HC) algorithm in uniform radiation conditions and ABC algorithm in PSCs. Similarly, [32] proposes another hybrid tracking algorithm that combines conventional P&O to track GMPP

in uniform radiation and moderate PSCs, and flower pollination algorithm to track GMPP during extreme PSCs. However, all optimization-based GMPPT algorithms for PSCs suffer from slow convergence speed because of the use of numerous steps due to their heuristic nature.

Modern PV systems require high GMPP convergence speeds to minimize energy loss during partial shading conditions. This is especially critical for emerging mobile PV applications such as on-board solar generation for electric vehicles [33] or aircraft [34]. Also, low sensor cost and high GMPPT efficiency is required for successful practical implementation. Thus, this chapter proposes a totally new approach of a software-based GMPPT algorithm that does not fit into the usual categories of modified GMPPT algorithms that blindly search the I-V curve or heuristic optimization algorithms. Instead, the proposed method analytically calculates the GMPP near-exactly during PSCs using exactly S current measurements, where S is the number of series modules in the array, therefore requiring only S steps. The I-V curve of each module is divided into two zones (constant current and parabola), and the algorithm calculates the position of the GMPP using the basic conical geometric equation of the parabola, thus the algorithm is named *Parabolic Assumption* (PA). The idea of using parabolic progression to find the MPP of a single PV module or a uniformly shaded array has been suggested in [35] – [37]. However, these methods are similar to conventional P&O or HC, where three points are assumed on the P-V curve to fit a parabola, and after several iterations, the point with the maximum power is set as the MPP. These

methods are not designed to be used in PSCs as they can get trapped at local peaks (LPs), just like other P&O or HC methods. Conversely, the proposed PA algorithm in this chapter addresses the more complex problem of PSCs by using the PA on the I-V curve to calculate the amount of right shift of the LPs during PSCs.

Compared to contemporary GMPPT algorithms for PSCs, the proposed PA algorithm has the following advantages:

- 1) Due to its analytical nature, the convergence speed is significantly higher than any existing GMPPT algorithm, setting a new standard for GMPPT speed. It always uses exactly S measurement steps to calculate the GMPP, where S is the number of series modules in the PV array. In this chapter four modules are used as the test case, so four steps are required, compared to a hundred or more for some optimization-based algorithms.
- 2) The S measurement steps are inherently used to determine if PSC has occurred, so no extra steps are needed.
- 3) Low hardware costs: uses a single current sensor and a simple microcontroller with low computational burden.
- 4) Guaranteed to find the GMPP in all PSCs with high tracking efficiency (where tracking efficiency is equal to or better than that of comparison algorithms).

Overall, the fast convergence speed, accuracy, low cost, and simplicity of the entirely unique proposed PA algorithm puts it in a class of its own and sets a new

standard for GMPPT algorithms for PSCs. This chapter is organized as follows: Section 4.2 describes PV system modeling, Section 4.3 presents the PA algorithm in detail, Section 4.4 presents simulation results, Section 4.5 presents experimental results, and Section 4.6 concludes the chapter.

4.2. PV System Modeling

4.2.1 Single Diode Model

Fig. 4.1 shows the single diode model of a PV cell. Multiple cells are connected in series in a PV module. If V is the terminal voltage of a single cell, the current provided by the cell can be written using KVL and KCL as:

$$I_{pv} = I_{ph} - I_d - \frac{V + I_{pv} R_s}{R_p} \quad (1)$$

where R_s and R_p are the series and parallel resistances in the cell model, respectively. The diode current, I_d , diode saturation current, I_0 , and the photocurrent I_{ph} can be expressed as [38], [39]:

$$I_d = I_0 \left[\exp\left(\frac{q(V + I_{pv} R_s)}{akT}\right) - 1 \right] \quad (2)$$

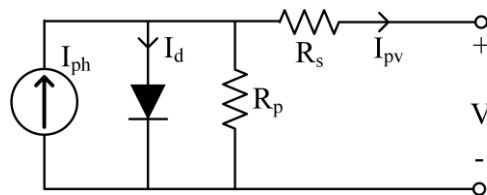


Fig. 4.1. Single-diode model of a solar cell.

$$I_0 = \frac{I_{sc_STC} + K_I \Delta T}{\exp(q(V_{oc_STC} + K_V \Delta T) / akT) - 1} \quad (3)$$

$$I_{ph} = \frac{G}{G_{STC}} (I_{ph_STC} + K_I \Delta T) \quad (4)$$

where “ a ” is the diode ideality factor, k is Boltzmann’s constant ($1.3806503 \times 10^{-23}$ J/K), T is the panel temperature (in K), and q is the electron charge ($1.60217646 \times 10^{-19}$ C). In (3) and (4), G_{STC} and I_{ph_STC} are the radiation and photocurrent at standard test conditions (STC), i.e., 1000 W/m^2 at 25°C , respectively, G is the present radiation, K_I and K_V are the temperature coefficients of current and voltage respectively from the manufacturer, and ΔT is the temperature difference from STC. If n_c number of cells are connected in series to make a PV module, the open circuit voltage, V_{oc} of the module at $I_{pv}=0$ can be written as [40]:

$$V_{oc} = n_c \frac{akT}{q} \ln\left(\frac{I_{ph}}{I_0}\right) \quad (5)$$

Though a change in radiation can be sudden, a change in temperature happens more slowly over time [39]. This results in a change in the photocurrent proportional to the change in radiation during PSCs [39]. Also, though $R_p \gg R_s$, the short-circuit current I_{sc} eventually satisfies $I_{sc} \approx I_{pv} \approx I_{ph}$ during a short-circuit event. The MPP voltage and current satisfy $V_{mpp} \approx 0.8V_{oc}$ and $I_{mpp} \approx 0.9I_{sc}$ [41] respectively. Therefore, the relation between different currents and radiations can be written as (6). The proposed PA algorithm measures each module’s I_{sc} , then uses the right half of (6) to calculate the corresponding radiation, G , on that module, since I_{sc_STC} and

G_{STC} are known from the datasheet. In this study, the solar module SunPower SPR-200-WHT-U is used for analysis, with specifications shown in Table 4.1.

$$\frac{I_{ph}}{I_{ph_STC}} \approx \frac{I_{mpp}}{I_{mpp_STC}} \approx \frac{I_{sc}}{I_{sc_STC}} \approx \frac{G}{G_{STC}} \quad (6)$$

Table 4.1. Specifications of Sunpower SPR-200-WHT-U

Parameters	Variable	Value	Unit
Open-circuit voltage	V_{oc}	47.8	V
Short-circuit current	I_{sc}	5.4	A
Voltage at maximum power	V_{mpp}	40	V
Current at maximum power	I_{mpp}	5	A
Maximum power	P_{mpp}	200	W
Temperature coefficient of V_{oc}	K_v	-0.2919	%/°C
Temperature coefficient of I_{sc}	K_I	0.043	%/°C
Diode saturation current	I_0	1.2832e-11	A
Diode ideality factor	a	0.96675	N/A
Cells per module	n_c	72	N/A
Series resistance	R_s	0.4427	Ω

4.2.2 I-V & P-V Characteristics of PV Array Under PSCs

Fig. 4.2 shows a PSC on a 4S1P solar array, where S is equal to four. Fig. 4.3 shows the I-V and P-V curves of this PV array along with those for an unshaded array. During PSCs, the bypass diodes are activated by the radiation difference between two modules, diverting the current away from the partially shaded modules. As a result, a staircase I-V curve is formed, while the corresponding P-V curve generates multiple local peaks. The goal of GMPPT algorithms is to find the GMPP, without getting trapped at any of the local peaks.

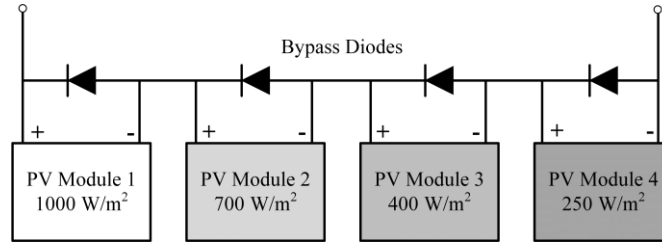


Fig. 4.2. Example of partial shading condition on a 4S1P PV array.

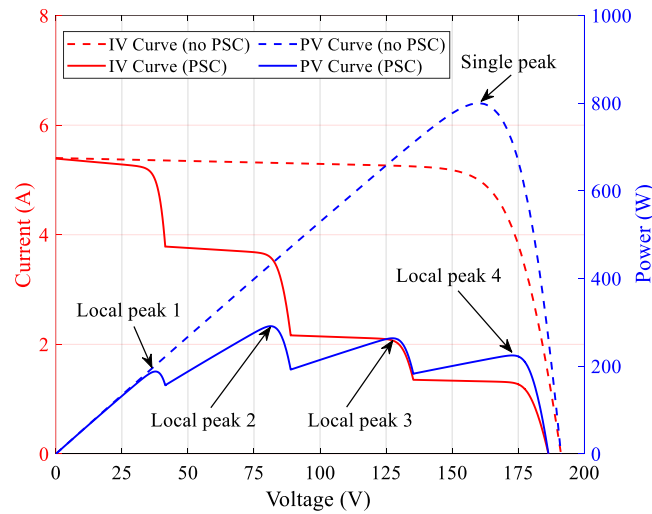


Fig. 4.3. Multiple local peaks during partial shading condition.

4.3. Proposed Parabolic Assumption Algorithm

4.3.1 Mathematical Description of Parabolas

A parabola is defined as a set of all points on a plane equally distant from a given line, L , called the *directrix* and a given point, *focus* not on the line, L , as shown in Fig. 4.4(a). The distance between *directrix* and *focus* is known as the focal parameter, p and given by $p=2f$, where f is the distance between the *vertex* and the *directrix* or the *focus*. Depending on where the parabola is located on the coordinate system, the parabola equations also change, as shown in Fig. 4.4(b) and 4.4(c). The

standard equation of a parabola having the y-axis as the main axis is $x^2=4fy$. A parabola having its *vertex* at the coordinate (α,β) and having negative y-axis as its axis has an equation of $(x-\alpha)^2=-4f(y-\beta)$.

4.3.2 Parabolic Assumption for Partial Shading

The trend of the I-V characteristic curve of an unshaded PV array is that the current is almost constant up to a certain voltage, and then the current decreases almost in an exponential fashion. This exponential progression is almost identical to a parabolic progression imagining the vertex is located at the MPP, like Fig. 4.4(c). This idea of the parabolic progression helps calculate the amount of right-shift of the local peaks during PSC and compute the positions of those peaks near-exactly to avoid the problems with missing the peak that could happen with GMPPT techniques such as [13]. Other geometrical progressions were also evaluated (linear and ellipse), as show in Fig. 4.5. Hyperbola was excluded from consideration as vertices of hyperbolas are not at the intersection of their conjugate and transverse axis, which means further unknown parameters would be required, complicating

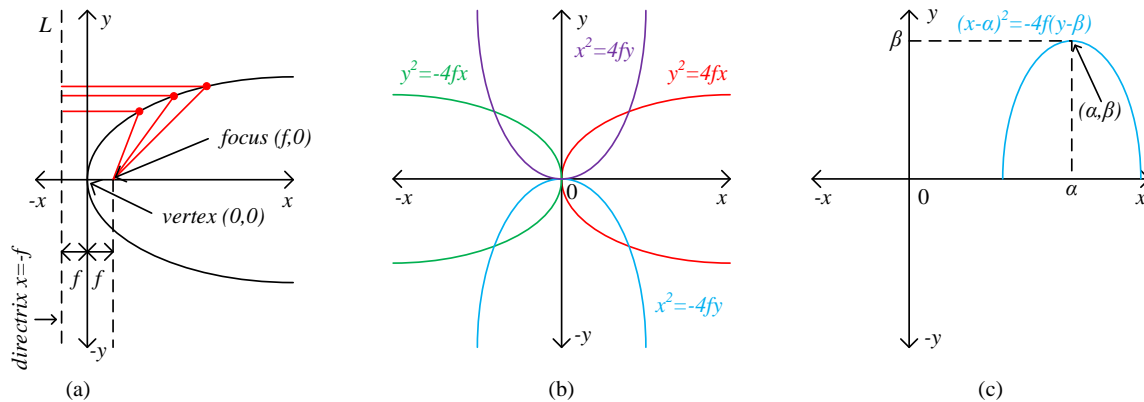


Fig. 4.4. Parabolas at different positions and their respective equations.

the algorithm. Fig. 4.5 shows that the parabolic progression most closely mimics the real I-V curve. The root-mean-square errors between the I-V curve and each progression are 0.045 for the parabola, 0.883 for linear, and 0.747 for ellipse, which justify the choice of parabolic expression for the proposed MPPT algorithm.

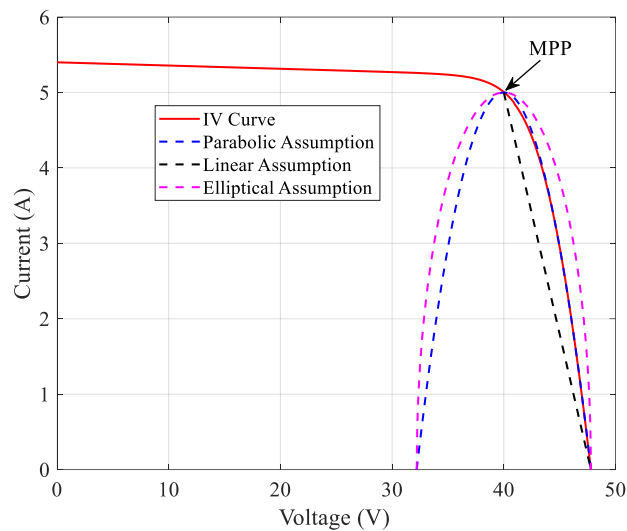


Fig. 4.5. Justification of Parabolic Assumption (PA).

To illustrate this process, Fig. 4.6 shows a typical PV system with a solar array, a DC-DC converter, and a battery. The proposed PA algorithm must scan the PV current at S precise voltages, shown as V_{pv} in (7), and thus requires a steady DC voltage at the output of the DC-DC converter (V_o in (7)) so that setting a certain duty cycle, D , will give the corresponding desired V_{pv} . This constant output voltage can be from a storage battery, which is often used due to the variable nature of solar power, or a DC-link capacitor in a grid-connected system without a storage battery. This chapter focuses on the algorithm application in a battery-based PV system.

$$V_{pv} = V_o(1 - D) \quad (7)$$

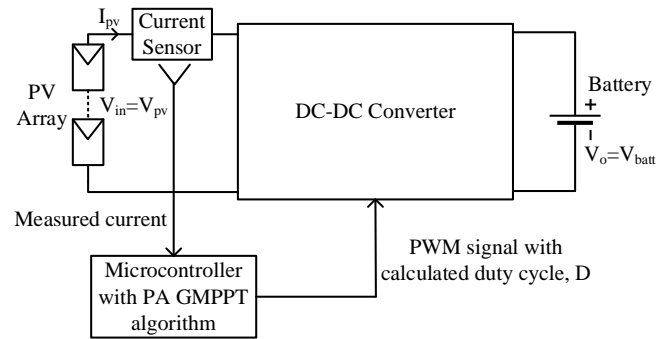


Fig. 4.6. Schematic of the PV system.

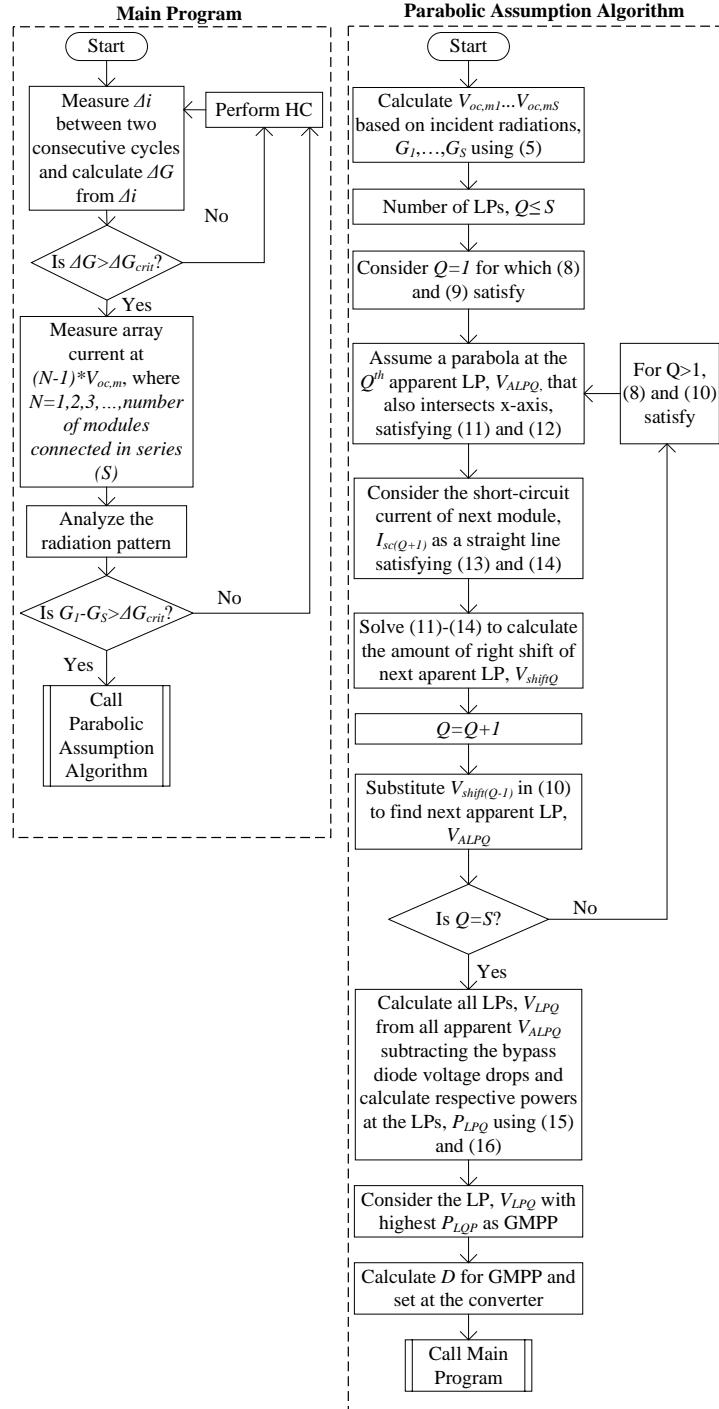


Fig. 4.7. Flowchart of the proposed PA GMPPT algorithm.

Fig. 4.7 summarizes the proposed PA GMPPT algorithm and Fig. 4.8 shows the example of a 4S1P array I-V curve with the PSC pattern of Fig. 4.2, excluding

the voltage drops of the bypass diodes. On a timed loop, the controller checks for a change in current, Δi , which indicates a change in radiation ΔG using (6). Once ΔG is higher than $\Delta G_{crit} = 50 \text{ W/m}^2$ [39], a large radiation change is considered to have taken place. The controller then scans currents at S steps at the voltage points of $(N-1)V_{oc,m}$, where $V_{oc,m}$ is a module's standard open circuit voltage and N ranges from 1 to S . Therefore, the ideal voltage points to scan are 0 V , $V_{oc,m}$, $2V_{oc,m}$, and $3V_{oc,m}$. However, the first scan is done at a relatively higher voltage, e.g., 30 V , as the current is almost constant up to 38 V in this module. The obtained currents, i.e., I_{sc1} , I_{sc2} , I_{sc3} , and I_{sc4} are converted to G_1 , G_2 , G_3 , and G_4 respectively using (6), and the new radiation pattern is mapped out. If $G_1 - G_4 \leq G_{crit}$, the controller confirms that the system is under uniform radiation and activates the Hill Climbing (HC) algorithm [13], which is not the focus of this chapter. If $G_1 - G_4 > G_{crit}$, a PSC is confirmed, and the PA GMPPT algorithm is activated. The PA algorithm is unique from all other methods in the literature because other methods will now try several blind steps to reach the GMPP, but the proposed PA algorithm will calculate the position of the GMPP just by knowing the PSC pattern, and move there right away. In other words, the PA algorithm uses the current measurements required to detect a PSC for direct calculation of GMPP, without requiring any additional steps/measurements.

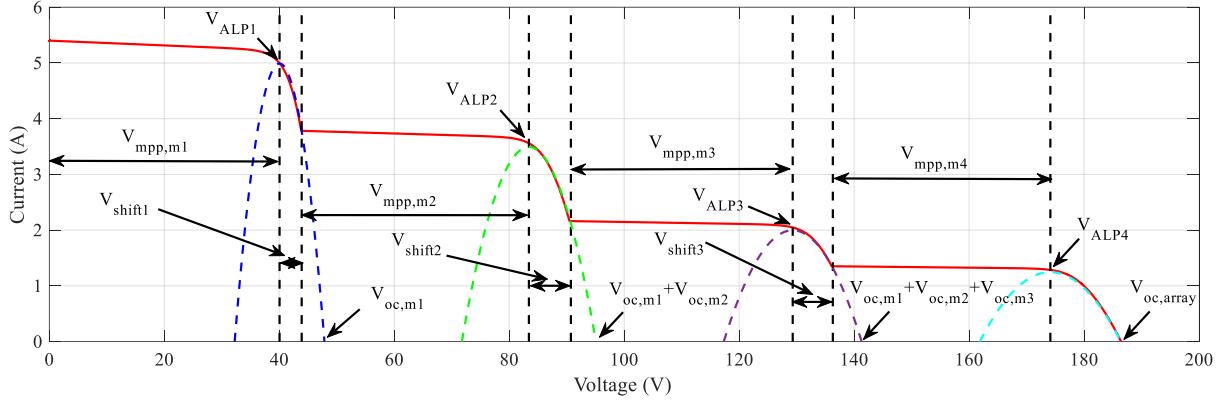


Fig. 4.8. Application of Parabolic Assumption (PA) method on I-V characteristic curve during PSC.

The actual open circuit voltages of modules 1 to 4, $V_{oc,m1}$, $V_{oc,m2}$, $V_{oc,m3}$, and $V_{oc,m4}$, vary based on the incident radiations of G_1 , G_2 , G_3 , and G_4 , therefore, are calculated using scanned short-circuit currents I_{sc1} , I_{sc2} , I_{sc3} , and I_{sc4} , using (5). In (8), the ratio of V_{mpp} to V_{oc} from the datasheet is used, which is 0.837 in this case as shown in Table 4.1. Also from the datasheet, the ratio of I_{mpp} to I_{sc} is 0.926. Q denotes the number of the local peak that can range from 1 to S .

$$V_{mpp,mQ} = \frac{V_{mpp}}{V_{oc}} V_{oc,mQ} \quad (8)$$

$$I_{mpp,mQ} = \frac{I_{mpp}}{I_{sc}} I_{sc,mQ}$$

For $Q=1$, the 1st apparent local peak (ALP), V_{ALP1} , is equal to the V_{mpp} of module 1 as in (9). But for $Q \geq 2$, the ALPs are shifted to the right by $V_{shift(Q-1)}$ as shown in Fig. 4.8 and (10).

$$V_{ALP1} = V_{mpp,m1} \quad (9)$$

$$V_{ALPQ} = V_{ALP(Q-1)} + V_{shift(Q-1)} + V_{mpp,mQ} \quad \text{if } Q \geq 2 \quad (10)$$

To calculate $V_{shift(Q-1)}$, a parabola is assumed through each ALP on the I-V curve having the parabolic equation (11), where the coordinates of all the points on these parabolas belong to the set (x_Q, y_Q) .

$$(x_Q - V_{ALPQ})^2 = -4f_Q(y_Q - I_{mpp,mQ}) \quad (11)$$

These parabolas are also considered to go through the open circuit voltage of the activated modules on the I-V curve, as described in (12). For example, $Q=1$ means the 1st parabola which goes through $(V_{oc,m1}, 0)$ and $Q=3$ means the 3rd parabola which goes through $(V_{oc,m1} + V_{oc,m2} + V_{oc,m3}, 0)$.

$$\left(\sum_{z=1}^Q V_{oc,mz}, 0 \right) \in (x_Q, y_Q) \quad (12)$$

Substituting $(V_{ALP1}, I_{mpp,m1})$ from (8) and (9) and $(x_1, y_1) = (V_{oc,m1}, 0)$ from (12) in (11), focus, f_1 can be calculated. It is also clear from Fig. 4.8 that every parabola intersects with the short circuit current curve of the next module. For example, the 1st parabola intersects with I_{sc2} and the 3rd parabola intersects with I_{sc4} . Hence, the coordinate of the intersection point can be described as shown in (15) and (16).

$$(V_{ALPQ} + V_{shiftQ}) \in x_Q \quad (13)$$

$$I_{sc(Q+1)} \in y_Q \quad (14)$$

For the 1st parabola where $Q=1$, (14) becomes $y_1=I_{sc2}$. Substituting y_1, f_1 , and $(V_{ALP1}, I_{mpp,m1})$ in (11), x_1 is solved. Replacing the value of x_1 and V_{ALP1} in (13), V_{shift1} is calculated, by which the 2nd peak is shifted to the right. Therefore, for $Q=2$, $V_{mpp,m2}$ is added with V_{shift1} and V_{ALP1} as in (10) and V_{ALP2} is near-exactly calculated. The current at this point is $I_{mpp,m2}$.

To calculate the third peak, a 2nd parabola with its vertex at $(V_{ALP2}, I_{mpp,m2})$ having equation (11) is considered, where $Q=2$. It also goes through $(V_{oc,m1} + V_{oc,m2}, 0)$ as described in (12). Thus, f_2 is calculated by substituting $(V_{ALP2}, I_{mpp,m2})$ and $(x_2, y_2) = (V_{oc,m1} + V_{oc,m2}, 0)$ in (11). Assuming the same parabola intersects with $y_2=I_{sc3}$, x_2 is solved from (11), which eventually gives the 2nd right shift V_{shift2} using (13). Therefore, for $Q=3$, $V_{mpp,m3}$ is added with V_{shift2} and V_{ALP2} as in (10) and V_{ALP3} is near-accurately calculated. The current at this point is $I_{mpp,m3}$. $(V_{ALP4}, I_{mpp,m4})$ can also be found in similar way.

Once all the apparent local peaks are known, the algorithm finds the actual local peaks V_{LPQ} and their corresponding powers P_{LPQ} as shown in (15) and (16) by subtracting the required bypass diode voltage drop V_{d_drop} per diode.

$$V_{LPQ} = (V_{ALPQ} - (S - Q)V_{d_drop}) \quad (15)$$

$$P_{LPQ} = V_{LPQ} I_{mpp,mQ} \quad (16)$$

By comparing the power levels at these peaks, the algorithm finds the GMPP and sets the appropriate duty cycle at the DC-DC converter. If there is a

situation where multiple modules have the same radiation during PSC, this algorithm assumes a single parabola at the single peak for all the similarly shaded modules and adjusts the algorithm accordingly.

4.3.3 Effect of Temperature Variation

The two PV parameters used in the algorithm which are dependent on temperature are V_{oc} and I_0 . These can be updated once the temperature is known. As discussed in [39], temperature change is a relatively slow process which may take spans of hours. Thus, the HC algorithm can be periodically run (e.g., every 10 or 20 minutes) around the present assumed MPP to check if the actual MPP has shifted to a new voltage point, indicating a temperature change. From any difference of the two voltages, the new temperature value can be found using the temperature coefficient of voltage, K_v , provided by the manufacturer. This temperature can then be used to update the diode saturation current, I_0 using (3). Using the periodically-updated values of V_{oc} and I_0 , the PA algorithm can run as usual eliminating the requirement of a temperature sensor.

4.4. Simulation Results

4.4.1 Proposed PA Algorithm

To evaluate the performance of the proposed PA GMPPT algorithm during PSCs, the system in Fig. 4.6 is modeled in MATLAB/Simulink with a 4S1P PV array and a boost converter. As the input voltage to the boost converter is the PV voltage and the output voltage of the boost converter is the battery voltage, (7) can

be written as (17). Table 4.2 shows the modeled parameters. The system is simulated under 4 different PSC radiation patterns with different numbers of local peaks (LPs) and different positions of the global peaks (GPs), as shown in Table 4.3. The respective I-V and P-V characteristic curves for these 4 PSC patterns are shown in Figs. 4.9 and 4.10.

$$V_{pv} = V_{batt} (1 - D) \quad (17)$$

Table 4.2. System Modeling Parameters

Parameters	Value
Array configuration	4S1P
No. of series connected bypass diodes	4
Bypass diode voltage drop, V_{d_drop}	0.8 [13]
V_{oc} and I_{sc} of the array (STC)	191.2 V & 5.4 A
V_{mpp} and I_{mpp} of the array (STC)	160 V & 5 A
P_{mpp} of the array (STC)	800 W
Boost converter inductor, L	650 μ H
Boost converter capacitors, C_{in} & C_{out}	20 μ F & 20.15 μ F
Switching frequency	40 kHz
Battery terminal voltage, V_{batt}	200V

Table 4.3. Details of PSC Patterns

PSC Pattern	Radiation (W/m ²)				Number of LPs	Position of GP
	Module 1	Module 2	Module 3	Module 4		
1	1000	900	800	700	4	4 th LP
2	1000	1000	520	300	3	1 st LP
3	1000	900	750	400	4	3 rd LP
4	1000	200	300	150	4	1 st LP

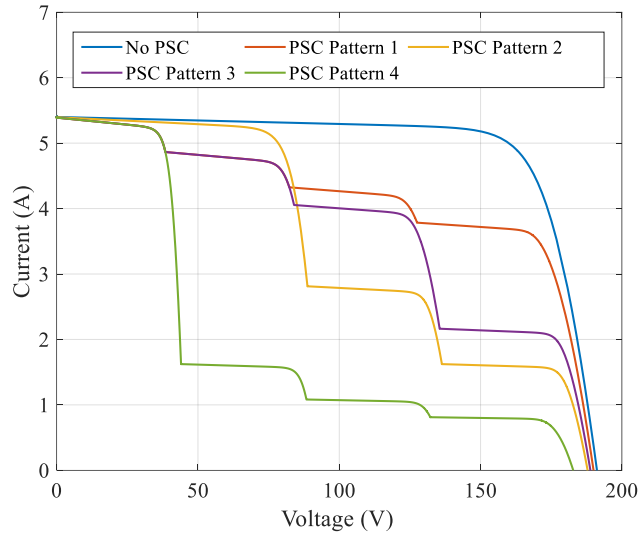


Fig. 4.9. I-V characteristic curves for four different PSC patterns.

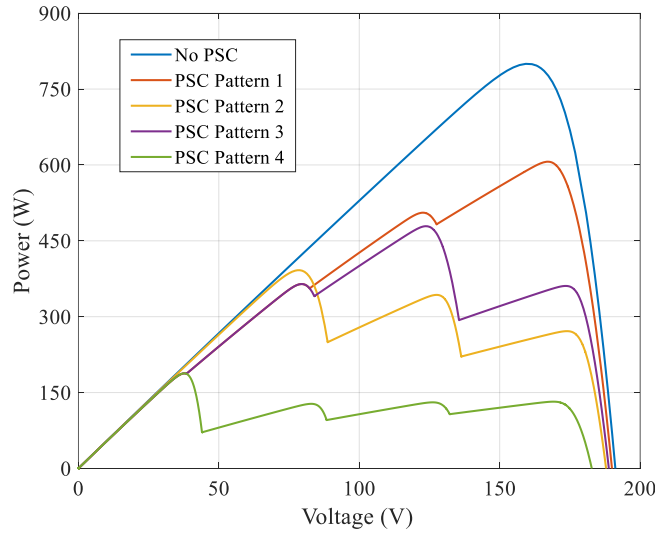


Fig. 4.10. P-V characteristic curves for four different PSC patterns.

Fig. 4.11 shows the performance of the proposed PA GMPPT algorithm for PSC patterns 1 and 2, and Fig. 4.12 does the same for patterns 3 and 4. Fig. 4.11 shows that the considered PV system starts delivering power at MPP at STC from 0 s. Table 4.2 shows that $V_{mpp}=160$ V at STC, and $V_{batt}=200$ V. Hence, the duty cycle

for the boost converter to operate at STC for maximum power extraction is 0.2 using (17). The PV array experiences the PSC pattern 1 and a sudden change in the current at 0.051 s. The current sensor keeps scanning for a current change every 0.025 s, which is enough time for the PV voltage oscillation to die down after a change in duty cycle. By comparing the sensed currents at 0.05 s and 0.075 s, the controller detects a large change in the radiation. Hence, the controller activates current scanning immediately at 0.075 s to find the shading pattern. Though the theoretical order of the current scanning points are 30 V, $V_{oc,m}$, $2V_{oc,m}$, and $3V_{oc,m}$, the practical scanning starts from either the theoretical 1st or last scanning point, whichever is closer to the present operating PV voltage to avoid large oscillations in the voltage. In this case, the scanning happens at $3V_{oc,m}$, $2V_{oc,m}$, $V_{oc,m}$, and 30 V, or 143.4 V, 95.6 V, 47.8 V, and 30 V using duty cycles 0.283, 0.522, 0.761, and 0.85, respectively as per (17). Hence, the controller measures the currents as 3.74 A, 4.29 A, 4.84 A, and 5.27 A at 0.1 s, 0.125 s, 0.15 s, and 0.175 s, respectively. At 0.175 s, the controller converts these currents into radiations using (6), which are 692.59 W/m², 794.44 W/m², 896.30 W/m², and 975.93 W/m², respectively. The PSC pattern 1 has the actual radiation values of 700 W/m², 800 W/m², 900 W/m², and 1000 W/m². Thus, the error for calculating G for each module using (6) is 1.06%, 0.70%, 0.41%, and 2.41%. The reason for the slightly higher error of the highest current module is that I_{sc} is measured at 30 V instead of 0 V. Nevertheless, these calculated estimates of G allow for very high tracking efficiency in the PA algorithm, as will be shown below. Comparing these radiation values, the algorithm

confirms partial shading has occurred. Thus, the PA GMPPT algorithm is called which immediately calculates that the GMPP is at 168.4 V using these four current measurements and (8)-(16). Then, the required duty cycle for the boost converter to have an input voltage of 168.4 V is calculated as $D=0.158$ using (17), and immediately set at the converter. The current at this point is 3.595 A, so the tracked input power is 605.4 W. Fig. 4.10 shows that the expected maximum power for PSC pattern 1 is 606.4 W. Hence, the tracking efficiency is 99.84%. Moreover, the controller has taken only four steps or 0.1 s at the given current measurement time interval to track the GMPP using the PA algorithm. In Fig. 4.11, PSC pattern 2 occurs at 0.305 s, and the same process ensues, this time with a tracking efficiency of 99.9%, and again using only four steps. Fig. 4.12 shows the performance of the proposed PA algorithm for PSC patterns 3 and 4. Again, high tracking efficiencies of 99.67% and 99.39% are obtained in only four steps per PSC pattern.

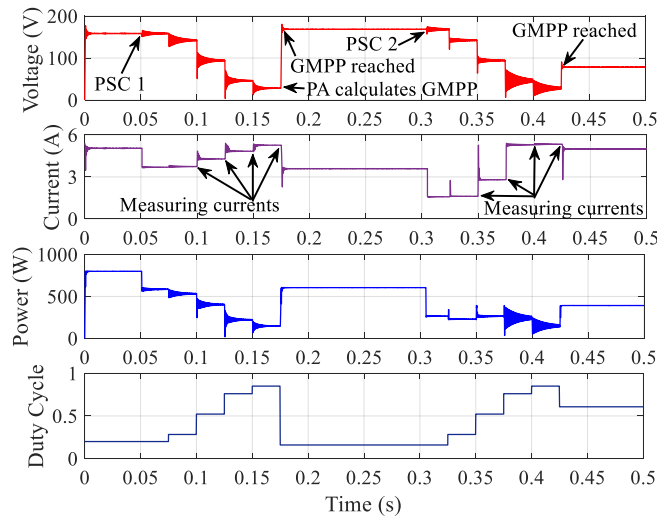


Fig. 4.11. Simulation of the performance of the proposed PA algorithm under PSC patterns 1 and 2.

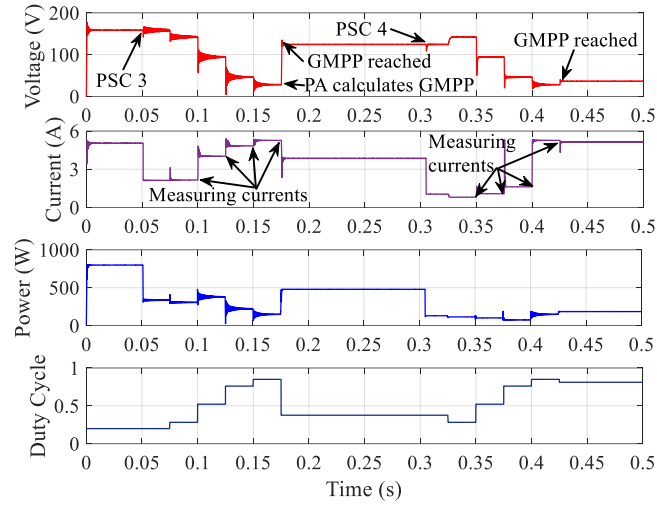


Fig. 4.12. Simulation of the performance of the proposed PA algorithm under PSC patterns 3 and 4.

The proposed PA algorithm as discussed so far uses a single current sensor and a single DC-DC converter per PV string. However, if more than one PV strings are connected in parallel and hardware costs must be minimized, the proposed PA algorithm with a simple modification can work with very high tracking efficiency using only one current sensor and one DC-DC converter for multiple parallel PV strings. The underlying theory can be explained using a 4S2P example with radiations Φ_1 , Φ_2 , Φ_3 , and Φ_4 on one string and Ψ_1 , Ψ_2 , Ψ_3 , and Ψ_4 on another string. The subscripts of Φ and Ψ indicate their ordering of magnitude such that $\Phi_1 > \Phi_2 > \Phi_3 > \Phi_4$ and $\Psi_1 > \Psi_2 > \Psi_3 > \Psi_4$, and do not necessarily indicate module number (i.e., the highest radiation Φ_1 can occur on any of the four modules, not necessarily module 1). These radiations will produce I-V and P-V curves very similar to a 4S2P array with radiations of $(\Phi_1 + \Psi_1)/2$, $(\Phi_2 + \Psi_2)/2$, $(\Phi_3 + \Psi_3)/2$, and $(\Phi_4 + \Psi_4)/2$ on each string. This condition is satisfied for any distribution of radiations between different

strings. Fig. 4.13 illustrates this concept, where the solid lines show the actual I-V and P-V curves when different radiations are on each string (in this case, PSC 2 on one string and PSC 3 on the other), and the dashed lines show the approximated curves assuming $(\Phi_1 + \Psi_1)/2$, $(\Phi_2 + \Psi_2)/2$, etc., on each string (i.e., 1000 W/m^2 , 950 W/m^2 , 635 W/m^2 , and 350 W/m^2). The only required modification to the PA algorithm for dealing with multiple parallel strings is that after the current sensor measures the PV current of the 4S2P system at $3V_{oc,m}$, $2V_{oc,m}$, $V_{oc,m}$, and 30 V , the algorithm must then divide the measured current by the number of parallel strings. Then, as usual, these current values are converted into radiations using (6) to approximate the module-to-module averaged PSC pattern on each string. Then, the PA algorithm calculates the GMPP for this averaged PSC pattern on a single string using (8)-(16), which ultimately becomes the GMPP of the whole array.

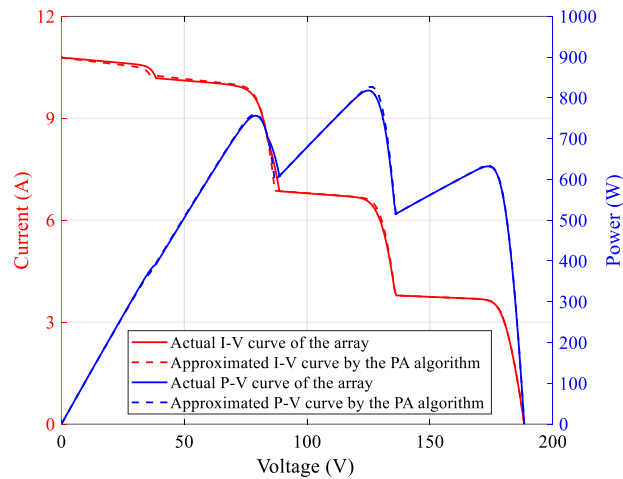


Fig. 4.13. Actual and approximated I-V and P-V characteristic curves for a 4S2P array configuration with PSC patterns 2 and 3.

Fig. 4.14 shows the simulation results of the PA algorithm using a single current sensor for a 4S2P array experiencing PSC pattern 2 on one string and PSC pattern 3 on the other string, where both patterns occur at 0.051 s. The controller measures currents at 0.1 s, 0.125 s, 0.15 s, and 0.175 s, respectively. At 0.175 s, the PA algorithm immediately calculates that the GMPP is at 124.86 V using these four current measurements and (8)-(16). The required duty cycle for the boost converter to operate at input voltage of 124.86 V is calculated as $D=0.3757$ using (17), and immediately set at the converter. The current at this point is 6.53 A, so the tracked input power is 815.34 W. Fig. 4.13 shows that the expected maximum power for these PSC patterns is 818 W. Hence, the tracking efficiency is 99.67%. The PSC is removed at 0.305 s, and the algorithm finds the new tracking power of 1599.68 W, with tracking efficiency of 99.98%. The simulation is repeated for a 4S3P system using PSC patterns 2, 3, and 4 on each string and a tracking efficiency of 99.68% is achieved. Furthermore, simulation results for a 4S4P system using all four PSC patterns shows a tracking efficiency of 98.73%. These results show that when hardware costs must be minimized, the PA algorithm can be considered for use with one current sensor and one DC-DC converter for up to three or possibly four strings in parallel. For high numbers of strings, the tracking efficiency worsens so an additional sensor and converter are recommended.

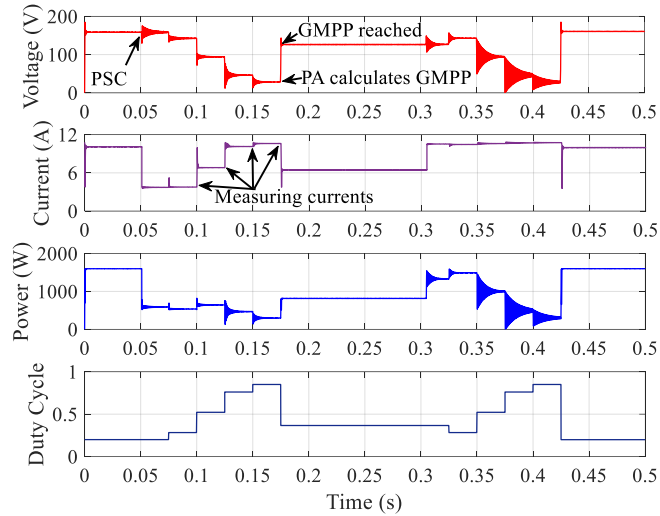


Fig. 4.14. Simulation of the performance of the proposed PA algorithm for a 4S2P configuration under PSC patterns 2 and 3.

4.4.2 Comparison to other MPPT Algorithms

The dynamic performance of the proposed PA algorithm is evaluated using the four PSC patterns connected back-to-back, and compared with three other well-known GMPPT algorithms: particle swarm optimization (PSO) [21], constriction factor PSO (CFPSO) [22], and Modified Hill Climbing (HC) [13]. PSO and CFPSO are population-based optimization methods inspired by the behavior of bird flocks and schooling fish. They generate a population of possible solutions, which are known as particles, and move them around in the search space as per a simple mathematical formula over their position and velocity to solve a problem. The movement of each particle is controlled by its local best-known position, but it is also directed toward the best-known positions in the search space, which are updated when better positions are discovered by other particles. The swarm is predicted to migrate toward the best options because of this. In PSO and CFPSO

based GMPPT algorithms, the duty cycle, D of the DC-DC converter is considered as the position of the particle. The duty cycle resulting in the highest tracked power is known as the best position of the particle. Thus, reaching the best position with highest power needs numerous steps in these optimization-based GMPPT algorithms. Fig. 4.15 shows the simulated dynamic results. The proposed PA algorithm reaches the GMPPT with only four steps compared to PSO with 84 to 149 steps, CFPSO with 71 to 148 steps, and Modified HC with 32 to 45 steps. For the entire simulation time of 20 s, the proposed PA algorithm stores 8397 J of energy, whereas PSO stores 8187 J, CFPSO stores 8094 J, and Modified HC stores 8264 J. Thus, the PA algorithm stores 1.6% to 3.7% more energy than the compared algorithms. Due to the significantly longer converging time of PSO and CFPSO, they are likely to fail to track the GMPPT if the PSC pattern changes before their convergence. In this case, they would need to reinitiate their MPPT processes, which will cause more tracking energy losses. Furthermore, it is well-known that the Modified HC algorithm can fail to scan all the LPs for higher numbers of series connected modules in an array, as explained in the Introduction, meaning finding the GMPP is not guaranteed [39]. Thus, when considering only the compared algorithms that will always find the GMPP, the PA algorithm stores 2.6% to 3.7% more energy during the simulated test.

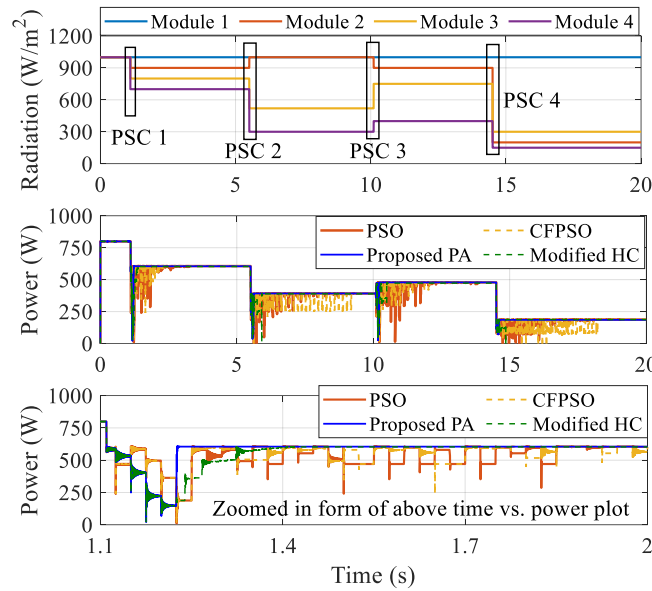


Fig. 4.15. Dynamic performance comparison of the proposed PA, PSO, CFPSO, and Modified HC algorithms under all 4 PSC patterns.

Table 4.4 summarizes the performance of the proposed PA algorithm compared to PSO, CFPSO, Modified HC, and two more popular GMPPT methods, artificial bee colony (ABC) and single sensor hill climbing ABC (SSHC-ABC) from [31], for the same 4S1P PV array configuration in terms of the simulated tracking steps and time, tracking efficiency, voltage track length, tracking energy loss (solar energy lost while trying to get to the GMPP), and sensors needed. ABC and SSHC-ABC are metaheuristic optimization algorithms like PSO and CFPSO, but work based on the food searching process of the bees. The comparison shows that, on average across the different patterns, the proposed PA algorithm is 33 times faster than PSO, 30 times faster than CFPSO, 3 times faster than Modified HC, 17 times faster than ABC, and 10 times faster than SSHC-ABC, while achieving the same or better tracking efficiency and the same or less hardware requirements.

Also, SSHC-ABC is the only other compared method that uses just one sensor, and it achieved an average tracking efficiency of 98.5% across the four PSC patterns, compared to the average PA algorithm tracking efficiency of 99.7%.

Table 4.4. Comparison of Proposed PA Algorithm With Other Methods

PSC Pattern	Method	Tracking Steps	Tracking Time (s)	Tracking Efficiency (%)	Voltage Track Length (V)	Tracking Energy Loss (J)	Sensors Needed
Pattern 1	Proposed PA	4	0.1	99.84	269	27.96	1
	PSO	84	2.1	99.83	755	67.24	2
	CFPSO	71	1.775	99.84	702	57.78	2
	Modified HC	32	0.296	99.42	269	49.28	2
	ABC	24 [31]	1.67 [31]	97.50 [31]	851	217.96	2
	SSHC-ABC	3 [31]	0.26 [31]	98.16 [31]	172	20.29	1
Pattern 2	Proposed PA	4	0.1	99.90	187	16.92	1
	PSO	145	3.625	99.89	990	61.3	2
	CFPSO	147	3.675	99.92	1053	115.54	2
	Modified HC	45	0.39	99.26	379	46.39	2
	ABC	23 [31]	1.62 [31]	99.08 [31]	881	238.14	2
	SSHC-ABC	18 [31]	1.3 [31]	99.13 [31]	811	198.68	1
Pattern 3	Proposed PA	4	0.1	99.67	273	21.44	1
	PSO	149	3.725	99.65	1357	93.10	2
	CFPSO	107	2.675	99.67	1105	60.96	2
	Modified HC	43	0.375	98.75	376	53.4	2
	ABC	24 [31]	1.71 [31]	98.34 [31]	910	238.35	2
	SSHC-ABC	19 [31]	1.33 [31]	99.17 [31]	823	225.86	1
Pattern 4	Proposed PA	4	0.1	99.39	138	7.79	1
	PSO	142	3.55	99.45	1312	81.79	2
	CFPSO	148	3.7	99.41	1351	162.62	2
	Modified HC	37	0.335	99.89	390	22.01	2
	ABC	24 [31]	1.68 [31]	96.85 [31]	929	103.49	2
	SSHC-ABC	18 [31]	1.25 [31]	97.57 [31]	839	79.73	1

4.4.3 Effect of Sensor Noise/Offset

Due to the analytical nature of the proposed PA algorithm, it is important to investigate the effect of sensor noise and offset on the algorithm performance. Sensor noise can be greatly reduced using a digital filter in the microcontroller, and

thus a median/moving average filter has been implemented both in the microcontroller (for the experimental results) and in the Simulink model for the noise/offset analysis. Fig. 4.16 shows the simulated tracking efficiency for the PA, PSO, and CFPSO algorithms under PSC pattern 2 for sensor offset levels of 0, 0.1, and 0.2 V, and sensor signal-to-noise (SNR) values of 10, 20, 30, 40, 50, and 80 dB. Firstly, the results show that the analytical PA algorithm performs similar or better than the optimization-based algorithms of PSO and CFPSO, and thus there is no particular concern regarding sensor noise/offset for the PA algorithm. Secondly, the results show that for all simulated algorithms, high tracking efficiency is achieved for $\text{SNR} > 30$ dB. High-quality current sensors will exceed this requirement; for example [42] describes a complete sensor system using a LEM Hall sensor that achieves $\text{SNR} > 84$ dB. Thirdly, sensor offset of 0.2 V or more causes a significant reduction in tracking efficiency for all simulated algorithms. However, the PA algorithm has high tracking efficiency at 0.1 V sensor offset as long as $\text{SNR} > 30$ dB. Since the LEM Hall sensor in [42] states a current measurement accuracy of 0.5% (which corresponds to a possible offset of 0.025 V on a 5 V signal into the microcontroller) and the LEM LTS15-NP sensor used in this experimental setup [43] has an accuracy of 0.2% (or 0.01 V on a 5 V signal), there are multiple quality current sensors available on the market to maintain an offset of 0.1 V or less.

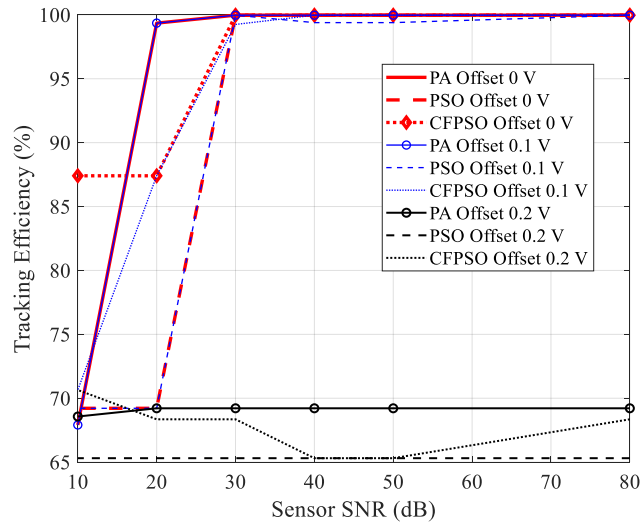


Fig. 4.16. Sensitivity analysis of the proposed PA algorithm compared to PSO and CFPSO for various noise levels and offsets.

4.4.4 Effect of PV Module Aging

Due to the analytical nature of the proposed PA algorithm, it is also important to investigate its performance on aged PV cells. Over time, PV cells experience optical and electrical degradation due to optical and encapsulating losses and deterioration of electrical parts due to temperature [44]. Optical and electrical degradation gradually decreases the effective radiation and increases the module's series resistance, R_s , over time [44]. Durastanti et al. modeled PV module aging in [45], where the effective radiation reduced by 6% and 12% and the series resistance increased by 2.3% and 4.6% after 10 years and 20 years respectively. Following the same aging model approach from [45], Fig. 4.17 shows the P-V characteristic curves of an aged SunPower SPR-200-WHT-U module, with similar

% changes after 10 and 20 years, which has been modeled and simulated with the PA algorithm in Simulink.

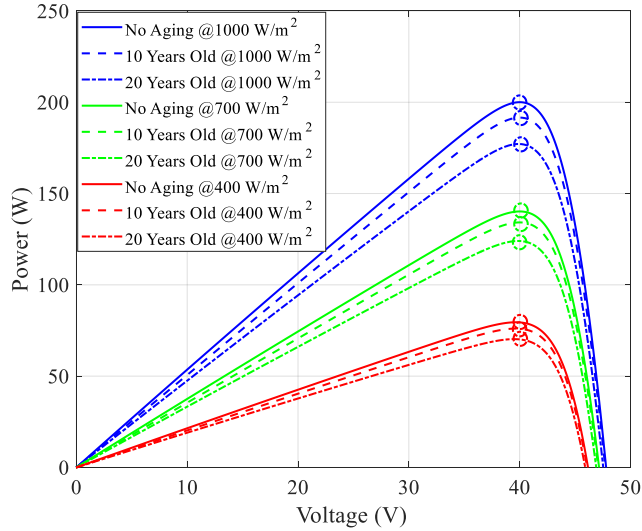


Fig. 4.17. Impact of aging on PV modules over 10 and 20 years of life.

The PA algorithm uses the V_{mpp}/V_{oc} and I_{mpp}/I_{sc} ratios (8) of a new module, so it is important to understand how these ratios may change as the module ages, even as the algorithm continues to use the “new module” values. With regards to the V_{mpp}/V_{oc} ratio, the increase of R_s has minimal impact on the reduction of V_{oc} as the R_s itself is very small as per the manufacturer’s datasheet and Table 4.1. As a result, the MPP positions of the module for various radiations stay almost at the same voltage positions compared to their initial positions for non-aged modules as shown in Fig. 4.17. The change in R_s will slightly affect the I_{mpp}/I_{sc} ratio: for the considered PV module at 20 years aging (4.6% increase in R_s), the new ratio is 0.925, which is 0.1% smaller than the new module ratio of 0.926. Thus, the change

in R_s over time can make a very small decrease in PA algorithm tracking efficiency for some PSC patterns.

Table 4.5. Tracking Efficiency (%) Comparison of The Proposed PA Algorithm For Non-Aged And Aged PV Modules

PSC Pattern	Non-aged	10 Years Old	20 Years Old
Pattern 1	99.84	99.92	99.90
Pattern 2	99.92	99.90	99.92
Pattern 3	99.67	99.92	99.82
Pattern 4	99.39	99.19	99.08

The other aging effect, a reduction in radiation, does not affect the PA algorithm tracking efficiency because the V_{mpp}/V_{oc} and I_{mpp}/I_{sc} ratios remain the same. The reduction in radiation will mean the PA algorithm is not correctly calculating the values of the incident radiations, but it will calculate the change of radiation correctly, and sense the presence of PSC accurately. As it is not the radiation, but rather the current which is used in the PA algorithm's equations to calculate the LP positions, this radiation reduction does not affect the algorithm's ability to find the GMPP. The simulation results shown in Fig. 4.18 illustrate this point for a 4S1P 20 year aged PV array subjected to PSC patterns 1 and 2. After experiencing PSC 1 at 0.051 s, the controller measures the currents as 3.32 A, 3.8 A, 4.29 A, and 4.68 A at 0.1 s, 0.125 s, 0.15 s, and 0.175 s, respectively. At 0.175 s, the controller converts these currents into radiations using (6), which are 614.81 W/m², 703.7 W/m², 794.44 W/m², and 866.67 W/m², respectively. The PSC pattern 1 has the actual radiation values of 700 W/m², 800 W/m², 900 W/m², and 1000 W/m². Though the calculated radiations are not correct, the sensed current is used in the PA algorithm's equations to find the LP, so the PA algorithm still achieves

excellent tracking efficiency for aged modules, as shown in Table 4.5. The tracking efficiency is over 99% for the simulated PSCs for 10 and 20 year aged cells, thus the PA algorithm can work effectively for aged PV modules.

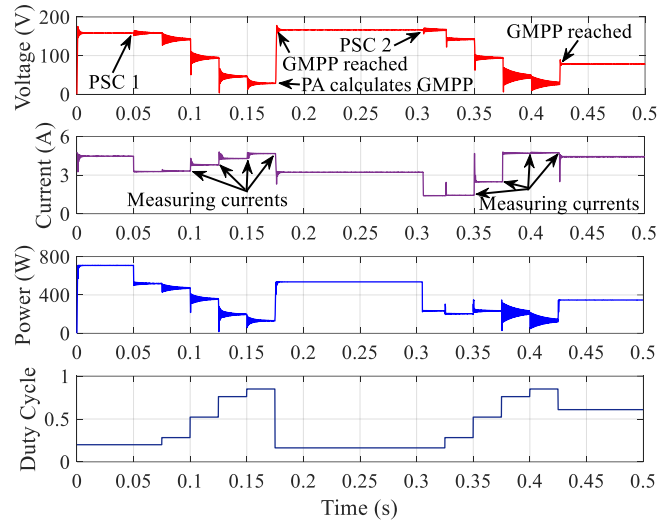


Fig. 4.18. Simulation of the performance of the proposed PA algorithm for a 4S1P configuration consisting of 20 years old modules under PSC patterns 1 and 2.

4.5. Experimental Results

Fig. 4.19 shows a diagram of the experimental setup used to evaluate the performance of the PA algorithm. Due to the unavailability of a high voltage battery in the lab, a DC load and a DC voltage supply are connected at the output of the boost converter as shown in Fig. 4.19 to mimic the steady voltage performance of a battery. The resistance of the DC load is set such that the current requirement of the resistance is higher than the maximum output current of the boost converter. Hence, the additional current required is provided by the DC voltage supply. A protection diode is connected in series with the DC supply so that no current flows back into the supply. Fig. 4.20 shows the experimental setup. The main components

include a solar array simulator (SAS) (ITECH IT6523C), hall effect current sensor with excellent noise rejection (LTS 15-NP), boost converter (KIT-CRD-3DD12P), DC electronic load (ITECH IT8906E-600-420), microcontroller (TMS320F28379D), and DC voltage supply (Sorensen SGX 600-25). The experiment is carried out with the same switching frequency as the simulation (40 kHz).

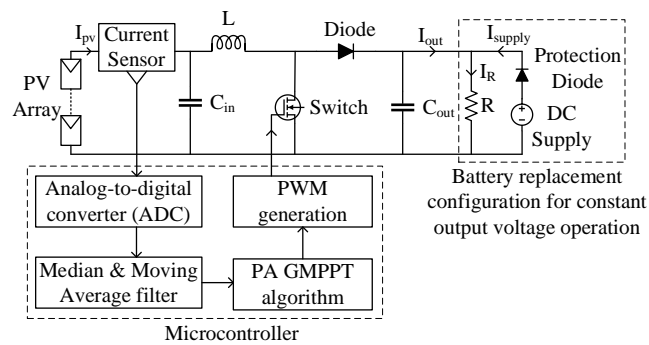


Fig. 4.19. Experimental setup with alternate configuration for steady output voltage operation.

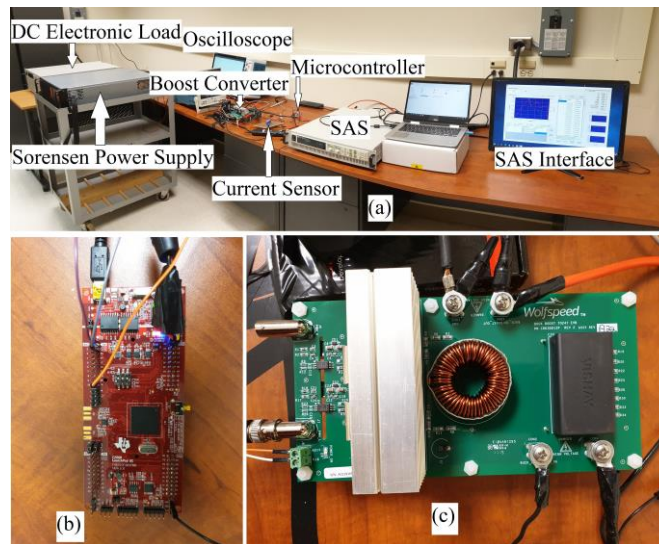


Fig. 4.20. (a) Experimental Setup, (b) TMS320F28379D Microcontroller, and (c) Boost Converter Evaluation Board KIT-CRD-3DD12P.

To experimentally validate the proposed PA GMPPT algorithm, the simulated PSC patterns are implemented in the SAS. In Fig. 4.21, PSC pattern 1 is applied to the SAS at 2.02 s. The microcontroller samples the input PV current every 0.15 s from the current sensor. This step time is longer than that used in simulation (0.025 s) to ensure enough time for the input current provided by the SAS to stabilize after a duty cycle change. As the SAS is not a real solar array, it emulates the behavior of a solar array by providing current with respect to voltage using I-V and P-V characteristic lookup tables, making the current response slower. Had it been a real solar array instead of the SAS, the current would have reached the steady state value much faster similar to [13]. Thus, a 0.15 s step time is used in the experiment to allow settling time for the SAS current, but the number of duty cycle steps required, the critical factor, is still shown to be four for a 4S1P system. As all conventional and contemporary GMPPT algorithms require significantly more steps compared to the proposed PA algorithm, they will all exhibit slower tracking time if implemented on the same hardware.

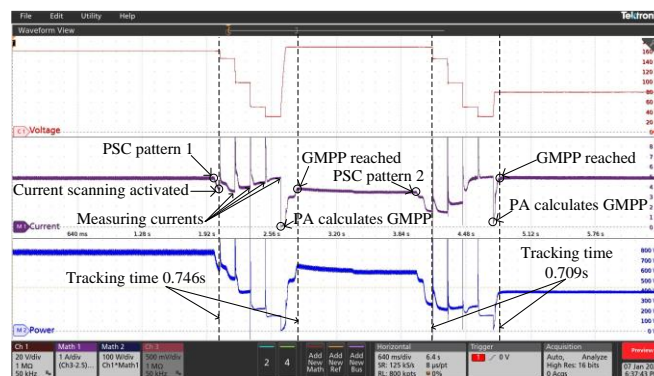


Fig. 4.21. Experimental performance of the proposed PA algorithm under PSC patterns 1 and 2.

In Fig. 4.21, from the difference between measured currents at 1.9 s and 2.05 s, the controller detects the occurrence of shading and initiates current scanning at $3V_{oc,m}$, $2V_{oc,m}$, $V_{oc,m}$, and 30 V. Using these current values, the controller confirms a PSC at 2.65 s, the PA algorithm calculates the GMPP immediately, and the controller applies the required duty cycle at the boost converter. Though the input voltage of the boost converter stabilizes at the GMPP voltage quickly at 2.703 s, the SAS takes a comparatively longer time to stabilize the input current, at 2.796 s in this case. Thus, the system, including the delayed SAS current response, takes 0.746 s to reach the new GMPP with a tracked maximum power of 605.6 W and a 99.87% tracking efficiency. At 4.02 s, PSC pattern 2 is applied at the SAS. The controller senses the change in radiation from the difference between sampled currents at 4 s and 4.15 s and initiates current scanning at the four previously defined voltage points. Using these sampled current values, the PA algorithm calculates the GMPP position at 4.75 s and the controller applies the required duty cycle at the boost converter immediately. The GMPP voltage is reached at 4.767 s and the GMPP current from the SAS stabilizes at 4.859 s with a tracking time of 0.709 s, tracked power of 391.82 W, and a 99.95% tracking efficiency.

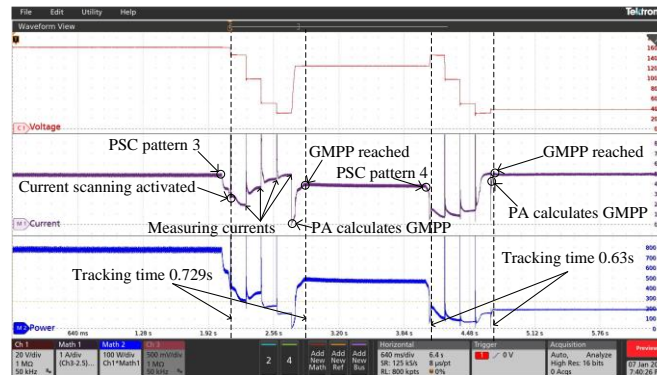


Fig. 4.22. Experimental performance of the proposed PA algorithm under PSC patterns 3 and 4.

Fig. 4.22 shows the performance of the PA algorithm for PSC patterns 3 and 4. Again, the PA algorithm takes only four steps to reach the GMPP for both pattern 3 and 4, which are actually the four current measurements required anyways to determine if PSC has occurred. Fig. 4.23 shows an example of the voltage, current, and efficiency from the SAS interface after the PA algorithm has tracked the GMPP under PSC pattern 2. Table 4.6 summarizes the performance of the proposed algorithm for both simulation and experiment in terms of tracking time, tracking power, tracking efficiency, tracking energy loss, and voltage track length for all four patterns. The results show extremely high experimental tracking efficiencies ($>99.6\%$ for all PSC patterns tested), and fast tracking times due to the fixed number of four measurement steps for a 4S1P system.

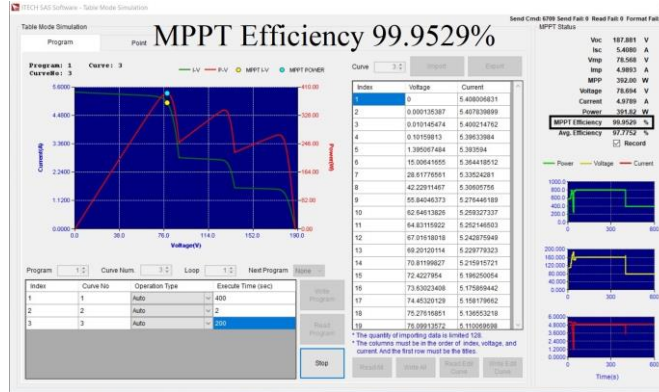


Fig. 4.23. Example of voltage, current, and efficiency profile from SAS interface.

Table 4.6. Experimental Results of The Proposed PA GMPPT Algorithm

PSC Pattern	Method	Tracking Time (s)	Tracked Power (W)	Maximum Power (W)	Tracking Efficiency (%)	Voltage Track Length (V)	Tracking Energy Loss (J)
Pattern 1	Simulation	0.1	605.4	606.4	99.84	269	27.96
	Experiment	0.746	605.6		99.87	270	128.66
Pattern 2	Simulation	0.1	391.5	392	99.90	187	16.92
	Experiment	0.709	391.82		99.95	186	109.653
Pattern 3	Simulation	0.1	477.3	478.9	99.67	273	21.44
	Experiment	0.729	477.1		99.62	223	136.35
Pattern 4	Simulation	0.1	186.85	188	99.39	138	7.79
	Experiment	0.630	187.38		99.67	143	35.29

4.6. Conclusion

This chapter proposes a totally new approach to finding the GMPP during PSC using a single current sensor: the PA GMPPT algorithm uses a fixed number of current scans (steps) equal to the number of solar modules connected in series to directly and immediately calculate the GMPP, in contrast to the other contemporary algorithms including optimization-based search methods that have significantly longer convergence times. The PA GMPPT algorithm uses simple parabolic equations to calculate the GMPP near-exactly during PSC. The tracking energy loss during scanning is negligible because of the low number of scans and no blind

scans. Only a few mathematical equations make this algorithm computationally inexpensive enough to be implemented on a simple microcontroller. A single current sensor reduces overall system cost and complexity. Both simulation and experimental results confirm that the PA GMPPT algorithm achieves a new standard of fast tracking time with a fixed number of steps (on average, 10 to 33 times faster than other methods guaranteed to find the GMPPT), while also achieving excellent tracking efficiency and a low sensor requirement, and thus outperforms other contemporary GMPPT algorithms. The proposed PA algorithm is an excellent choice for fast-moving applications such as SEVs.

Chapter 4 References

- [1] A. Bidram, A. Davoudi, and R. S. Balog, "Control and circuit techniques to mitigate partial shading effects in photovoltaic arrays," *IEEE J. Photovolt.*, vol. 2, no. 4, pp. 532-546, Oct. 2012.
- [2] P. Van den Heever, S. Oberholzer, and J. Enslin, "High-efficient solar panel/wind turbine converter with maximal power control," in *Proc. Eur. Conf. Power Electron. Appl.*, 1989, pp. 663-668.
- [3] Teodorescu et al., "On the perturb-and-observe and incremental conductance MPPT methods for PV systems," *IEEE J. Photovolt.*, vol. 3, no. 3, pp. 1070-1078, Jul. 2013.
- [4] E. Koutroulis and F. Blaabjerg, "A new technique for tracking the global maximum power point of PV arrays operating under partial-shading conditions," *IEEE J. Photovolt.*, vol. 2, no. 2, pp. 184-190, Apr. 2012.
- [5] S. Daraban, D. Petreus, C. Morel, and M. Machmoum, "A novel global MPPT algorithm for distributed MPPT systems," in *Proc. 15th Eur. Conf. Power Electron. Appl.*, Lille, France, 2-6 Sept. 2013, pp. 1-10.
- [6] Perreault et al., "Submodule integrated distributed maximum power point tracking for solar photovoltaic applications," *IEEE Trans. Power Electron.*, vol. 28, no. 6, pp. 2957-2967, Jun. 2013.
- [7] Ahmed et al., "A switched PV approach for extracted maximum power enhancement of PV arrays during partial shading," *IEEE Trans. Sustain. Energy*, vol. 6, no. 3, Jul. 2015.
- [8] El-Saadany et al., "Enhanced reconfig. method for reducing mismatch losses in PV systems," *IEEE J. Photovolt.*, vol. 7, no. 6, Nov. 2017.
- [9] Tahmasbi-Fard et al., "A vol. equalizer circuit to reduce partial shading effect in photovoltaic string," *IEEE J. Photovolt.*, vol. 8, no. 4, Jul. 2018.
- [10] H. Delavaripour, B. Dehkordi, H. Zarchi, and E. Adib, "Increasing energy capture from partially shaded PV string using differential power processing," *IEEE Trans. Ind. Electron.*, vol. 66, no. 10, Oct. 2019.
- [11] R. López-Erauskin, A. González, G. Petrone, G. Spagnuolo, and J. Gyselinck, "Multi-Variable Perturb and Observe Algorithm for Grid-Tied PV Systems With Joint Central and Distributed MPPT Configuration," *IEEE Trans. Sustain. Energy*, vol. 12, no. 1, pp. 360-367, Jan. 2021.
- [12] Y. Mahmoud and E. F. El-Saadany, "A Novel MPPT Technique Based on an Image of PV Modules," *IEEE Trans. Energy Conv.*, vol. 32, no. 1, pp. 213-221, March 2017.

- [13] Farhangi et al., "Global maximum power point tracking method for photovoltaic arrays under partial shading conditions," *IEEE Trans. Ind. Electron.*, vol. 64, no. 4, pp. 2855-2864, Apr. 2017.
- [14] B. Lin, L. Wang, and Q. Wu, "Maximum Power Point Scanning for PV Systems Under Various Partial Shading Conditions," *IEEE Trans. Sustain. Energy*, vol. 11, no. 4, pp. 2556-2566, Oct. 2020.
- [15] Huang et al., "A novel spline model guided maximum power point tracking method for photovoltaic systems," *IEEE Trans. Sustain. Energy*, vol. 11, no. 3, Jul. 2020.
- [16] G. Escobar, C. Ho, and S. Pettersson, "Maximum power point searching method for partial shaded PV strings," in *Proc. 38th Annu. Conf. IEEE Ind. Electron. Soc.*, 2012, pp. 5726-5731.
- [17] Y. Wang, Y. Li, and X. Ruan, "High accuracy and fast speed MPPT methods for PV string under partially shaded conditions," *IEEE Trans. Ind. Electron.*, vol. 63, no. 1, pp. 235-245, Jan. 2016.
- [18] M. Ghasemi, H. Forushani, and M. Parniani, "Partial shading detection and smooth maximum power point tracking of PV arrays under PSC," *IEEE Trans. Power Electron.*, vol. 31, no. 9, pp. 6281-6292, Sep. 2016.
- [19] Berkouk et al., "A high-performance global maximum power point tracker of PV system for rapidly changing partial shading condition," *IEEE Trans. Ind. Electron.*, vol. 68, no. 3, pp. 2236-2245, Feb. 2020.
- [20] Yu et al., "An overall distribution particle swarm optimization MPPT algorithm for photovoltaic system under partial shading," *IEEE Trans. Ind. Electron.*, vol. 66, no. 1, Jan. 2019.
- [21] C. Manickam, G. R. Raman, G. P. Raman, S. I. Ganesan, and C. Nagamani, "A Hybrid Algorithm for Tracking of GMPP Based on P&O and PSO With Reduced Power Oscillation in String Inverters," *IEEE Trans. Ind. Electron.*, vol. 63, no. 10, pp. 6097-6106, Oct. 2016.
- [22] S. Obukhov, A. Ibrahim, A. A. Zaki Diab, A. S. Al-Sumaiti, and R. Aboelsaud, "Optimal Performance of Dynamic Particle Swarm Optimization Based Maximum Power Trackers for Stand-Alone PV System Under Partial Shading Conditions," *IEEE Acc.*, vol. 8, pp. 20770-20785, 2020.
- [23] Sundareswaran et al., "Enhanced energy output from a PV system under partial shaded conditions through artificial bee colony," *IEEE Trans. Sustain. Energy*, vol. 6, no. 1, pp. 198-209, Jan. 2015.
- [24] A. A. S. Mohamed, A. Berzoy, and O. A. Mohammed, "Design and Hardware Implementation of FL-MPPT Control of PV Systems Based on GA and Small-

- Signal Analysis," *IEEE Trans. Sustain. Energy*, vol. 8, no. 1, pp. 279-290, Jan. 2017.
- [25] Sampaio et al, "Comparative analysis of MPPT algorithms bio-inspired by grey wolves employing a feedforward control loop in a three-phase grid connected photovoltaic system," *IET Ren. Pow. Gen.*, Mar. 2019.
- [26] Pachaiyannan et al., "Crowded plant height optimisation algorithm tuned maximum power point tracking for grid integrated solar power conditioning system," *IET Ren. Pow. Gen.*, Jun. 2019.
- [27] Tey et al., "Improved team game optimization algorithm based solar MPPT with fast convergence speed and fast response to load variations," *IEEE Trans. Ind. Electron.*, Early Access, Jun. 2020.
- [28] Y. -P. Huang, M. -Y. Huang, and C. -E. Ye, "A Fusion Firefly Algorithm With Simplified Propagation for Photovoltaic MPPT Under Partial Shading Conditions," *IEEE Trans. Sustain. Energy*, vol. 11, no. 4, pp. 2641-2652, Oct. 2020.
- [29] Yousri et al., "A novel chaotic flower pollination algorithm for global maximum power point tracking for photovoltaic system under partial shading conditions," *IEEE Acc.*, Sept. 2019.
- [30] L. Chen and X. Wang, "Enhanced MPPT method based on ANN assisted sequential Monte-Carlo and quickest change detection," *IET Smart Grid*, Sept. 2019.
- [31] J. Goud, R. Kalpana, and B. Singh, "A hybrid global maximum power point tracking technique with fast convergence speed for partial-shaded PV systems," *IEEE Trans. Ind. Appl.*, vol. 54, no. 5, Sep./Oct. 2018.
- [32] D. S. Pillai, J. P. Ram, A. M. Y. M. Ghias, M. A. Mahmud, and N. Rajasekar, "An Accurate, Shade Detection-Based Hybrid Maximum Power Point Tracking Approach for PV Systems," *IEEE Trans. Power Electron.*, vol. 35, no. 6, pp. 6594-6608, June 2020.
- [33] M. H. Mobarak, R. N. Kleiman and J. Bauman, "Solar-Charged Electric Vehicles: A Comprehensive Analysis of Grid, Driver, and Environmental Benefits," *IEEE Trans. Transp. Elec.*, vol. 7, no. 2, pp. 579-603, June 2021.
- [34] A. Diab-Marzouk and O. Trescases, "SiC-based bidirectional cuk converter with differential power processing and MPPT for a solar powered aircraft," *IEEE Trans. Transp. Elec.*, vol. 1, pp. 369-381, 2015.
- [35] F. Pai, R. Chao, S. H. Ko, and T. Lee, "Performance Evaluation of Parabolic Prediction to Maximum Power Point Tracking for PV Array," *IEEE Trans. Sustain. Energy*, vol. 2, no. 1, pp. 60-68, Jan. 2011.

- [36] N. Femia, D. Granozio, G. Petrone, G. Spagnuolo, and M. Vitelli, "Predictive & Adaptive MPPT Perturb and Observe Method," *IEEE Trans. Aerospace and Electron. Sys.*, vol. 43, no. 3, pp. 934-950, July 2007.
- [37] R. Li and Z. Tan, "Study on Maximum Power Point Tracking Based on Parabolic Approximation Method for Photovoltaic Power Generation System," *2018 37th Chinese Control Conference (CCC)*, 2018, pp. 7570-7574.
- [38] J. Ahmed and Z. Salam, "An accurate method for MPPT to detect the partial shading occurrence in a PV system," *IEEE Trans. Ind. Infor.*, vol. 13, no. 5, Oct. 2017.
- [39] J. Ahmed and Z. Salam, "An enhanced adaptive P&O MPPT for fast and efficient tracking under varying environmental conditions," *IEEE Trans. Sustain. Energy*, vol. 9, no. 3, Jul. 2018.
- [40] P. Lei, Y. Li, and J. E. Seem, "Sequential ESC-based global MPPT control for photovoltaic array with variable shading," *IEEE Trans. Sustain. Energy*, vol. 2, no. 3, pp. 348-358, Jul. 2011.
- [41] Sawada et al., "A study of a two stage maximum power point tracking control of a photovoltaic system under partially shaded insolation conditions," *Sol. Energy Mater. Sol. Cells*, vol. 90, pp. 2975-2988, 2006.
- [42] Reference Design for Interfacing Current Output Hall Sensors and CTs With Differential ADCs/MCUs, *TI Designs*. Available Online: https://www.ti.com/lit/ug/tidua57a/tidua57a.pdf?ts=1619541472041&ref_url=https%253A%252F%252Fwww.google.com%252F
- [43] Current Transducer LTS 15-NP, *LEM*. Available Online: https://www.lem.com/sites/default/files/products_datasheets/lts_15-np.pdf
- [44] S. Santos, J. Torres, C. Fernandes, and R. Lameirinhas, "The impact of aging of solar cells on the performance of photovoltaic panels," *Energy Conversion and Management: X*, vol. 10, 2021, 100082.
- [45] Durastanti et al., "Impact of the aging of a photovoltaic module on the performance of a grid-connected system," *Solar Energy*, vol. 174, pp. 445-454, 2018.

Chapter 5: Optimization of PV Array and Power Electronics Design for On-Vehicle Solar Charging

5.1. Introduction

As Chapter 4 provides a fast-converging solution to the maximum power extraction problem for a fast-moving SEV, two major issues still need to be addressed to ensure the solar energy reaches the storage battery with highest efficiency. One of them is the selection of the optimum power electronic architecture that the PV energy must use to flow from PV panel to storage. As PV voltages are generally low, boosting the PV voltage to the high traction battery voltage, varying between 250 V and 450 V becomes a real power electronic challenge. Though the existing 12 V battery path can be used for solar energy capture, the energy capacity of these batteries is not sufficient to store solar energy gathered over long periods of time. Thus, the two potential strategies as shown in Fig. 5.1 [1] are: (1) using a low number of cells in series to keep the voltage low and reuse the bidirectional high-voltage to 12 V DC-DC converter that generally is present in most EVs, or (2) connecting more cells in series to create higher PV voltages and boosting the voltage to the 250-450V range using dedicated DC-DC converters.

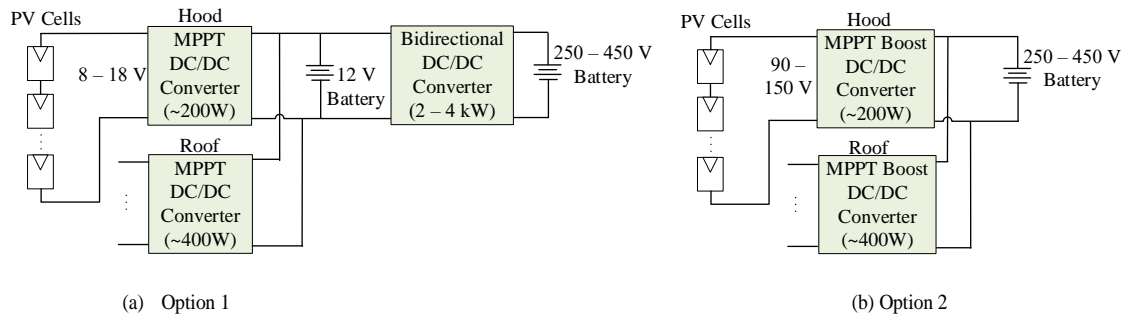


Fig. 5.1. Two potential electrical architecture options for the proposed SEV [1].

Option 1 reduces the cost as the existing DC-DC converter is used for boosting the voltage to the traction battery voltage range. But the efficiency is expected to be lower as higher currents occur in each MPPT converter due to the lower input voltage, the high-power (2-4 kW) existing bidirectional DC-DC converter being used at the 200-600 W level, and two DC-DC converters processing the power before reaching the traction battery. Option 2 may result in higher efficiency as the dedicated DC-DC converters will be of higher efficiency due to less voltage boost required. Nevertheless, the high step-up dedicated MPPT boost converters in this case will incur additional cost compared to Option 1. Thus, this is crucial to determine the optimum power electronic architecture for PV energy accumulation.

Another major issue is to determine the optimum PV interconnections, i.e., how many cells should be connected in series and parallel. Larger cell sizes result in fewer interconnections, but a lower voltage is produced from such a string of cells. This low voltage requires high boost to the traction battery voltage, which generally leads to poor efficiency. More cells in series may boost the resulting voltage, but any shading in the series string will reduce the solar power for the entire

string. Though the major portion of the solar energy may be obtained while the vehicle is parked, an optimal design is required for maximum solar power production even when vehicle body is partially in the shade. Previous research on deciding series parallel interconnection [2] only compares the extracted power difference for stationary and moving vehicle between two configurations, i.e., either connecting all cells in series or in parallel based on fixed cell size available at the market. Though connecting all the cells in parallel shows higher solar energy extraction in this research, the practical implementation is limited as a separate boost converter will be required with each cell to boost the voltage, resulting in higher cost. Also, this research has not taken the effect of MPPT DC-DC converter efficiency into account.

Larger PV cell sizes will result in higher PV currents with a fixed PV voltage and connecting the cells in series will increase the PV voltages [1]. Various combinations of these input voltage and current along with a fixed output voltage at the DC-DC converter connected to a battery will result in different efficiency values. Thus, it is extremely important to determine the optimum cell size and optimum number of such cells in series and parallel taking the effect of the power electronic converter efficiency. Thus, this chapter carries out a system level analysis of the two PV architectures shown in Fig. 5.1 to find out the optimum power electronic architecture for maximum PV energy accumulation. Based on this power electronic architecture, this chapter also uniquely determines the optimum PV cell size and optimum number of such cells in series and parallel using offline genetic

algorithm (GA) to ensure maximum power extraction, specially, in case of partial shading.

Section 5.2 models and determines the optimum power electronic architecture from Fig. 1, section 5.3 explains cell size and interconnection optimization based on DC-DC converter efficiency modeling, section 5.4 shows the simulation results using GA for the optimum cell size and their optimum numbers in series-parallel interconnection with the effect of DC-DC converter efficiency, and section 5.5 concludes this chapter.

5.2. Optimum Power Electronic Architecture Selection

To carry out a system level analysis to determine the optimum power electronic architecture from Fig. 5.1, a SEV with CIGS PV cells with a current density of $J=380 \text{ A/m}^2$ is considered. Specifications of this cell are described in Table 5.1.

Table 5.1. Specifications of the considered CIGS PV cell.

Parameters	Variable	Value	Unit
Current density	J	380	A/m^2
Cell size (square)	$cell_dimension$	Variable (1 to 20)	mm
Cell open-circuit voltage	$V_{oc,cell}$	0.7	V
Short-circuit current	I_{sc}	$J * cell_dimension^2$	A
MPP voltage to open circuit voltage ratio	$V_{mpp,cell} / V_{oc,cell}$	0.82	N/A
MPP current to short circuit current ratio	I_{mpp} / I_{sc}	0.93	N/A
Temperature coefficient of V_{oc}	K_v	-0.36	$\%/^{\circ}\text{C}$
Temperature coefficient of I_{sc}	K_I	0.02	$\%/^{\circ}\text{C}$
Diode saturation current	I_0	1.8898e-10	A
Diode ideality factor	a	1.1287	N/A

The cell dimension inside the SEV PV panels has been considered a value similar to that of a PV cell currently available at the market [3], i.e., 125mm. The roof area of the Chevy SEV is assumed to be 2.33 m^2 , with a length of 1.79 m and a width of 1.302 m. Similarly, the hood area is 1.05 m^2 with a length of 0.81 m and

a width of 1.302 m. The roof mounted PV panel has a configuration of 2S1P with each module having 75 cells in series, and the hood mounted PV panel has that of 1S1P with each module having 67 cells in series. The array specifications are given in Table 5.2.

Table 5.2. Specifications of the upward facing PV panels.

Parameters	Variable	Value	Unit
Cell size (square)	<i>cell_dimension</i>	125	mm
Cells per module on roof	<i>n_{c_roof}</i>	75	N/A
Roof PV configuration	N/A	2S1P	N/A
Cells per module on hood	<i>n_{c_hood}</i>	67	N/A
Hood PV configuration	N/A	1S1P	N/A

For Option 1, a buck converter connected to the 12 V bus is assumed to perform the MPPT task. Both roof-mounted and hood-mounted PV panels have separate buck converters. The average efficiency of this converter is assumed to be 94% [1]. A GaN HEMT based bidirectional converter with a rated power of 1kW has been considered [4]. The efficiency map is shown in Fig. 5.2. The architecture is arranged such that if the PV power is higher than the electrical accessories power requirement, the remaining power will flow to the 400 V battery from the 12 V bus. If the accessories power requirement is higher than the available PV power, the 400 V battery will provide power to the 12 V bus through the bidirectional converter.

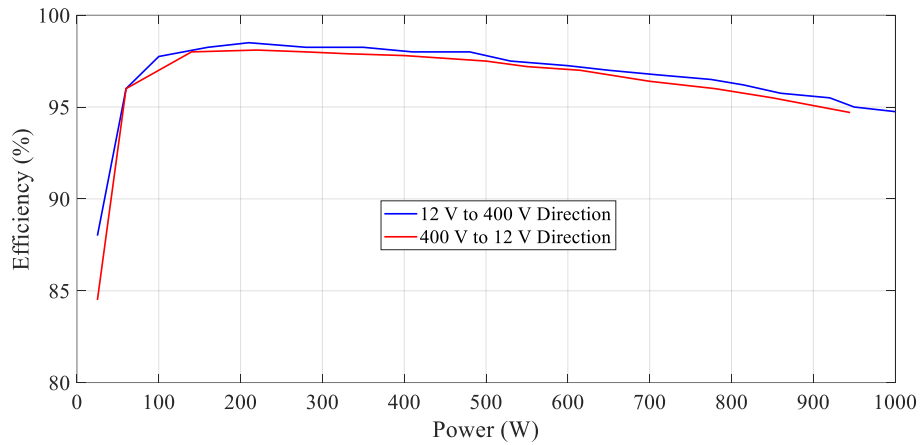


Fig. 5.2. Efficiency map for bidirectional converter in Option 1.

Option 2 uses dedicated MPPT Boost converters connected to the 400 V bus to extract the PV energy. Both roof-mounted and hood-mounted PV panels have separate boost converters. The efficiency maps for boost converters connected to roof-mounted and hood-mounted PV panels are given in Figs. 5.3 and 5.4 respectively [5].

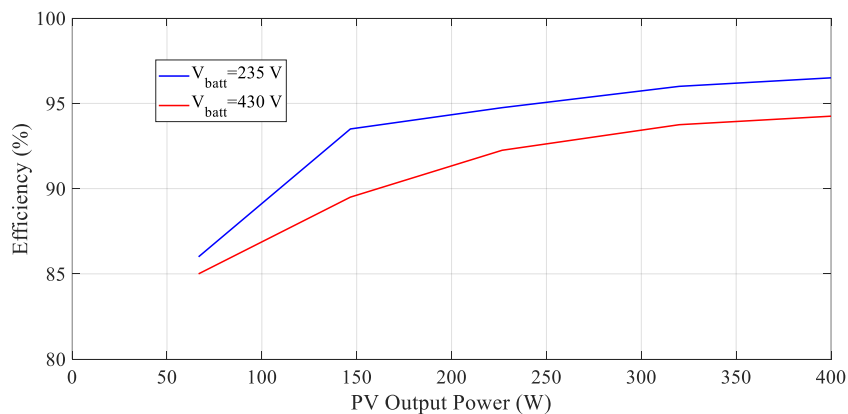


Fig. 5.3. Efficiency map for dedicated boost converter in Option 2 (Rooftop PV).

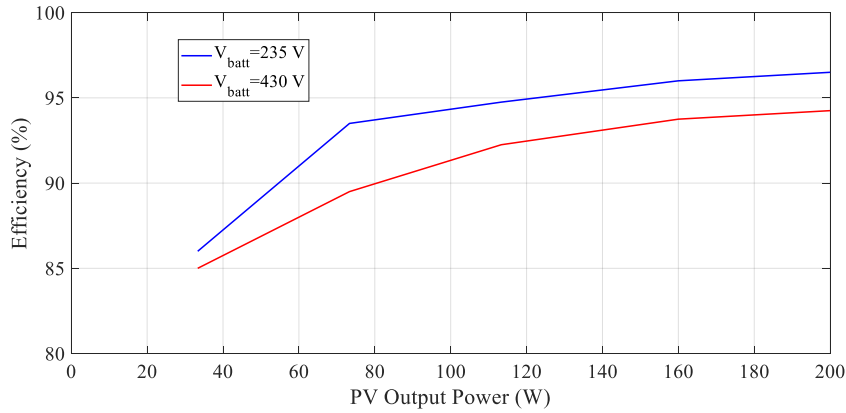


Fig. 5.4. Efficiency map for dedicated boost converter in Option 2 (Hood top PV).

Fig. 5.5 shows the monthly solar radiation and temperature in Los Angeles. Fig. 5.6 shows the simulation performance of the two considered power electronic architectures for a SEV driving in Los Angeles on a day in June with average sky conditions. The electrical accessories power is considered 400 W. At the end of the day, the remaining SOC of the battery is 56.76% for the Option 1 architecture and 56.77% for the Option 2 architecture, taking the effect of temperature on PV cells

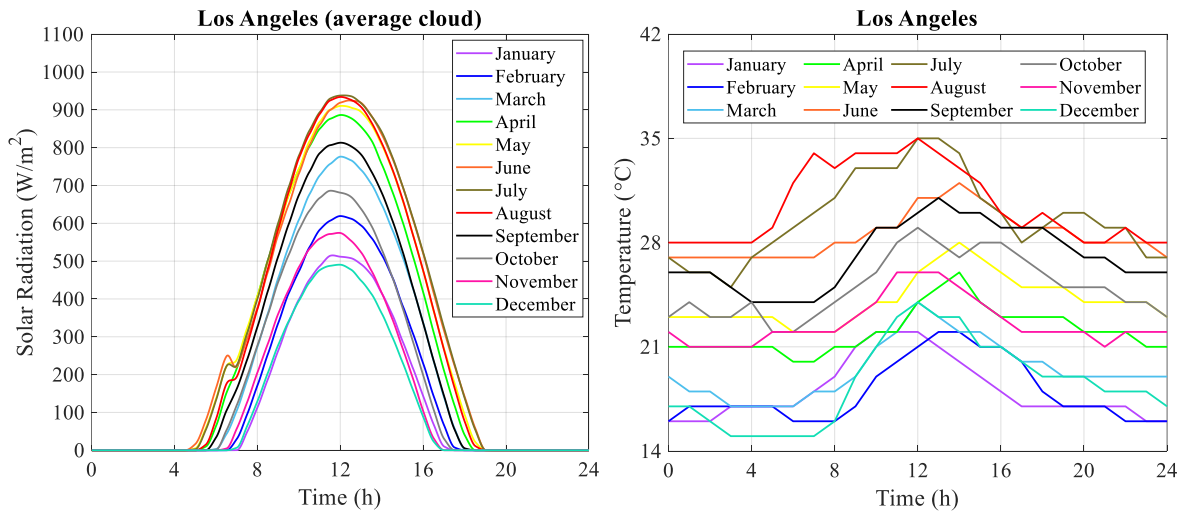


Fig. 5.5. Monthly solar radiation and temperature in Los Angeles.

into account, as shown in Fig. 3.12. This analysis indicates that the Option 1 with the advantage of reusing the existing bidirectional converter is definitely a promising architecture, with efficiency comparable to Option 2 and with the advantage of lower cost. Therefore, it is imperative to determine the cell size and their numbers in series-parallel interconnection in the PV panels with efficiency modeling of the buck converter used in this architecture.

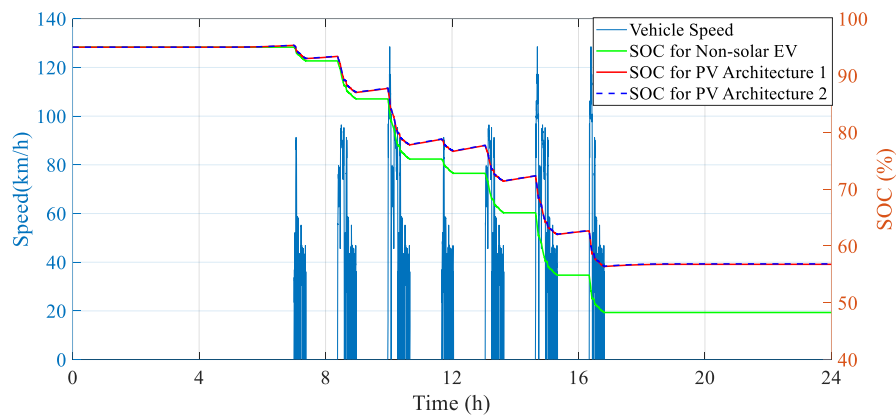


Fig. 5.6. Performance comparison of the two considered PV architectures.

5.3. Cell Size and Interconnection Optimization

5.3.1 Partial Shading Condition (PSC) Modeling on SEV

Fig. 4.3 shows the effect of partial shading on PV power generation. Due to various PSCs, the maximum power voltage and current also varies. Eventually, the efficiency of the DC-DC converter also varies. Fig. 5.7 shows a modeled PSC that is considered to cover part of the hood and roof of a SEV in LA, as shown in Fig. 5.8.

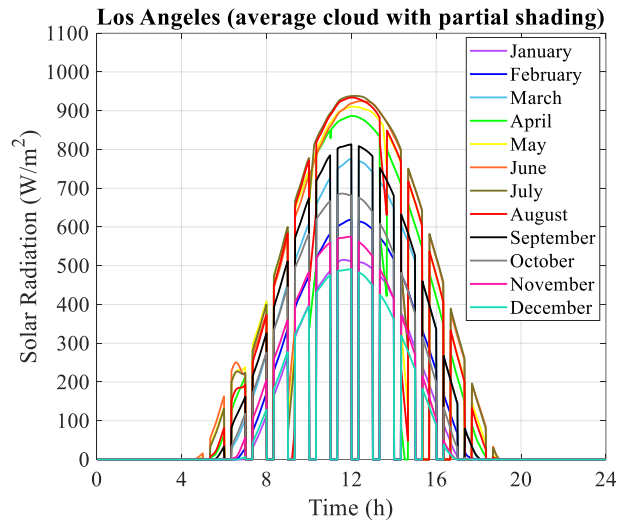


Fig. 5.7. Monthly partial shading solar radiation models for Los Angeles.

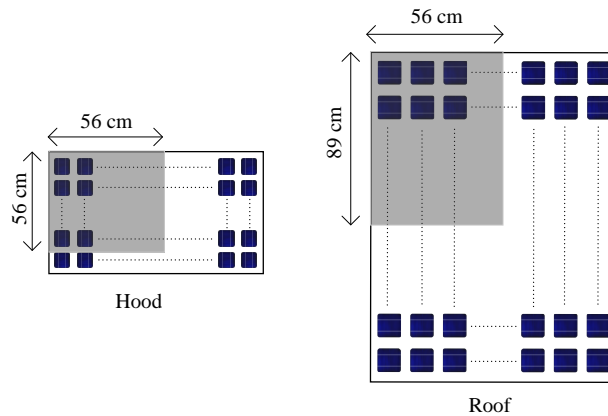


Fig. 5.8. Simplified roof and hood of a SEV.

Fig. 5.8 shows simplified roof and hood of the SEV. The 56cmX89cm area of the roof and 56cmX56cm area of the hood are assumed to have PSC profiles as shown Fig. 5.7. The rest of the areas will continue to have radiation profiles as shown in Fig. 5.5.

5.3.2 DC-DC Converter Efficiency Modeling

This section models the efficiency of a synchronous buck DC-DC converter in Option 1 by calculating corresponding losses.

- High-side MOSFET conduction loss [6]:

$$P_{on_h} = (i_{out}^2 + \frac{\Delta i_L^2}{12}) R_{on_h} \frac{v_{out}}{v_{in}} \quad (1)$$

- Low-side MOSFET conduction loss [6]:

$$P_{on_l} = (i_{out}^2 + \frac{\Delta i_L^2}{12}) R_{on_l} (1 - \frac{v_{out}}{v_{in}}) \quad (2)$$

Here, current ripple [6]:

$$\Delta i_L = \frac{v_{out}(v_{in} - v_{out})}{v_{in} f_{sw} L} \quad (3)$$

- High-side switching loss [6]:

$$P_{sw_h} = 0.5 v_{in} i_{out} (t_{r_h} + t_{f_h}) f_{sw} \quad (4)$$

- Low-side switching loss [6]:

$$P_{sw_l} = 0.5 v_D i_{out} (t_{r_l} + t_{f_l}) f_{sw} \quad (5)$$

- Reverse recovery loss [6]:

$$P_{diode} = 0.5 v_{in} i_{rr} t_{rr} f_{sw} \quad (6)$$

- Output capacitance loss in the MOSFET [6]:

$$P_{\cos s} = 0.5(C_{oss_l} + C_{oss_h})v_{in}^2 f_{sw} \quad (7)$$

- Dead time loss [6]:

$$P_{dead} = v_D i_{out} (t_{d_r} + t_{d_f}) f_{sw} \quad (8)$$

- Gate charge loss [6]:

$$P_g = (q_{g_h} + q_{g_l}) v_{gs} f_{sw} \quad (9)$$

- Conduction loss in the inductor [6]:

$$P_{L_dcr} = (i_{out}^2 + \frac{\Delta i_L^2}{12}) dcr \quad (10)$$

- Loss in the input capacitor [6]:

$$P_{c_in} = i_{c_in(rms)}^2 ESR_{c_in} \quad (11)$$

Here, input capacitor rms current [6]:

$$i_{c_in(rms)} = i_{out} \frac{\sqrt{v_{out}(v_{in} - v_{out})}}{v_{in}} \quad (12)$$

- Loss in the output capacitor [6]:

$$P_{c_out} = i_{c_out(rms)}^2 ESR_{c_out} \quad (13)$$

Here, output capacitor rms current [6]:

$$i_{c_out(rms)} = \frac{\Delta i_L}{2\sqrt{3}} \quad (14)$$

- Total power loss [6]:

$$P_{loss_total} = P_{on_h} + P_{on_l} + P_{sw_h} + P_{sw_l} + P_{diode} + P_{cos.s} + P_{dead} + P_g + P_{L_dcr} + P_{c_in} + P_{c_out} \quad (15)$$

- Converter output power [6]:

$$P_{out} = P_{in} - P_{loss_total} \quad (16)$$

- Efficiency [6]:

$$\eta = \frac{P_{out}}{P_{in}} \quad (17)$$

The detailed descriptions and values of the parameters used in (1)-(17) are given in

Table 5.3.

Table 5.3. Specifications of synchronous buck converter.

Parameters	Variable	Value	Unit
Rated power	P_{rated}	400	W
Inductor	L	24 [8]	μ H
Input capacitor	C_{in}	470 [9]	F
Output capacitor	C_{out}	100 [9]	F
Switching frequency	f_{sw}	40	kHz
High-side MOSFET on-resistance	R_{on_h}	24 [7]	m Ω
Low-side MOSFET on-resistance	R_{on_l}	24 [7]	m Ω
High-side MOSFET rise time	t_{r_h}	38 [7]	ns
High-side MOSFET fall time	t_{f_h}	16 [7]	ns
Low-side MOSFET rise time	t_{r_l}	38 [7]	ns
Low-side MOSFET fall time	t_{f_l}	16 [7]	ns
Forward direction voltage of low-side MOSFET body diode	v_D	2.5 [7]	V
Peak value of body diode reverse recovery current	i_{rr}	30 [7]	A
Body diode reverse recovery time	t_{rr}	17 [7]	ns
Low-side MOSFET drain-source & gate-drain capacitance	C_{oss_l}	294 [7]	pF
High-side MOSFET drain-source & gate-drain capacitance	C_{oss_h}	294 [7]	pF
Dead time for rising	t_{d_r}	58 [7]	ns
Dead time for falling	t_{d_f}	26 [7]	ns
Gate charge of high-side MOSFET	q_{g_h}	157 [7]	nC
Gate charge of low-side MOSFET	q_{g_l}	157 [7]	nC
Gate drive voltage	v_{gs}	5 [7]	V
Inductor DC resistance	dcr	2.5 [8]	m Ω
Equivalent series resistance of input capacitor	ESR_{c_in}	15 [9]	m Ω
Equivalent series resistance of output capacitor	ESR_{c_out}	27 [9]	Ω

5.4. Simulation and Results

The solar energy generation from SEV rooftop and hood-top PV panels based on the PSC pattern as shown in Fig. 5.8 is simulated taking into account the effect of the efficiency of the modeled buck converter from section 5.3.2. The simulation runs based on genetic algorithm (GA), a metaheuristic inspired by the biologically inspired operators such as mutation, crossover and selection. The resultant is the optimum cell dimension, number of series and parallel cells, and number of modules indicating how many cells are contained by each module.

Running two separate GA optimization for roof and hood assuming they both have their own buck converter, the outcome of the simulation for roof from MATLAB workspace is shown in Fig. 5.9.

Name ^	Value
cell_dimension_init	1
cell_dimension_lb	1
cell_dimension_ub	20
exitflag	0
fval	335.4930
Generations_Data	6
InitialPopulation_Data	1
lb	1
no_of_parallel_strings	89
nvars	1
output	1x1 struct
PopInitRange_Data	[1;20]
population	[2;2.2500;2;1.6...
PopulationSize_Data	6
rr	5
score	[335.4930;356....
ub	20
x	2

Fig. 5.9. Outcome of GA for Roof.

In Fig. 5.9 for roof, $x=2$ means optimum cell dimension is 2 cm, $rr=5$ means each module will contain 5 cells in series and there will be 26 modules in series, and 89 indicates the number of parallel strings. Fig. 5.10 explains the optimized array structure for the roof.

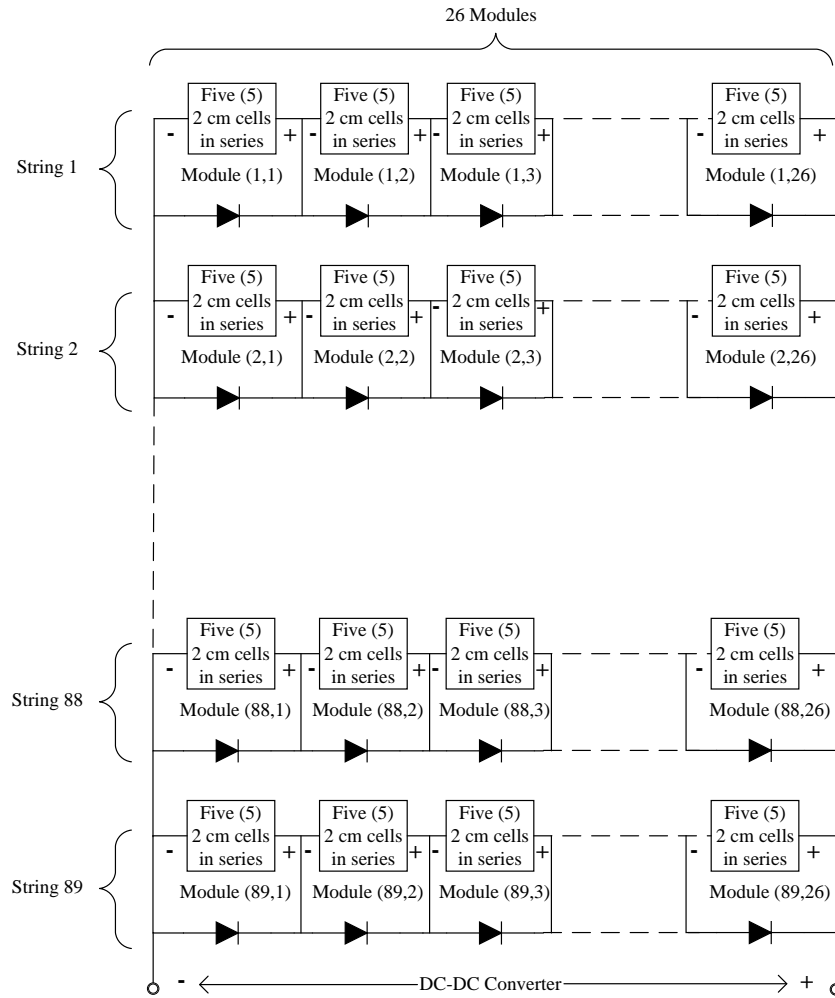
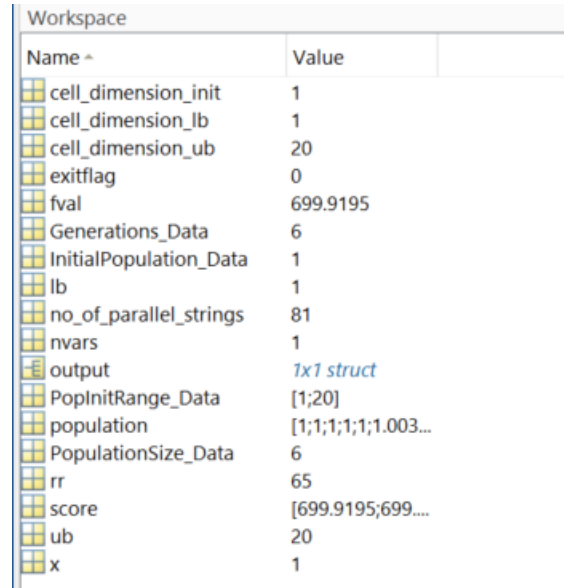


Fig. 5.10. Optimized array for Roof.

Similarly, Fig. 5.11 shows for the hood that the optimum cell dimension is 1 cm, each module will contain 65 cells in series, and there will be 2 modules in series and 81 parallel strings. Fig. 5.12 explains the optimized array structure for the hood.



Name	Value
cell_dimension_init	1
cell_dimension_lb	1
cell_dimension_ub	20
exitflag	0
fval	699.9195
Generations_Data	6
InitialPopulation_Data	1
lb	1
no_of_parallel_strings	81
nvars	1
output	1x1 struct
PopInitRange_Data	[1;20]
population	[1;1;1;1;1;1.003...
PopulationSize_Data	6
rr	65
score	[699.9195;699....
ub	20
x	1

Fig. 5.11. Outcome of GA for Hood.

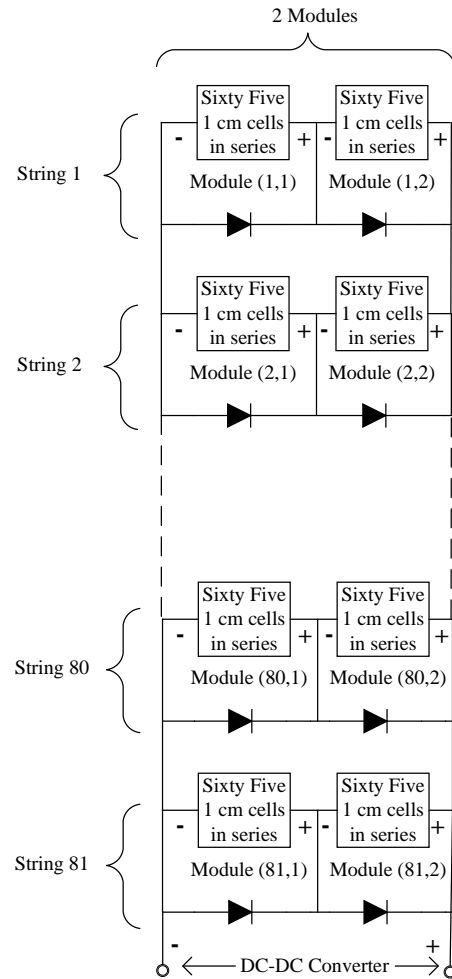


Fig. 5.12. Optimized array for Hood.

Assuming the SEV had a trip everyday throughout the year, Table 5.4, 5.5, and 5.6 show the monthly and annual accumulated energy comparison for the optimized cell and array configuration and an unoptimized array configuration, i.e., 4cm cell dimension and 4 cells in a module.

Table 5.4. Energy comparison for optimized and unoptimized array for roof.

Month	Accumulated PV Energy (kWh)		Savings (%)
	Optimized Array	Chosen Unoptimized Array	
January	33.50	32.60	2.68
February	38.23	37.20	2.71
March	54.93	53.46	2.68
April	69.51	67.94	2.26
May	77.23	75.58	2.13
June	74.97	73.43	2.06
July	77.05	75.50	2.02
August	71.77	70.29	2.06
September	54.83	53.41	2.59
October	45.94	44.73	2.64
November	35.57	34.62	2.67
December	30.97	30.14	2.67
Annual	664.51	648.89	2.35

Table 5.5. Energy comparison for optimized and unoptimized array for hood.

Month	Accumulated PV Energy (kWh)		Savings (%)
	Optimized Array	Chosen Unoptimized Array	
January	14.91	13.89	6.82
February	17.11	15.90	7.02
March	24.70	22.96	7.03
April	31.62	30.54	3.40
May	35.17	34.32	2.43
June	34.17	33.37	2.36
July	35.06	34.26	2.28
August	32.56	31.71	2.60
September	24.61	22.94	6.79
October	20.55	19.15	6.82
November	15.86	14.77	6.87
December	13.76	12.83	6.79
Annual	300.08	286.65	4.48

Table 5.6. Total energy comparison for optimized and unoptimized array.

Month	Accumulated PV Energy (kWh)		Savings (%)
	Optimized Array	Chosen Unoptimized Array	
January	48.40	46.49	3.95
February	55.34	53.10	4.04
March	79.63	76.42	4.03
April	101.13	98.48	2.62
May	112.40	109.90	2.22
June	109.15	106.80	2.15
July	112.11	109.76	2.10
August	104.33	102.00	2.23
September	79.44	76.35	3.89
October	66.49	63.88	3.93
November	51.43	49.39	3.96
December	44.73	42.97	3.94
Annual	964.59	935.54	3.01

5.5. Conclusion

This chapter has performed a system level analysis indicating that the Option 1 power electronic architecture with 12 V bus is a promising one to use in SEVs for maximum solar energy extraction. Based on this decision, the analysis is further carried out to find the optimum PV cell dimension, number of such cells in series parallel interconnection, and possible module size taking the power electronic converter efficiency modeling into account. GA has been used to optimize the array structure which shows an annual 3% energy savings compared to an assumed random unoptimized array structure. As the occurrence and profile of PSC can greatly vary, more real-life partial shading data is needed to improve the optimization of the array structure for better energy savings. Moreover, this research has simplified the roof and hood structure by eliminating the slight curves around the sides. Future research may focus on the curved surface for improved optimization results.

Chapter 5 references

- [1] M. H. Mobarak, R. N. Kleiman, and J. Bauman, "Solar-Charged Electric Vehicles: A Comprehensive Analysis of Grid, Driver, and Environmental Benefits," in *IEEE Transactions on Transportation Electrification*, vol. 7, no. 2, pp. 579-603, June 2021.
- [2] C. Schuss, T. Fabritius, B. Eichberger and T. Rahkonen, "Impacts on the Output Power of Photovoltaics on Top of Electric and Hybrid Electric Vehicles," in *IEEE Transactions on Instrumentation and Measurement*, vol. 69, no. 5, pp. 2449-2458, May 2020.
- [3] *Preliminary Specification Sheet CIGS Thin Film Solar Modules*, Available Online: <https://xsunx.com/pdf/CIGSBrochure-draft.pdf>
- [4] F. Xue, R. Yu and A. Q. Huang, "A 98.3% Efficient GaN Isolated Bidirectional DC–DC Converter for DC Microgrid Energy Storage System

- Applications," in *IEEE Transactions on Industrial Electronics*, vol. 64, no. 11, pp. 9094-9103, Nov. 2017.
- [5] N. Shafiei, M. Ordonez, M. A. Saket Tokaldani and S. A. Arefifar, "PV Battery Charger Using an L3C Resonant Converter for Electric Vehicle Applications," in *IEEE Transactions on Transportation Electrification*, vol. 4, no. 1, pp. 108-121, March 2018.
- [6] *Application Note: Efficiency of Buck Converter*, Available Online: https://fscdn.rohm.com/en/products/databook/applinote/ic/power/switching_regulator/buck_converter_efficiency_app-e.pdf
- [7] *Silicon carbide Power MOSFET HiP247-4 package*, Available Online: <https://www.mouser.ca/datasheet/2/389/dm00753355-2042264.pdf>
- [8] *Filter Inductors, High Current, Radial Leaded*, Available Online: <https://www.mouser.ca/datasheet/2/427/ihv-1762807.pdf>
- [9] *Conductive Polymer Aluminum Solid Electrolytic Capacitors*, Available Online: https://www.mouser.ca/datasheet/2/293/201904_PCH_e-1842995.pdf

Chapter 6: Conclusions and Future Work

6.1. Conclusions

As long-range EVs are becoming more affordable due to reducing price, it is most important now to evaluate and minimize the effects of their increasing charging demand on distribution transformers. While centralized and distributed smart-charging techniques have been the focus of the research trend, they require a lot of infrastructure and will take huge investments and time to deploy. This research initially proposes the Vehicle-Directed Smart Charging concept, Random-In-Window (RIW), with two variants: fixed rate charging (RIW-FR) and variable rate charging (RIW-VR) strategies to be implemented by a suitably programmed EV without requiring additional infrastructure. RIW results in a similar transformer aging rate as a centralized smart-charging algorithm over a summer week for EV penetration rates up to 60% for long-range EVs and up to 70% for short-range EVs for various transformer sizes. This study has extensively been supported by logged driving dataset of 150 unique drivers over one week.

Going further to try to help the problem more by reducing the net energy the vehicle needs to charge from the grid, a concept of a large-scale solar-charged electric vehicle (SEV) with low-cost flexible thin film PV cells integrated directly onto the steel of all upwards-facing body panels of the vehicle i.e., roof, hood, and trunk is proposed. This research has shown that the proposed low-cost SEV concept offers real benefits to the grid, the driver, and the environment, indicating that further research is warranted to address the design and manufacturing challenges

of SEVs. For the given dataset of 150 drivers, the use of SEVs (compared to non-solar EVs) would reduce the annual net vehicle energy consumption and eventual CO₂ emission by 18-22% under average cloud conditions and including temperature-dependent PV efficiency. The peak solar range extension is up to 47 km/day on a sunny day in May and charging costs are reduced by about 20% for average cloud conditions. Combining all the results together, the study has shown real potential of SEVs in mitigating transformer aging, benefitting drivers, and promoting cleaner environment. Thus, the design and manufacturing challenges associated with SEVs deserve real attention.

To ensure maximum solar power extraction in SEVs, Chapter 4 proposes a totally new approach to finding the global maximum power point (GMPP) during uniform radiation change and PSC using a single current sensor. The proposed parabolic assumption (PA) GMPPT algorithm can directly and immediately calculate the GMPP, in contrast to the other contemporary algorithms including optimization-based search methods that have significantly longer convergence times by using a fixed number of current scans (steps) equal to the number of series connected solar modules in the array. The PA GMPPT algorithm uses simple parabolic equations to calculate the GMPP near-exactly during PSC. Negligible tracking energy loss, computationally inexpensive algorithm eligible to be implemented on a simple microcontroller, lower cost due to a single current sensor, 10 to 33 times faster convergence, and excellent experimental tracking efficiency,

i.e., minimum of 99.6% make the proposed PA GMPPT algorithm outperform other contemporary GMPPT algorithms.

It is also important to have optimum cell size and optimum number of series and parallel connected cells in the array to ensure maximum solar power extraction, while also considering the effect on efficiency of the power electronic converters in the SEV electrical architecture. Thus, the research proposes a novel method using GA to optimize the PV array while also considering the power electronics design. The proposed estimation of the possible interconnection of the cells shows a solar energy savings of up to 3% during PSCs compared to the assumed random unoptimized array. Overall, this thesis has proposed useful strategies for mitigating distribution transformer aging in the face of rising EV penetration rates. Furthermore, some practical challenges related to the proposed large-scale SEV concept are addressed.

6.2. Recommendation for Future Work

The recommendations for future work focus on both improving the existing studies and further developing the on-board solar charging concept on both large scale and small-scale basis. The first recommendation is to formulate the aging process of solid-state transformers (SSTs) and analyze the effect of EV charging stress on them based on the formulated equivalent aging factor. SSTs can accommodate DC and/or AC interfaces with high frequency isolation between medium voltage grid and renewables. Thus, they are becoming popular for distributed energy storage, EVs, and DC or AC loads and gradually replacing the

currently used conventional transformers. As SSTs are different from conventional power or distribution transformers in terms of construction and operation, it would be necessary to study the effectiveness of the proposed RIW and SEV concept in the mitigation of the aging of the SSTs.

The second recommendation is to make SEVs decentralized solar generation systems by incorporating a bidirectional on-board charger in the vehicle. Though some prior works have focused on the design and control of bidirectional on-board chargers for EVs for V2G functionality, no work to date has considered its use in SEVs. With a smart energy management system, a V2G enabled SEV with a bidirectional on-board charger can fully charge overnight from the grid and feed any extra solar energy back to the grid during the day reducing electricity costs. Therefore, future research on the cost and complexity reduction of bidirectional on-board chargers would be crucial for SEVs.

The next recommendation would be studying the benefits of on-board solar charging on low traction power vehicles, e.g., golf carts, three-wheeler rickshaw, city commuters, etc. The solar energy obtained from such vehicles' on-board solar energy generation system will have to be compared to their daily energy requirements based on their respective drive cycles to realize the feasibility of installing on-board solar charging options on these vehicles.

The last suggestion for future work is in the area of optimization of PV cell size and interconnection and power electronic architecture. The current study has

optimized the cell size and interconnections by modeling partial shading and assuming upward facing body panel to be flat. The modeled PSC data often could be different from actual PSCs on a fast-moving car. The upward facing body panel of the car is also slightly curved at some places. Moreover, the power electronic MPPT converter efficiency has been modeled based on switches with fixed rating. The voltage stress on switches would be different in reality based on different PV voltages with different PV cell sizes. Therefore, extensive real-life partial shading data from a fast-moving car, inclusion of surface curvature of the SEV, and inclusion of the objective of minimizing voltage stress on the MPPT converter switches would be useful for a better optimized on-board solar array. The optimization process has considered an architecture with 12 V bus system typically present in most of the EVs. Vehicles with different bus voltages, e.g., 24 V system in commercial and military vehicles, 36 V in tow tractors and Golf carts, etc., also have the prospect of reducing their charging requirement from the grid by incorporating on-vehicle solar charging. Hence, the PV cell and interconnection optimization can be carried out for these vehicles based on their power electronic architecture with different bus voltages to maximize the on-board solar energy extraction for them.